Ion Cyclotron Emission on ASDEX Upgrade

Rodolphe D'Inca

München 2014

Ion Cyclotron Emission On ASDEX Upgrade

Rodolphe D'INCA

Dissertation
an der Fakultät für Physik
der Ludwig-Maximilians-Universität
München

vorgelegt von
Rodolphe D'Inca
aus Nizza

München, den 12. Dezember 2014

Erstgutachter:	Prof. Dr. Hartmut Zohm
Zweitgutachter:	Prof. Dr. Gregor Morfill
Tag der mündlichen Prüfung:	13.12.2014

Zusammenfassung

Diese Arbeit bespricht die Ion Cyclotron Emission (ICE), eine Plasma-Instabilität welche sowohl in astrophysischen Plasmen als auch in Fusionsmaschinen wie Tokamaks und Stellaratoren vorkommen ist, sofern hier eine Verteilung hoch-energetischer Ionen anzufinden ist. Diese Ionen können mit den Plasma Wellen, welche wiederum vom Plasma unterstützt werden, interagieren und so neue Formen von Instabilitäten mit Frequenzen im Mega-Hertz Bereich hervorrufen. Letzter können anhang von Radio-Frequenz Proben erfasst werden. In der Hoffnung mehr über die schnellen Ionen zu erfahren, wurde in den Jahren 1992-2002 intensiv zu diesem Thema geforscht. Tatsächlich wurden in dieser Zeit viele theoretisch und experimentelle Fortschritte erzielt; jedoch blieb das Ziel ein Diagnostik für schnelle Ionen zu erstellen unerreicht.

Diese Tatsache beruhte im wesentlich auf zwei Gründen. Zunächst beinhaltet das Erstellen eines solchen Diagnostiks die Inbetrachtnahme einer Vielzahl von Plasma Phänomenen: Wellen-Ausbreitung, Resonanzen, Konversion und Absorption, Rand- und Core-Plasma Modellierung, schnelle Ionen Erzeugung und Verlauf. Diese unterschiedlichen Aspekte sind zudem eng miteinander verwoben und man brauchte genau Daten im zeitlichem und frequenziellem Bereich, sowie eine Theorie welche zwischen diesen Phänomenen ein so geartete Verbindung schafft, dass die Bedeutsamkeit eines jeden der genannten Parameter erschließbar wird. Der zweite Grund ist von praktischer Natur und betrifft die technischen Schwierigkeiten auf welche man trifft, wenn man ein Hochfrequenz-Signal vor einer nicht zu unterschätzenden Hintergrundgeräusch herauszufiltern sucht.

Das Ziel der vorliegenden Studie ist es nun diese Probleme unter Zuhilfenahme der im Bereich der Erfassungstechnik erzielten Fortschritte und einer verbesserten ICE Theorie, welche die Beziehungen zwischen den Eigenschaften der schnellen Ionen und denen der beobachteten Emissionen speziell hervorhebt, neu aufzurollen.

Abstract

This works deals with the Ion Cyclotron Emission (ICE), a plasma instability that takes place both in astrophysical plasmas and in fusion energy facilities like Tokamaks and Stellarators, when a population of high energetic ions is present. These fast ions can interact with the waves that propagate in the background thermal plasma and excite instabilities in the Mega-Hertz range. This emission is measured in a non-intrusive way with radio-frequency probes and provides information on the characteristics of the fast ions. The hope of a new diagnostic sparked many studies in the years 1992-2002 but, in spite of the theoretical and experimental progresses, no operational instrumentation was developed.

There are indeed two main difficulties: first, the ICE involves many different types of plasma phenomena: wave propagation, resonances, conversion and absorption in complex geometries, core and edge plasma modelling, fast ion creation and trajectories; all these aspects are entangled. Therefore, accurate data both in time and frequency domains and a theory that covers these physics fields are necessary to distinguish the impact of the different phenomena. Second, there are technical difficulties in measuring high-frequency signals with a sufficient Signal-to-Noise Ratio to discriminate it from the background noise.

The purpose of this study is to address these issues with the use of the latest acquisition technologies and an improved ICE theory, which can relate in a new light the properties of the fast ions to the characteristics of the emission.

Contents

Und für mich steht im Mittelpunkt meines Interesses an der Philosophie wie auch an den Naturwissenschaften ihre unverzagte Suche nach neuem Wissen über die Welt... Für mich verliert also die Philosophie und auch die Naturwissenschaft ihre Anziehungskraft, wenn sie diese Suche aufgeben - wenn sie Fächer für Spezialitäten und für Spezialisten werden und die Rätsel unserer Welt nicht mehr sehen und nicht mehr über sie staunen können.

-K. Popper, die Anfänge des Rationalismus

Introduction

This thesis is the fruit of several years of work on the topic of Ion Cyclotron Emission (ICE), a plasma instability that can be found in astrophysical plasmas and in fusion energy facilities like tokamaks and stellarators, when a population of very energetic particles, also called fast ions, is present. These ions can resonate with the plasma waves supported by the plasma, and excite some new modes of instabilities with frequencies in the Mega-Hertz range that can be detected with radio-frequency probes. ICE in tokamaks was intensively studied in the years 1992-2002 with the hope to extract information on the fast ions from the measured signal. A lot of theoretical and experimental advances were achieved at that time but the objective of designing a diagnostic remained out of reach for two reasons. First, this phenomenon covers a broad range of plasma phenomena: wave propagation, resonances, conversions and absorption, edge and core plasma modeling, fast ions production and trajectories. These different aspects are deeply intertwined and it requires accurate data in time and frequency domains, and a theory that makes the connection between these different phenomena to unravel the role of each parameter. The second reason is the technical difficulty to acquire low amplitude radio-frequency signal in a noisy background with a sufficiently high signal-to-noise ratio and a proper time resolution. The purpose of our study is to address these issues by using the progress made in acquisition techniques and by improving the ICE theory to explicitly highlight the relation between the properties of the fast ions and the characteristics of the observed emission.

Figure 1: The ASDEX Upgrade tokamak. In orange, the transmission lines of the ICRF system.

We have tried to build a coherent system to explain the instability, working both on the improvement of the acquisition of experimental data and on the development of the theoretical tools. As for the practical aspects the target-machine for the measurements is ASDEX Upgrade (AUG), a divertor tokamak located in Garching, Germany, which features a complete set of diagnostics to study the plasma edge. ICE has never been observed on it before and we have developed a dedicated setup to acquire its signal and carry out the measurements, covering about 2 years of experimental campaigns, with various plasma configurations and operational parameters. They complete the existing data obtained on other machines with somewhat different characteristics. On the theoretical level, our objective is not only to bring clarity in the various existing theories of ICE

by highlighting their similarities and differences, but also to reveal the link between the global parameters of the fast ions (energy, orbit invariants) and the local properties of the instability (growth rate, mode structure). In this sense, the Hamiltonian framework and its application to the particle/wave interaction are, for us, the key to the use of the emission as a diagnostic.

The report is divided into five parts: first, we put the role of ICE in the context of the vast area of fusion research. Following a top-down path, we briefly present the energetic and environmental issues and how fusion energy can be a solution. Then we go more in the details of a specific facility, the tokamak, describing its principles of operation and its architecture. It will be the occasion to introduce the basic concepts of plasma physics that will be useful for our study. After that, we will turn on to a short phenomenology of instabilities and, more particularly, of ICE as previously observed on the machines. The purpose there is not to do a review but to highlight its key features which we will use as a reference for our own measurements. To finish this part, we will show why a diagnostic for fast ions is important not only for present facilities but also for burning plasma experiments like the test reactor ITER which is currently developed to validate fusion plasma confinement as a viable source of energy. The second section is dedicated to the theory of ICE. We will first present the general Hamiltonian tools and the way to apply them to the interaction of particles with waves in the ion cyclotron range of frequencies. We will obtain a general relation between the constants of motion of the fast ions, their distribution in energy and the wave structure. From there, we will see how to calculate the growth rate of the instability (it represents the short term evolution of the emission) and how to evaluate the coupled "quasi-linear" evolutions of the population of fast ions and of the wave (this represents the long-term evolution). To finish we will apply this general framework to the different types of ICE by modeling the distribution functions of the ions and the wave modes. In the third section, we present the hardware: first, the tokamak ASDEX Upgrade (AUG) with its main geometrical and operational characteristics as well as an introduction to the heating systems and diagnostics of interest for our study. Second, the setup that we have designed and realized to acquire the signal of ICE, covering the probes, the signal conditioning chain, the digitizers, drivers and post-processing tools. The results of the measurements are presented in the fourth section, sorted in function of the nature of the ICE observed. We will present the characteristics acquired in frequency domain, their time evolution, the condition of existence of the emission and its relation with other instabilities. The fifth part leads to the synthesis of the experimental and theoretical results under the form of a discussion. It has three objectives: to verify that the emission observed fits with the theory of ICE developed in section two; to explain some specific features of the emission, left unexplained by previous theories; and to show how the data can be used to reconstruct the parameters of the popu-

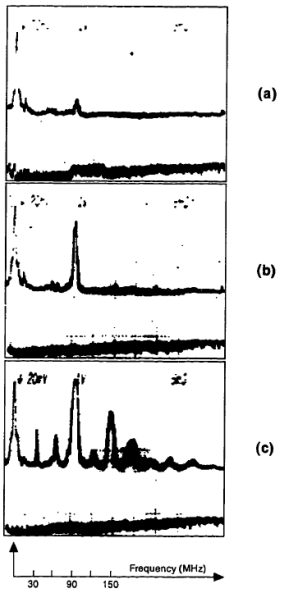

Figure 2: The first measurements of ICE on TFR in 1979. The cases a, b and c correspond to different conditions of neutral beam injections.

lation of the fast ions that excite the instability. This study does not manage to solve all issues of ICE, it even open new ones. There are a lot of possible (and required) improvements of the theory and of the diagnostics; we detail them in the conclusion. However, we think that it offers a clear and coherent framework to tackle this instability and use it to investigate fast ions.

On a more personal touch, this study was a challenging and exciting adventure: it was my first step in fusion research, drove me to many dead ends, brought me to contemplate the wonderful theoretical edifices elaborated by the geniuses of plasma physics and to get a share from the vast practical knowledge of our RF engineers and technicians. I hope that the results presented here will be able to rekindle the flame of interest for ICE as an area of research and will lead fusion scientists to include it in the growing set of diagnostics for fast particles on fusion research facilities.

Figure 3: The wave Picture taken during the conference on RF heating in Newport, May 2011. Also called *the Destiny of the reckless ICRF physicist*

To finish, I would like to thank Pr. Noterdaeme who made this thesis possible and Pr. Zohm who organized the international doctorate network which gave us detailed insights in the engineering of a tokamak and gave me precious comments on the report. The whole ICRF team, and more particularly Franz Braun, was present to support my work and bring precious help in the abstruse domain of RF technics. For the physics of fast ions, I had many fruitful discussions with Manuel Garcia-Munoz and Fernando Meo for the possible use of the Collective Thomson Scattering as a diagnostic to investigate ICE. I also had a strong support from M. Lohs which showed me the details of the interface between the Time Digital Controller and the ASDEX Upgrade Time network, and of course from M. Giannone which gave me the access to the RF probes located in the vacuum vessel. For the TRANSP simulations, I could have done nothing without G. Tardini. B. Geiger was also kind to give me his last update of the code GOURDON. I would also like to thank the other students of the International PhD Network, with whom I shared good moments in Padova and Lisbon. I thank Stephane Assas who helped me to clear the ground at the beginning of the thesis. And last but not least, my dear wife Yuna who supported my work in the (many) downs and (not so many) ups of the endeavor and my children who added a bit of spice to it.

Rodolphe D'Inca, December 2014

1 *From energy issues to fast ions: an overview of nuclear fusion*

This chapter will set up the framework for our study on ion cyclotron emission. Although we focus on a very specialized and tiny area of the nuclear fusion physics, we need to keep in mind the big picture and what the role of emission is in the bigger issue of nuclear fusion as a source of energy. Indeed, our field of research is dedicated to finding a solution to the energy crisis. But first we have to understand what the reasons for this energy and environmental problem and why we need to develop alternative sources of energy.

Figure 1.1: Natural Lighting. *Credits wb skinner - Flickr CC.*

The second step is to show why nuclear fusion can be one of those suitable new sources of energy and how we can develop facilities to deploy it. There are different ways to produce fusion reactions, but not all are equal in terms of development and hope they generate in the scientific community. Tokamaks are among the most promising facilities and ITER (International Tokamak Experiment Reactor), the billion dollar project being built by an international cooperation of institutes and companies throughout the world, should confirm and demonstrate that technologies are ready to promote fusion as a competitive and efficient energy source. We will describe the architecture and principle of operations and define the concepts of plasma physics necessary for our study. This will lead us to the description of instabilities in plasma and, more particularly, of the ion cyclotron emission. Its main features and its relation with fast ions, as observed on other machines, will be described and will serve as reference for the next sections. To finish, we will highlight the role of the fast ions in the plasma burning facilities and why it is important to diagnose them. This chapter is mostly a summary of fusion research and plasma physics with an emphasis on the elements which are relevant for our study; it is based on plasma physics books like [9] and [2].

1.1 *Environmental problems and the energy crisis*

There are two drivers in our perception of the energy situation: first, the problem of a climate change and the environmental impact of the present sources of energies. Second, the increase in the energy demand cannot be sustained by the existing sources of energies (cf. Figure 1.2).

At the same time, the United Nations climate change conferences

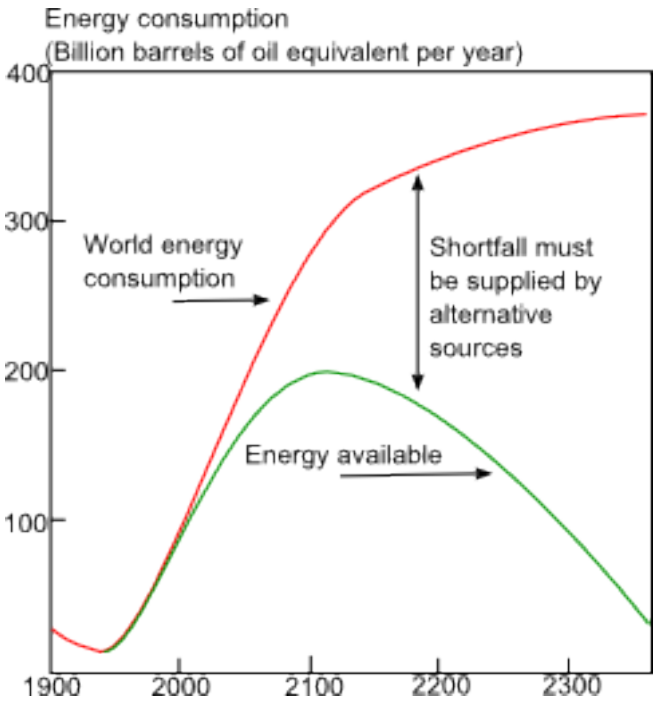

Figure 1.2: Comparison between long term evolutions of energy demand and resources based on data from the World Energy Council. It assumes that the world population stabilizes at 10 billion consuming at 2/3 of the US 1985 rate. *Source: Culham Center for Fusion Energy*

acknowledge climate change as one the greatest challenge of the present days and that actions should be taken to limit the temperature increase below 2 degrees. Consequently, alternative sources of energy have to be developed and to be socially accepted. One of these sources could be the nuclear fusion, which in spite of its tremendous technical and theoretical difficulties, can be promising in terms of efficiency and respect of the environment.

1.2 *Nuclear fusion as an answer*

A coherent model of the fusion reactions of light elements was established in 1936-1939 by Atkinson, Bethe and Houdemans.

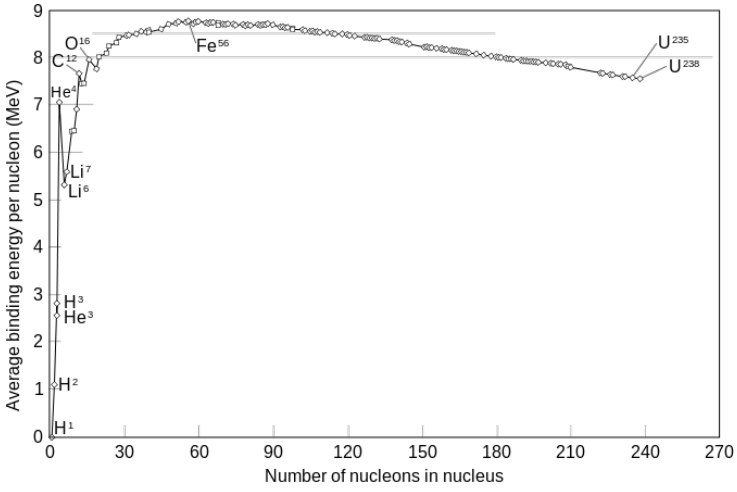

Figure 1.3: Binding energy per nucleus as calculated from a semi-empirical formula by Bethe and Weizsäcker taking into account the balance between nuclear and Coulomb forces

Considering, an atom nucleus made of A nucleons, Z protons and

A-Z neutrons, the mass M(A,Z) of the nucleus verifies:

$$M(A,Z) < Zm_p + (A-Z)m_n$$

m_p is the mass of the proton and m_n is the mass of the neutron

This insures the stability of the nucleus. Consequently, the formation of a nucleus by A nuclei releases an energy B(A,Z). The binding-energy per nucleus $B(A)/A$ can be represented by the Dempster curve shown on Figure 1.3.

The reaction energy is the difference Q between the binding energies of products and reactants. If $Q > 0$ we have an exo-energetic reaction, which is achievable with the fusion of light elements.

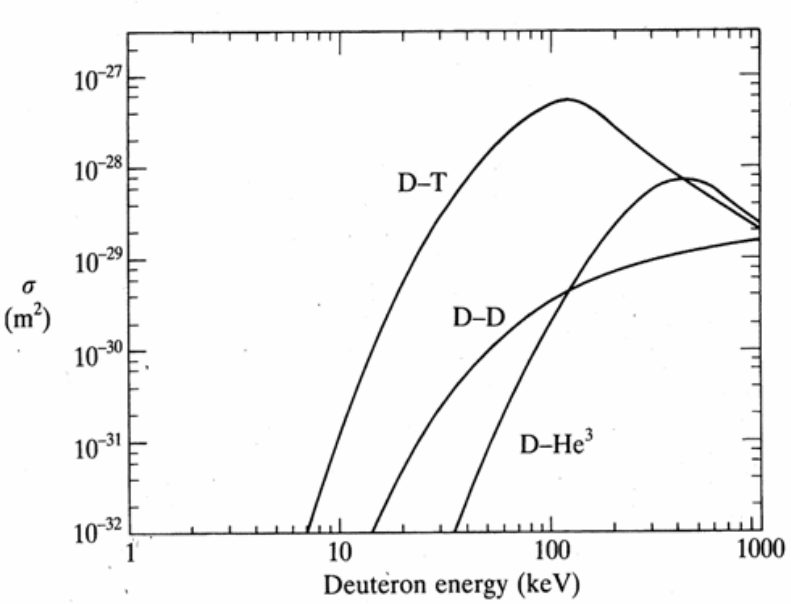

Figure 1.4: Cross-section σ of the most exo-energetic fusion reactions of Hydrogen isotopes.

The most promising reaction is the following one:

$$D + T \rightarrow He^4\ (3.5\ MeV) + n\ (14.1\ MeV) \tag{1.1}$$

where D is Deuterium, T is tritium, He Helium and n for neutron. The He^4 isotope is called the α particle.

The reactions are induced by collisions; therefore it is necessary to take into account the notion of cross-section. For a monoenergetic beam of ions reacting on a static target, as represented on Figure 1.5, the cross section is defined by:

$$\frac{dN}{dxdydz} = -dn_1 = n_1 n_2 \sigma(v_1) v_1 dt$$

It is represented on Figure 1.4 for different Hydrogen isotopes reacting on deuterium in function of its energy. The tritium has clearly the highest cross-section for temperatures If we consider a more realistic case, where the ions populations have a distribution of energy $f(\mathbf{v})$, the cross section is defined statistically by:

$$< \sigma v >_{DT} = \int |\mathbf{v_D} - \mathbf{v_T}| \cdot \sigma_{DT}(|\mathbf{v_D} - \mathbf{v_T}|) f_D(\mathbf{v_D}) f_T(\mathbf{v_T}) \mathbf{dv_D dv_T}$$

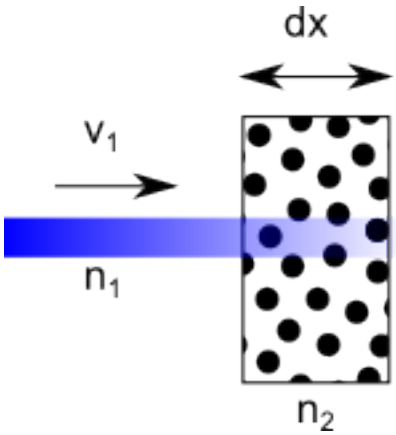

Figure 1.5: Reaction between a beam of nuclei X_1 at velocity V_1 with a static target X_2.

In the case where the reactants have a Maxwellian distribution function, i.e. in thermodynamical equilibrium, we get $< \sigma v >_{DT}$ in function of their temperature.

The reaction between Deuterium and Tritium has the highest cross-section and releases the highest energy; this is why it is the main candidate for use in a future power plant. The advantage of fusion over other classical sources of energy emerges when we compare the energy density Q/m (where Q is the energy released by the reaction and m the total mass of reactants): about $3.10^{14}\ J.kg^{-1}$ for D-T fusion and about $10^{7}\ J.kg^{-1}$ for a chemical combustion. The Deuterium-Tritium reaction has been used only on few tokamaks (JET, TFTR) because of the difficult handling of tritium and because of the highly energetic neutrons fluxes that activate all components in the neighborhood and require remote handling for the maintenance. Consequently, most fusion research facilities like ASDEX Upgrade prefer to use less efficient reactions (with a cross section 10 to 100 times lower than the D-T one) but which are still sufficient to investigate most of the relevant phenomena be. The most used reactions are Deuterium-Deuterium:

$$D + D \rightarrow He^3\ (0.82\ MeV) + n\ (2.5\ MeV) \tag{1.2}$$

$$D + D \rightarrow T\ (1.0\ MeV) + p\ (3.0\ MeV) \tag{1.3}$$

where D is Deuterium, T is tritium, He Helium, n for neutron and p for the proton. The He^4 isotope is called the α particle. We note that the two D-D reactions are equiprobable.

The purpose of a fusion facility is to reach the temperature where the cross-section is the highest, corresponding to higher reactions rates.

1.2.1 *Power balance*

The release of energy by the fusion reactions is only a part of the power balance: losses have to be included as well and, possibly, external heating to compensate these losses.

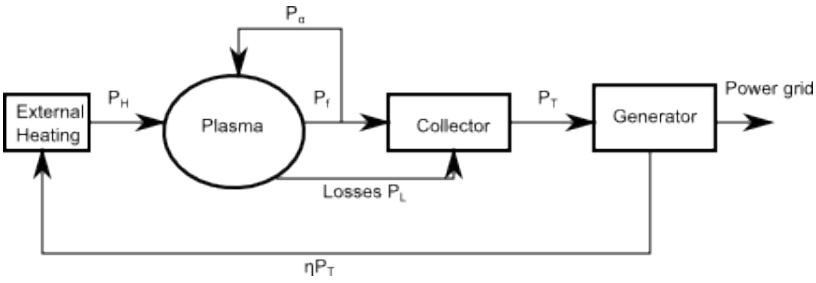

Figure 1.6: Schematic representation of the power balance in a fusion facility.

A schematic view of the power balance for a fusion power plant is represented on Figure 1.6. Two modes of operations can be considered depending on whether the losses are compensated by external heating (the plasma works as power amplifier) or by a part of the fusion energy (ignition). These two modes can be combined to have an intermediate mode of energy production.

Lawson criterion We consider the first mode of operation where losses are completely compensated by external heating and we look

for a criterion to make this solution possible. The fusion reaction power in a D-T plasma (with densities $n_D = n_T = n/2$) is given by:

$$P_f = Q\frac{n^2}{4} < \sigma v > \tag{1.4}$$

where α is a coefficient of proportionality, k_B is the Blotzmann constant, τ_E is the energy confinement time and Q the energy released.

The losses are the sum of two terms:

$$P_L = \alpha n^2 T^{1/2} + \frac{3nk_BT}{\tau_E} \tag{1.5}$$

The first term represents the radiation due to bremsstrahlung and the second term covers all other losses and is characterized by the energy confinement time τ_E. The total power in output is $P_T = P_f + P_L$, which is converted with an efficiency η to provide the auxiliary power heating $P_H = \eta P_T$. This power is used to compensate the losses: $P_H > P_L$. By substituting Equations 1.4 and 1.5, we get the Lawson criterion:

$$n\tau_E > \frac{3k_BT}{\frac{\eta}{1-\eta}\frac{1}{4} < \sigma v > Q - \alpha T^{1/2}} \tag{1.6}$$

This gives a condition on the density and the energy confinement time to be able to compensate the losses by external heating.

Ignition

Now, if we can use a part of the Fusion power P_T to compensate the losses (for instance, by containing the alpha particles in the case of D-T reacions), it is possible to decrease or even, in the best case of ignition, to suppress the amount of necessary external heating power. The power released in the form of alpha particles is given by:

$$P_\alpha = \frac{1}{4}n^2 < \sigma v > \zeta_\alpha \tag{1.7}$$

where $\zeta_\alpha = 3.5$ MeV is the energy of an alpha particle.

We consider now an energy confinement time τ_E^* that covers all losses (including bremsstrahlung):

$$P_L = \frac{3nk_BT}{\tau_E^*} \tag{1.8}$$

For ignition, we need to have $P_\alpha > P_L$, which gives the following criterion:

$$n\tau_E^* > \frac{12}{\zeta_\alpha}\frac{T}{< \sigma v >} \tag{1.9}$$

The criterion is represented on Figure 1.7.

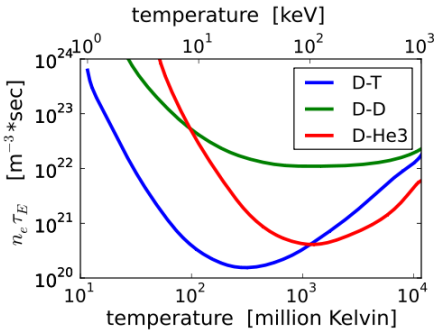

Figure 1.7: n-τ function of temperature for different reactions. The minimum represents the optimal temperature point to achieve the Lawson criterion.

The advantage of fusion, in addition to its high efficiency, is the release of low radioactive products and that there is no risk of criticality. Deuterium can easily be found in water. The limiting point is the Tritium that doesn't exist in the nature and has to be produced by using Lithium in a tritigeneous blanket at the periphery of the reactor.

1.3 *Magnetically confined Fusion: the Tokamak*

The concept of tokamak was invented in the 50s by the Soviet physicists Igor Tamm and Andrei Sakharov, inspired by an original idea

of Oleg Lavrentiev. A magnetic field is used to confine a plasma and reach the density and temperature required to satisfy the Lawson criterion. The acronym tokamak comes from the Russian тороидал'ная камера с магнитными катушкам which means *toroidal chamber with magnetic coils*.

1.3.1 Plasma physics

The main component of the tokamak is the confined plasma, a ionized gas made of electrons and ions. As shown on Figure 1.8, this fourth state of the matter covers a wide range of parameters. In our case, the plasma has a density in the range of 10^{19} m^{-3} for a temperature of several keV. It is completely ionized and magnetized.

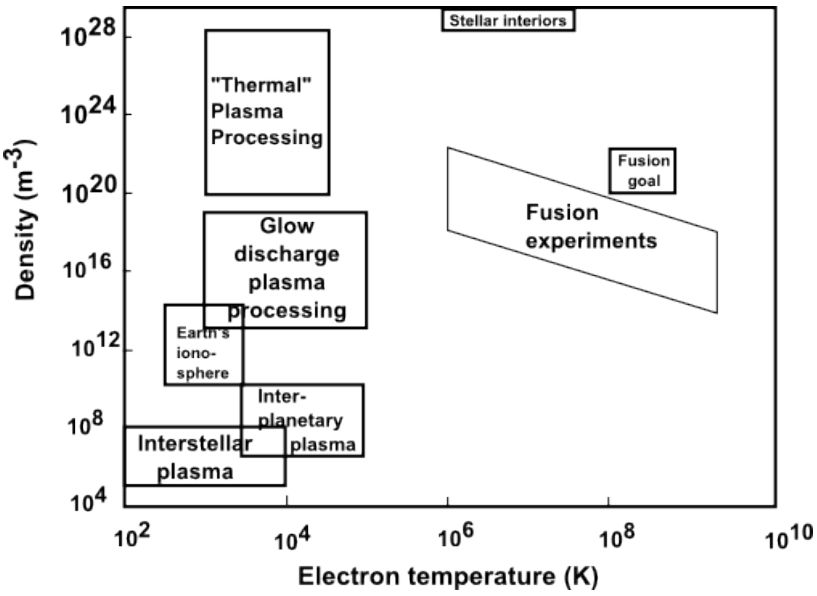

Figure 1.8: Classification of plasmas in function of their density and of their electronic temperature.

The behavior of the plasma comes from the strong coupling between its electromagnetic field and the movement of its particles. The electromagnetic field is governed by the Maxwell equations, written here in SI units:

$$\nabla \cdot \mathbf{E} = \frac{\rho}{\epsilon_0} \qquad \text{Maxwell-Gauss} \qquad (1.10)$$

$$\nabla \cdot \mathbf{B} = 0 \qquad \text{Maxwell-Gauss} \qquad (1.11)$$

$$\nabla \times \mathbf{E} = -\frac{\partial \mathbf{B}}{\partial t} \qquad \text{Maxwell-Faraday} \qquad (1.12)$$

$$\nabla \times \mathbf{B} = \mu_0 \mathbf{j} + \mu_0 \epsilon_0 \frac{\partial \mathbf{E}}{\partial t} \qquad \text{Maxwell-Ampere} \qquad (1.13)$$

where $\mathbf{E}$ *and* $\mathbf{B}$ *are respectively the electric and magnetic field;* ρ *is the charge density,* ϵ_0 *and* μ_0 *respectively are the electric and magnetic constant;* $\mathbf{j}$ *is the current.*

The movement of the particles is mainly affected by the electromagnetic field through the Lorentz force:

$$\mathbf{F} = q[\mathbf{E} + (\mathbf{v} \times \mathbf{B})] \qquad (1.14)$$

and, to a less extent (because of the quasi-neutrality), by the Coulomb force that we will neglect for the moment.

Several authors still use the CGS units, which are also useful for numerical simulations because of a reduced order of magnitude of the different values. For our numerical calculations on Alfvén Eigenmodes in Section 2.2.1, we used these units as well to be able to compare with the previous works and to simplify the numerical work. Therefore we recall here the Maxell equations in CGS units and we will indicate it in the text when we use these units:

$$\nabla \cdot \mathbf{E} = 4\pi\rho; \nabla \cdot \mathbf{B} = 0$$

$$\nabla \times \mathbf{E} = -\frac{1}{c}\frac{\partial \mathbf{B}}{\partial t}$$

$$\nabla \times \mathbf{B} = \frac{4\pi}{c}\mathbf{j} + \frac{1}{c}\frac{\partial \mathbf{E}}{\partial t}$$

where $\mathbf{v}$ *is the velocity of the particle of charge* q.

This looks like a very simple description of a confined plasma but it is considerably complicated by the number of particles, the geometry and the configuration of the electromagnetic field. This complexity can be handled by ordering the time and space scales between the different mechanisms at stake in the plasma.

The smallest scale for time and space corresponds to the condition for plasma quasi-neutrality: if we create a separation of charges in the plasma, it will relax back to the neutrality in a time $1/\omega_p$ where ω_p is called the *plasma or Langmuir frequency* and is defined, for each type of particle, by:

$$\omega_p \equiv \sqrt{\frac{nq^2}{\epsilon_0 m}} \tag{1.15}$$

where n is the density of the type of particles considered.

The associated length corresponds to the minimal distance above which the plasma can be considered neutral (the local electric field is then shielded by the the other particles) and it is the *Debye length*:

$$\lambda_D \equiv \frac{v_{Te}\sqrt{2}}{\omega pe} \tag{1.16}$$

With this basic definition, we can start to consider the basic adiabatic movements of the particles, both ions and electrons, in a confined plasma.

1.3.2 *Adiabatic invariants and drifts*

The simplest case to deal with is an homogeneous magnetic field constant in time.

In this case, the Lorentz force given by Equation 1.14 reduces to its magnetic part and the Newton's law of motion can be written:

$$m\frac{d\mathbf{v}}{dt} = q\mathbf{v} \times \mathbf{B} \tag{1.17}$$

where m is the mass of the particle.

The motion in this case is a simple helix along the magnetic field line, as represented on Figure 1.9. The frequency of rotation around the line is the *gyro-frequency*:

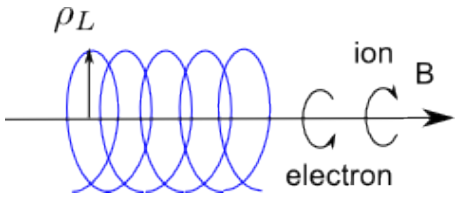

Figure 1.9: gyromotion of particles for an homogeneous static magnetic field.

$$\omega_c \equiv \frac{|q|B}{m} \tag{1.18}$$

We can note that ions and electrons rotate in opposite directions. The associate radius is called the *Larmor radius* ans is given by:

$$\rho_L \equiv \frac{mv_\perp}{|q|B} \tag{1.19}$$

where $v_\perp$ is the projection of the velocity perpendicular to the field line.

The complexity of the magnetic configuration is overcome when we separate the slow variation of the background field and the fast gyration. The orbit of the particle can then be decomposed into a slow part, which is the movement of the gyrocenter as defined on Figure 1.10, and a fast part which is the gyration itself. The choice of adiabatic conditions makes it possible to find invariants of motion, which will be useful in the later sections.

First we consider the invariance due to the adiabatic character of a magnetic field that respects one or both of the following conditions:

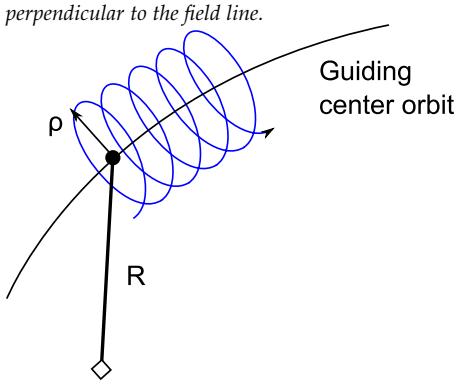

Figure 1.10: Decomposition of the trajectory in guiding center orbit characterized by the position R and Larmor gyration given by the radius ρ.

- slow time evolution: $\partial B/\partial t \ll |\omega_c|B$,
- small spatial variation of B: $\rho_L \partial B/\partial \mathbf{r} \ll B$.

In this case, a perturbative treatment of the law of motion 1.17 with a field featuring these particularities shows that the result of the inhomogeneities is the *diamagnetic force* applied to the gyrocenter:

$$\mathbf{F} \equiv -\mu \cdot \nabla B \tag{1.20}$$

where μ is the magnetic moment and is an invariant of movement:

$$\mu \equiv \frac{m v_\perp^2}{2B} \tag{1.21}$$

The existence of this force shows that, with a gradient of magnetic field , it is possible to trap the particles in a bottle-like configuration shown on Figure 1.11. The problem is that energetic particles can still overcome the bottle neck and escape the trap, resulting in a loss of confinement. The idea is to close the bottle in a torus-like shape. Yet, a torus with just a radial gradient of the magnetic field is not sufficient to insure the good confinement. The existence of this gradient and of the curvature of the field drives a drift of the particles, which is given by:

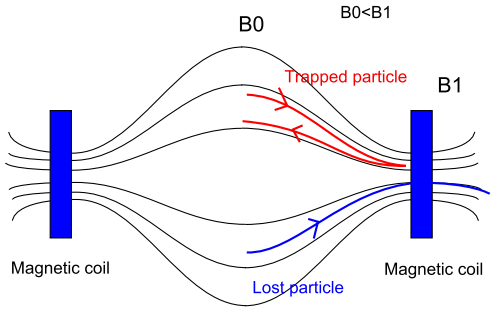

Figure 1.11: Principle of the magnetic mirror. The increasing gradient towards the necks brake the particle which, if it is not too energetic, will bounce back.

$$\mathbf{V_{Dg}} = \frac{v_c^2}{\omega_c^2}\mathbf{b} \times \frac{\nabla B}{2B} \qquad \text{Gradient drift}$$

$$\mathbf{V_{Dc}} = \frac{v_\parallel^2}{\omega_c}\mathbf{b} \times \frac{\mathbf{n}}{R} \qquad \text{Curvature drift}$$

where v_c is the velocity of the gyration, $v_\parallel$ is the velocity parallel to the magnetic field, $\mathbf{b}$ is the unit vector parallel to the magnetic field line, $\mathbf{n}$ is the unit vector perpendicular to the field line and R is the radius of curvature of the field.

In the case of the tokamak, the toroidal field $\mathbf{B}$ can be considered in first approximation irrotational ($\nabla \times \mathbf{B} = \mathbf{0}$) and the total drift velocity is given by:

$$\mathbf{V_D} \equiv \mathbf{V_{Dg}} + \mathbf{V_{Dc}} = \frac{1}{R\omega_c}(v_\parallel^2 + \frac{v_c^2}{2})\mathbf{b} \times \mathbf{n} \tag{1.22}$$

The drift velocities of ions and electrons have opposite directions and create a separation of charges and to an electric field into the plasma. The superposition of these drifts leads in turn to another drift velocity, the *$E \times B$ drift*:

$$\mathbf{V_E} = \mathbf{E} \times \frac{\mathbf{B}}{B^2} \tag{1.23}$$

We summarize all these drift movements in the Figure 1.12. We note that the electric drift has the same sign for electrons and ions.

The effect of the electric drift, as summarized on Figure 1.13 is an outward movement of the particles and the confinement is lost in a time too short to respect the Lawson criterion.

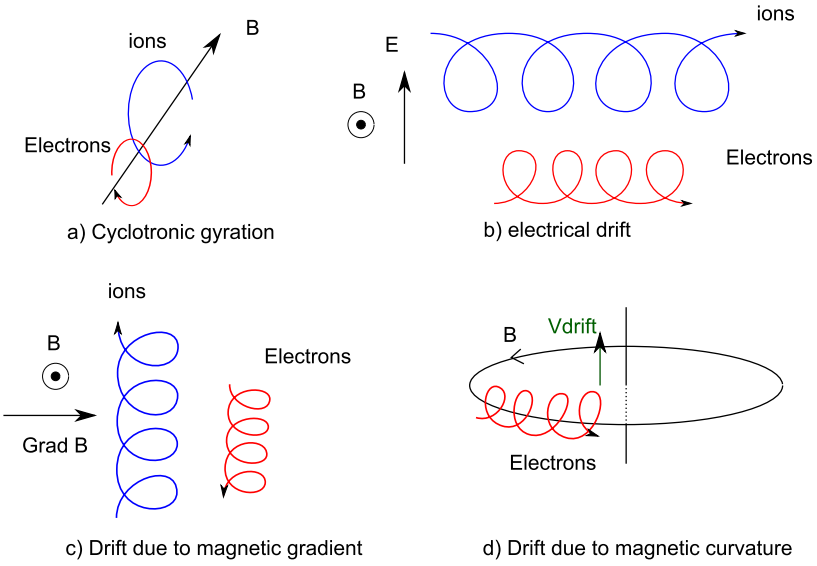

Figure 1.12: Drift of ions in different magnetic field configurations.

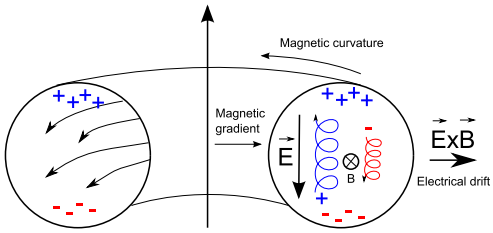

Figure 1.13: Effect of the drift velocities on the confinement in a toroidal configuration.

The solution is to add a component to short-circuit this separation of charges: the poloidal field. As a result, each magnetic line looks like a helix revolving around the torus major axis. An example is plotted on Figure 1.14. We describe the configuration and principle of operations in the next section.

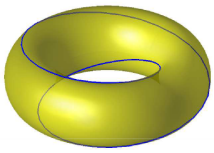

Figure 1.14: Representation of a magnetic line with the safety factor q=2.

1.3.3 *Tokamak configuration*

The magnetic structure is presented on Figure 1.15. In the simplest possible model (which will be useful for the next section), the magnetic field is given by the toroidal and poloidal components:

$$B_\phi(R) = B_c \frac{R_c}{R} \approx B_c(1 - \frac{r}{R_c} cos\theta) \qquad \text{Toroidal} \qquad (1.24)$$

$$B_\theta(R,r) = \frac{r}{q(r)R} B_\phi(R) \qquad \text{Poloidal} \qquad (1.25)$$

We have introduced here the *safety factor* defined by:

$$q(r) \equiv \frac{r}{R} \frac{B_\phi}{B_\theta} \qquad (1.26)$$

It represents the ratio of the number of turns followed by a field line around the magnetic axis over the number of turns around the toroidal axis. Two further characteristics of interest for ASDEX Upgrade are the triangularity $\delta = b/a$ (and its inverse, the elongation k) and the inverse aspect ratio $\epsilon = a/R_c$ which is small ($\epsilon \to 0$) for machines like AUG with a large aspect ratio.

where B_ϕ is the toroidal field, B_θ is the poloidal field, R is the coordinate on the major axis, r is the coordinate on the minor axis, B_c is the field at the center of the plasma and R_c is the major axis. Cf. Figure 1.15.

1.3.4 *Orbit of particles*

With these elements defined, we can now have a better look at the trajectories of the particles in the tokamak configuration. We use a "ballistic" approach based on the solution of the Newton equation of

motion for ions and electrons with a low energy. In the next section, we will use the Hamiltonian approach, which can deal with highly energetic particles. Using the magnetic drift 1.22 and the description of the field given in the previous subsection, we can write the equations of motion of the guiding center in the directions parallel and perpendicular to the field:

$$\frac{dr}{dt} = v_D sin\theta \qquad \text{Perpendicular:}$$
$$\frac{d\theta}{dt} = \frac{v_\parallel}{qR_c} + v_D \frac{cos\theta}{r}$$
$$\frac{dv_\parallel}{dt} = -\frac{\mu B_c}{mqR_c} r sin\theta \qquad \text{Parallel}$$

The particles fall into two groups:

- the circulating particles which have a high parallel velocity ($v_\parallel \gg v_c$) and will turn around the magnetic axis.
- the trapped particles dominated by a high gyration velocity ($v_c \gg v_\parallel$) which bounce back and forth between two maxima of the magnetic field along their trajectory.)

The corresponding trajectories are represented on the Figure 1.16 for the case where magnetic fields and currents have the same direction.

The maximum excursion of these orbit from the local magnetic surface is given by $2\delta_b \propto \epsilon^{-1/2} q\rho_L$ [1], which means that the low-energy particles "stick" to the magnetic surfaces. But for high energies, ρ_L becomes high, and we have orbits with a large extension in comparison with the minor radius[2]. These fast ions will be of particular interest for ICE and will be further studied in part 2.2.2.

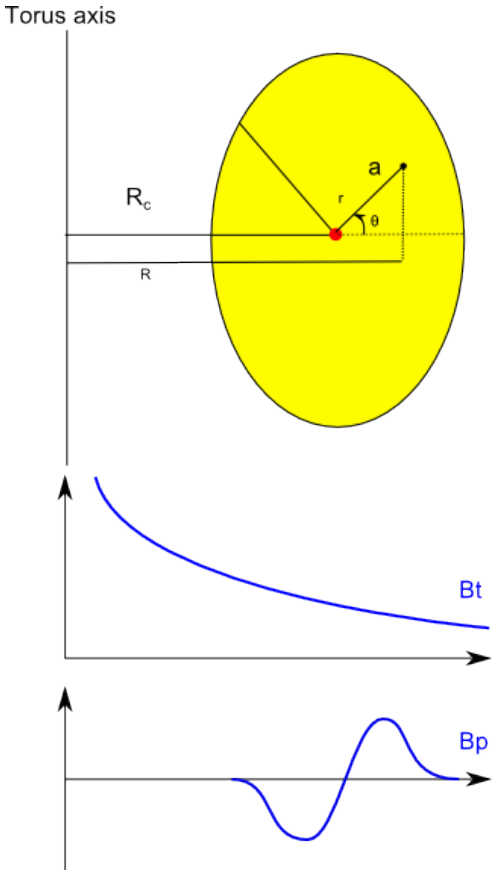

Figure 1.15: Half section of a tokamak with main geometrical characteristics and correspond magnetic field profiles.

[1] where $\epsilon = r/R$ is the local aspect ratio of the toroidal magnetic surface, q is the safety factor and ρ_L is the Larmor radius

[2] $\epsilon \leq (2q_0\rho/R)^{2/3}$ where q_0 is the safety factor is the center fails for these orbits

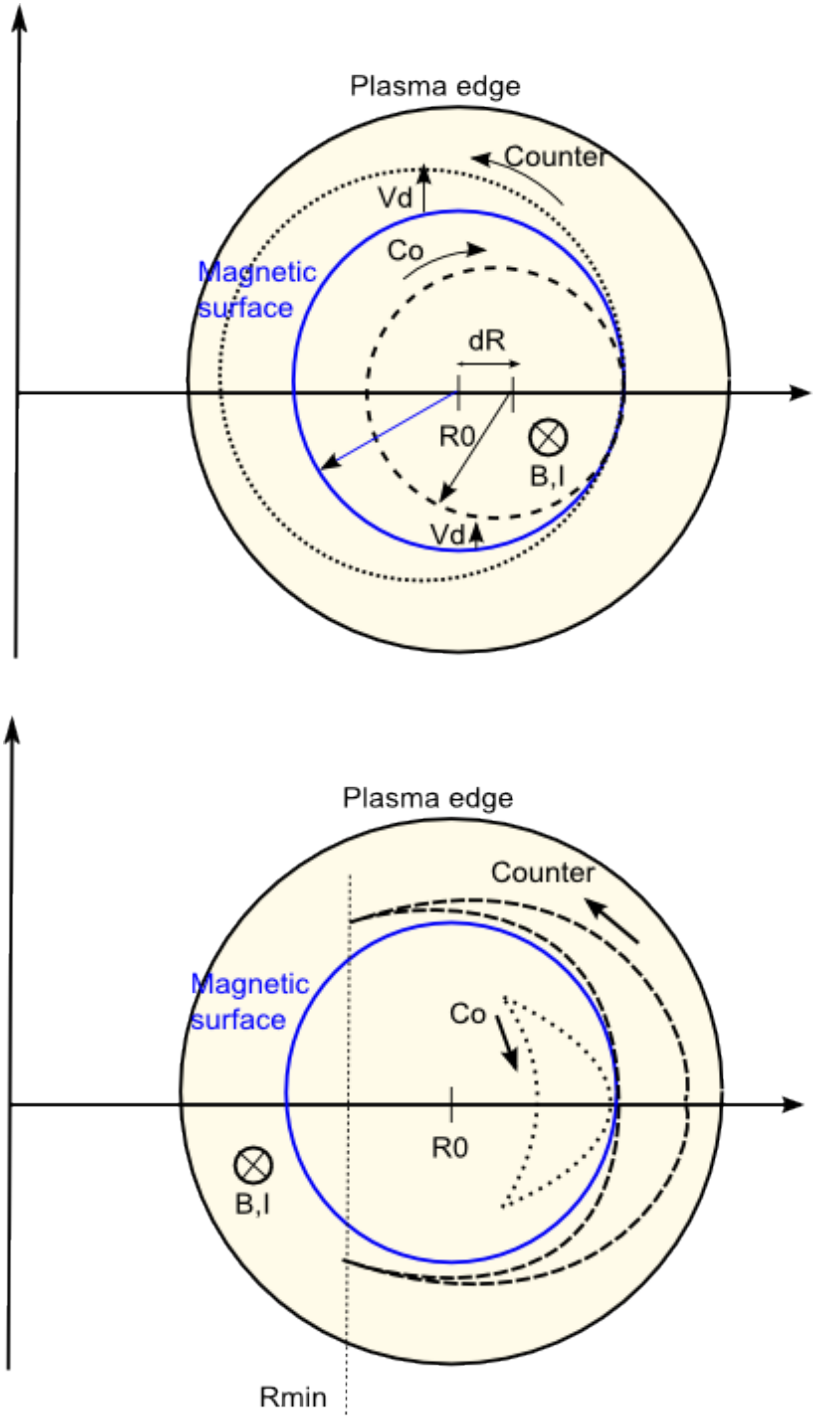

Figure 1.16: Representation of particle orbits in a section view of the magnetic configuration of a tokamak. At the top: circulating particles in co- or counter-current direction. V_d is the drift velocity. At the bottom, the "banana" shape of the trapped particles in co- and counter-current direction.

We have shown how the particles can be confined inside the plasma of the tokamak thanks to the torus-shaped configuration of the magnetic field. The right equilibrium has to be calculated to obtain this configuration. Given a current and a pressure profile, the magnetic fluxes are solutions of the *Grad-Shafranov* equation (cf. [3]).

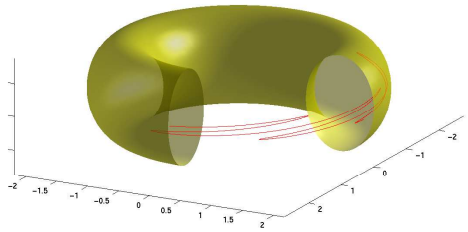

Figure 1.17: 3D representation of a banana orbit of the gyrocenter, computed with method of invariants.

1.3.5 *Architecture and Operations*

The simplified structure of a tokamak is presented on Figure 1.18. The main solenoid forms a transformer with the plasma as secondary circuit and produces a time-varying poloidal flux, which induces, inside the plasma, a loop voltage and a current due to the finite resistivity of the plasma.

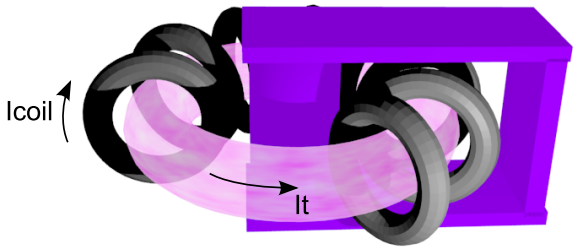

Figure 1.18: Main elements of a tokamak: toroidal coils in black, central solenoid in purple and plasma. The coils that insure the vertical stability of the plasma are not represented.

The evolution of the loop voltage, current and temperature of the plasma is presented in an example on Figure 1.19.

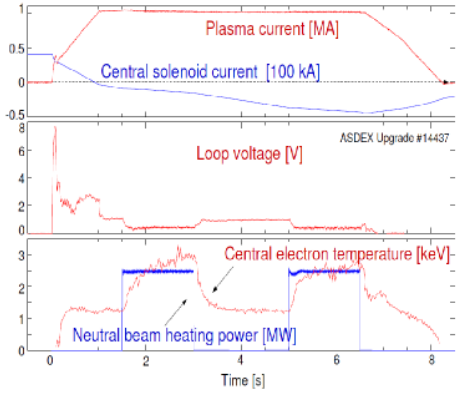

Figure 1.19: Evolution of the main plasma parameters during a classical discharge on a tokamak.

To reach the temperatures characteristic of a fusion plasma, a tokamak requires auxiliary heating systems. There are four of them: the neutral beam injection (NBI) that heats the plasma by exchange of momentum, and three radio-frequency devices operating in different range of frequencies: ion cyclotron resonant heating (ICRF $\approx 10 - 100\ MHz$), Lower-Hybrid (LH $\approx 1 - 5\ GHz$) and the electron cyclotron resonant heating (ECRH $\approx 140\ GHz$). Two of them are more interesting for our study and will be presented in the section 3.1.2.

A plasma in a tokamak with a divertor has two main modes of confinement: the L Mode (L for Low confinement) which is the normal mode of a tokamak with Ohmic heating and the H Mode (High confinement) where a strong addition of power leads to a change in the structure of the plasma edge with a higher slope of the density and temperature pedestal resulting in a better confinement. This H-Mode is of course a mode of predilection and the source of all attention since its understanding brings some keys to a better confinement and more advanced regimes (internal barriers, current pro-

file control, ...). However, it is not a perfect solution: it reveals some particular instabilities, the so-called Edge Localized Modes or ELMS. These are regular pulsations of the pedestal supporting the H-mode: at a regular pace, the edge density profile crashes down, before rebuilding itself: it has consequences for the transport of particles and of energy, for the coupling of the auxiliary heating systems and for the loss of fast ions.

Another instability is also noteworthy for our study: the sawteeth oscillations which are seen in many tokamak discharges. The central temperature oscillates in an alternation of slow rises of several hundreds of milliseconds and fast crashes of few microseconds. During the crash, the population of fast ions is quickly depleted.

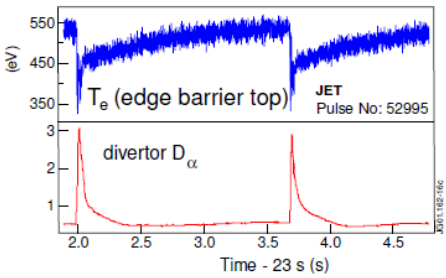

Figure 1.20: Example of observation of sawteeth trough its impact on the electron temperature at the edge and through the flux of particles in the divertor (the exhaust part of the tokamak)

1.3.6 *Instabilities*

We have mentioned in the previous section two types of instabilities. There are far more of them and they are the main source of loss of confinement when they grow beyond control. These instabilities can be triggered if there are in the plasma some reserves of "free energy", which is in excess relative to the equilibrium state with the minimum energy. They are classified in two categories, following the source of free energy: *fluid* or *kinetic*.[3]. The former includes all MHD instabilities caused by gradients of temperature, density and magnetic field. But, we are interested by the latter category. One source of free energy are the fast ions [33], which are not in thermal equilibrium because or their high velocity (ranging from hundreds of keV to several Mev). These particles are common in the plasma: the products from the nuclear reactions, the ions from the NBI beams after ionization, the ions accelerated by ICRH. They are however difficult to analyze because of their small population. As a result, few diagnostics are able to provide data on their behavior inside the plasma and on how they transfer their free energy to the plasma instabilities. It is a broad and very active area of research, both for the development of diagnostics like the Fast Ion D Alpha (FIDA) detector and for the analysis of the interactions with eigenmodes of the plasma (like the Toroidal Alfvén Eigenmodes [20]). Fast ions have different effects on the confinement: they can be lost in few microseconds, taking away their energy created by auxiliary heating systems, decreasing their efficiency. They can encounter the first wall of the tokamak, creating excessive heat loads on the surface and additional sputtering of impurities. Helium, a by-product of fusion reactions, is also created at high energy and has to be extracted from the plasma to prevent them from choking the reaction.

[3] a second classification depends on the active or dissipative nature of the instability.

1.4 *Ion Cyclotron Emission*

The Ion Cyclotron Emission is an instability that occurs in the range of several MHz, at the harmonics of the ion cyclotron frequency. It was first predicted by Harris ([31]) in 1959 and had been since then

observed on tokamaks, stellarators and space plasmas. This section will give the key features of the emission observed on other machines as a reference for our own studies. Therefore, we will not give a detailed account of the previous observations and the interested reader can refer to the thesis of Cauffman ([8]) where he will find a detailed report of the experimental results on various machines. Several types of emission can exist depending on the position inside the machine and on the source of fast ions exciting the instability.

1.4.1 *ICE due to fusion products*

The emission was first observed on TFR ([22]) where a signal corresponding to the Deuterium cyclotron frequencies at the outer midplane edge of the plasma was recorded with a magnetic probe during neutral beam injection. The absence of the signal coming from the microwave scattering diagnostic probing the center for density fluctuations confirmed the edge location of the signal. But the decisive experiments that shed light on the phenomenon were due to Cottrell's team who analyzed the emission coming from JET ([15]).

The key points of these experiments can be summarized as follows:

- during Ohmic deuterium discharges, peaks at $\omega_{ci}(D)$ at the edge are observed,
- with injection of Hydrogen neutral beams, the spectrum is conserved but the intensity of each peak increases,
- discharges with Deuterium or a mixture Deuterium/Tritium feature the same spectrum, with a higher intensity in the second case (cf. Figure 1.21),
- odd harmonics of the spectrum are less intense and the peaks are replaced by a continuum of frequencies after the 7th harmonic. The discrete part of the spectrum represents 2% of the total signal.
- a fine structure can be observed on some peaks, with a doublet spaced by $\Delta f/f \approx 0.88$,
- the signal is proportional to the fusion reactivity measured with the neutron detector (cf. Figure 1.22); it follows the time signal from the neutron rate but with a delay comparable with the slowing down time,
- there is a temporal correlation between the emission and MHD instabilities like ELMs and sawteeth.

A useful comparison was done with the experiments carried out on TFTR ([7]) with highly peaked density profiles (while on JET there are rather flat); they revealed the transient character of the emission when the fusion products are subalfvénic at the edge. Playing with the density profile, they showed that the emission could become steady and similar to JET when the density was high enough

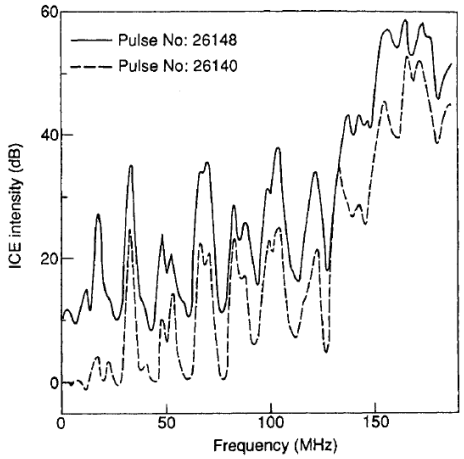

Figure 1.21: ICE spectrum for discharges in Deuterium and in Deuterium/Tritium .

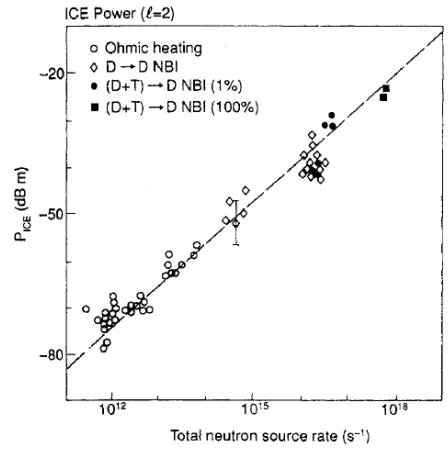

Figure 1.22: Correlation between the ICE intensity for different types of heating and the neutron rate ([15]).

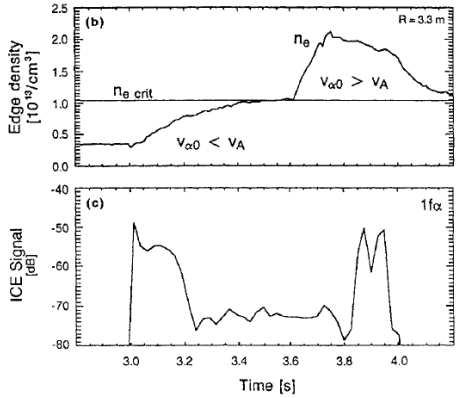

Figure 1.23: Evolution of the ICE signal in function of the superlafvenic character of the fusion products on TFTR ([7]).

at the edge for the fast particles to be superalfvénic again. In addition, they showed that another emission at the Deuterium cyclotron was steadily present during the beam injection and was located even more outside than the "FP-ICE" and featuring wider frequencies.

A series of experiments was also done on JT-60U ([50]). They were in the same situation than TFTR with transient "FP-ICE" and a steady "beam ICE". The first emission revealed the signatures of Helium-3, Tritium and protons (cf. Figure 1.24). The key point was that they were able to measure the toroidal wave number of each emission (cf. 1.25). It appeared that the FP-ICE presented a finite toroidal wavenumber, while the beam-ICE had no parallel propagation. For the Helium-3, a doublet was present and the two frequencies had opposite directions of propagation.

The first detailed theory for ICE on tokamaks was worked out by Coppi ([14]) and improved by Dendy ([17]), Gorelenkov ([30]), Fülöp ([25]) and Hellsten ([34]), to quote only the main contributors. It is still difficult to have a convergence of these theories on the details of the observed emission, but they all agree upon the common basic mechanism: a part of the fusion products created in the center of the plasma have large extension orbits and can graze the plasma edge: they create at this point a tail of fast energetic ions in the local population, a tail that acts as a source of free energy. They can release this energy by exciting the waves supported by the thermal ions in the background through cyclotron interaction (basically the same interaction used for ICRF heating).The waves excited are the fast waves propagating at the Alfvén velocity and thus requiring superalfvénic or almost superalfvénic ions to excite them. This mechanism explains the main data, but many questions are left unanswered:

- the growth rate of the instability is difficult to ascertain: it can be high and require only a local interaction, or low and need the excitation of eigenmodes (the so-called Compressional Alfvén Eigenmode or CAE); it depends on the value of the growth rate compared with the interaction time between the population of ions and the wave,
- only the growth rate in the linear approximation is calculated; the theories do not model the longer evolution of the interaction by taking into account the different damping mechanisms, the quasi-linear evolution or the non-linear coupling. In addition, it is not clear what kind of feedback the emission has on the fast ions population,
- protons can excite the half-harmonics of its cyclotron frequency: it is not clear if it is a non-linear wave-wave interaction or if the Doppler shift is high enough to excite remote frequencies,
- the ICE signal features an extreme variability, about one order of its magnitude. It is unknown if it comes from the interaction of the wave with the probe or if it is intrinsic to the emission itself,

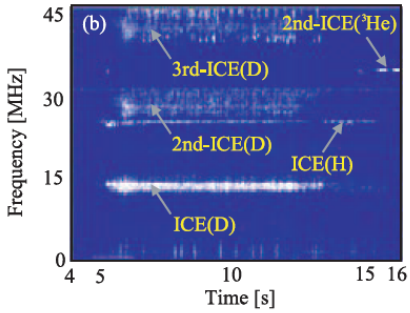

Figure 1.24: Spectrogram of frequencies in function of time for the ICE signal on JT-60U. Source: [50].

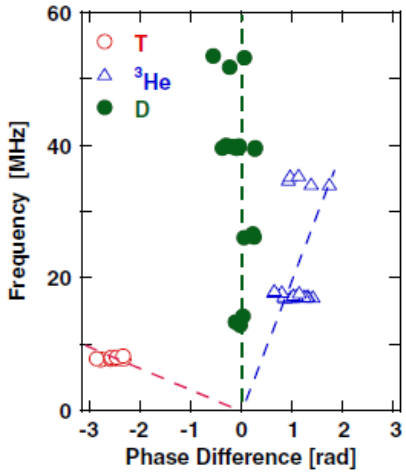

Figure 1.25: Parallel wavenumber measured by an array of probes for different emissions on JT-60U. The D emission corresponds to the beam ICE. Source: [50].

- there exist a theory for the steady "beam-ICE" proposed by Dendy ([18]), involving electrostatic waves both supported and excited by the beam ions themselves but the experimental data are still insufficient to confirm it. In addition, the intensity of the signal partly correlates with the fusion rate, which is not explained by the theory,
- to finish, there is no method to extract information on the fast ion population from the ICE signal. This is however the major interest of this instability as a diagnostic.

This short summary of the open issues will serve us as a guideline for our study and we will try in the next section to develop a formal framework that addresses these issues.

1.4.2 *ICE due to minority species during ICRF heating*

Another type of emission related to the previous one was observed by Cottrell during minority ICRF heating De(H) on JET ([16]). The spectrum is presented on Figure 1.26 where the cyclotron frequency of Hydrogen, the minority species, can be seen. The signal usually appears with a delay of 0.4s after the flat top of the ICRF power profile and shows a threshold in injected power and diamagnetic energy of the plasma. The explanation would be that, for this emission, the source of fast ions are the hydrogen ions accelerated to MeV energies by the ICRF wave: they have a similar orbit to the fusion products, with a birth place in the center, on the ICRF resonance layer and a large extension reaching the edge of the plasma where they lead to an anisotropic tail of fast ions. The interaction is then the same as for the FP-ICE. This has been the only case of m-ICE (minority ICE) observed up to now and there were few theoretical developments related to it.

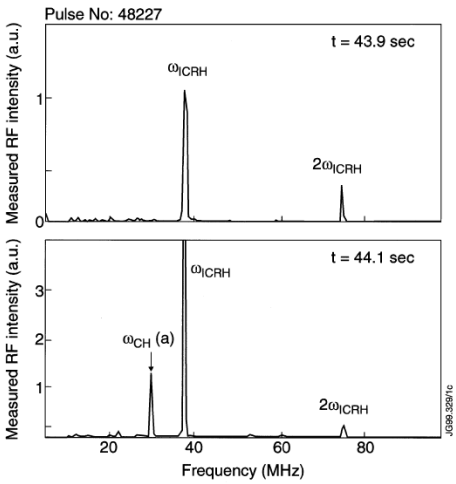

Figure 1.26: Spectrum of the ICE signal during ICRF heating on JET ([16]).

1.4.3 *ICE in the plasma center*

This is a less known type of ICE, which has been observed on few machines only. The first observations date back to the controlled experiments on JFT-2M where a train of pulses of a neutral beam was injected into the plasma. Each pulse was accompanied by a short burst of emission with a frequency corresponding to the cyclotron frequency of the beam species in the center of the plasma. When the beam ions slowed down, these bursts disappeared. More recently, the central ICE was measured on JT-60U ([42]) at harmonics of tritons in a Deuterium plasma at high plasma pressure. The signal showed some precursors before ELMs and peaked with them, but most of the time it appears at the beginning of the NBI pulse. Some theories were developed to explain the possibility of central ICE ([39]) but the lack of experimental data prevented further development.

1.4.4 Summary

In this short overview, we saw that there are four possible types of ion cyclotron emission in tokamaks:

- FP-ICE: due to the fusion products from the center and exciting the compressional Alfvén waves at the edge.
- beam-driven ICE: steady emission from the edge, probably due to the excitation of an electrostatic wave supported by the beam ions
- m-ICE: due to the minority species heated by ICRF and exciting the compressional Alfvén waves at the edge
- central ICE: emission from the center of the plasma at the beginning of beam injection. The nature is unknown

The topic of the next section is to enter into the details of the mechanism and to rigorously explain the physics at stake.

1.5 ITER and the future fusion power plants

The question of the fast ions characterization will be present on the future tokamak demonstrator being built in France in the frame of the ITER program [37]. Alpha particles, as a result of fusion, will be generated in the plasma and might excite numerous instabilities. It will be very important to diagnose them or to already have a good understanding of their behavior.

We have stressed the important role of the fast ions, both on present and future tokamaks and explained why it was necessary to have good diagnostics to get data on them. We have also presented the frame of our study: the tokamak itself, its configuration and its modes of operation. We are thus ready to enter the core of our topic, the theory of ion cyclotron emission and see how to use it as a diagnostic for fast ions.

2 *Theory of Ion Cyclotron Emission*

This section is dedicated to the theoretical framework of the ion cyclotron emission used to interpret the results from ASDEX Upgrade presented in the section 4, and extract information on the fast ions in the section 5. This is not a new theory of ICE; we use the tremendous work achieved by our predecessors to investigate ICE. However, we want a theory that can address several issues:

- the basic mechanism of ICE is known: a tail of fast ions constitutes a source of free energy that can be transfered to background plasma waves through cyclotron interaction. Several theories have been developed to detail this mechanism and find the relation between the characteristics of the exciting population of fast ions and the spectrum measured on different tokamaks. The problem is that these theories take different assumptions on the nature of the excited waves (local, global, with dominant parallel or poloidal propagation) and on the intensity of the interaction (weak or strong perturbation),
- these theories do not take into account the "long term" evolution (over several orbit periods τ_b of the exciting population) of the emission and the resulting feedback on the distribution function of the fast ions,
- the ICE at the edge, due to ICRF-accelerated ions or to fusion products, is the most common observation. But experiments also show that beam-driven ICE and, to a lesser extent, central ICE can happen as well. For the beam-driven ICE, a specific theory exists, but with a formalism of its own, which does not make easy the analysis of its relation with other type of ICE instabilities. Yet, we will see that, for AUG, they can happen simultaneously and it can be interesting to understand how the multiple interactions affect the population of ions.
- the ultimate goal of ICE, as formulated by Coppi and Dendy, is to use the emission as a non-intrusive diagnostic to extract information (velocity, pitch angle) from the exciting population of fast ions. The idea is to take the measured spectrum and, from the distribution and intensity of frequencies, to deduce the parameters of the distribution function. Up to now, this goal has not

been achieved for two reasons: first, the experimental accuracy and the plasma conditions have given rather rough spectra where few features were visible (we will deal with this problem in the case of AUG in the Section 3.2). Second, the existing theories do not clearly highlight the relation between the parameters of the distribution function and the growth rate of the different modes. In addition, the long term evolution can affect the spectrum by selecting only the most excited modes and by adding new modes by non-linear coupling.

Therefore, we want to establish a theory general enough to tackle the different types of ICE and that clearly highlights the relations between the characteristics of the fast ions and the spectrum. To do that, we will use the Hamiltonian formalism proned by Hellsten to find out the growth rate in the linear approximation and express the long term evolution in a quasi-linear frame coupled with the energy balance. We will not go as far as including non-linear coupling and saturation effects because of the tedious work which is not justified by the results which show the validity of the linear model.

Equipped with this framework, we should be able in the end to explain the measurements of the emission on ASDEX Upgrade and, in a reversed operation, from these measurements to reconstruct the distribution function of the fast ions under the form of a simple model.

This theoretical framework covers a wide range of techniques in different parts of the plasma. A fully integrated and unified theory would not have been feasible in the time of this study; consequently, we have segmented the work in several blocks: the eigenmode analysis, the fast ions modeling, the linear resonance, growth rate computation and the long term evolution. For each part, we had to make simplifying assumptions to get tractable models; we kept track of these assumptions and checked that they were coherent from one building block to the other.

2.1 *Hamiltonian theory of interactions between particles and waves*

The Hamiltonian theory of waves-particles interaction was developed by Kaufman ([41]) and applied to ICRF by Becoulet ([1]). It is regularly used to calculate the effect of ICRF heating on fast ions with code like SELFO ([40]).

In spite of its formal approach[1], it is well suited to study physical phenomena with different time scales and makes it possible to deal with both the global trajectories of the fast ions in a toroidal configuration and with the local interaction (at the edge or in the center). Thus, we approach the problem from a different direction from Dendy and Fülöp who use a local approach (even though injecting some toroidal effects of the ion orbit in [25]) or from Gorelenkov who uses the generalized gyrokinetics theory ([45]).

[1] *"The Hamiltonian approach is very elegant but rather formal and does not readily provide physical insight"* [21]

This part will be dedicated to a short, general, presentation of the theory. Readers eager of more details can be referred to the textbooks and papers related to the topic ([48], [41], [1]).

2.1.1 *Integrable motion*

For a particle of mass m and charge e in an electromagnetic field $\mathbf{E} = -\boldsymbol{\nabla}\Phi - \frac{\partial \mathbf{A}}{\partial t}$ and $\mathbf{B} = \boldsymbol{\nabla} \times \mathbf{A}$ where $\mathbf{A}(\mathbf{r}, t)$ and $\Phi(\mathbf{r}, t)$ are the vector and scalar potentials, the Hamiltonian of the particle is given by:

$$H(\mathbf{p}, \mathbf{r}, t) = \frac{[\mathbf{p} - e\mathbf{A}(\mathbf{r}, t)]^2}{2m} + e\,\Phi(\mathbf{r}, t) \tag{2.1}$$

where the canonical variables $\mathbf{p}$ and $\mathbf{r}$ can be taken in a very generalized sense, not necessarily spatial coordinates. The orbit of the particle is given by the **Hamiltonian equations**:

$$\frac{\partial \mathbf{p}}{\partial t} = -\frac{\partial H}{\partial \mathbf{r}}, \qquad \frac{\partial \mathbf{r}}{\partial t} = \frac{\partial H}{\partial \mathbf{p}} \tag{2.2}$$

Using canonical transformations, it is possible in some situations to find new variables that are solutions of the Hamilton equations and more particularly, the action $\mathbf{J}$ which is constant during the movement and the angle $\boldsymbol{\Theta}$ which follows a linear evolution:

$$\begin{aligned} \mathbf{J}(t) &= \mathbf{J_0} \\ \boldsymbol{\Theta}(t) &= \boldsymbol{\Omega}(\mathbf{J_0})t + \boldsymbol{\Theta_0} \end{aligned}$$

where $\boldsymbol{\Omega}(\mathbf{J}) = \frac{\partial H_0}{\partial \mathbf{J_0}}$ *is called the pulsation of the system.*

If such coordinates can be found, the system is said to be *integrable*. These coordinates verify the equations:

$$\frac{d\mathbf{J}}{dt} = -\frac{\partial H_0(\mathbf{J})}{\partial \boldsymbol{\Theta}} = 0 \tag{2.3}$$

$$\frac{d\boldsymbol{\Theta}}{dt} = \frac{\partial H_0(\mathbf{J})}{\partial \mathbf{J}} = \boldsymbol{\Omega}(\mathbf{J}) \tag{2.4}$$

H_0 is independent of $\boldsymbol{\Theta}$ and we can consider two orderings:

- The phase angles $\boldsymbol{\Theta} = (\Theta_1, \Theta_2, \Theta_3)$ are fast variables in comparison with $\mathbf{J}$
- inside $\boldsymbol{\Theta}$, the pulsations can have different time scales: $\dot{\Theta}_1 \ll \dot{\Theta}_2 \ll \dot{\Theta}_3$

The orbits in phase space are thus given by helices on the so-called KAM (*Kolmogorov Arnold Moser*) torus, as seen on Figure 2.1.

In a tokamak with a static $\mathbf{B}$ field, the movement of the particles is integrable and can be decomposed in three rotations/oscillations with different time scales:

- around the field lines: it is the cyclotronic gyration defined by the angle α.
- the toroidal rotation/precession[2] around the major axis defined by ϕ,
- and the poloidal rotation/oscillation around the minor axis

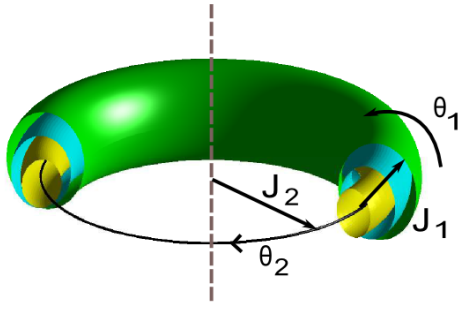

Figure 2.1: Representation of angles/actions in phase space for a Poincare integrable system with two degrees of freedom.

[2] rotation for circulating particles and precession for trapped particles).

2.1.2 *Interaction with a perturbation*

If we have now an electromagnetic wave superimposed on the static magnetic field, the Hamiltonian $H_0(\mathbf{J})$ of the integrable movement must be completed to take into account the interaction; if the field has a low amplitude, we can add a perturbed Hamiltonian $V(\mathbf{J}, \mathbf{\Theta}, t)$ with $|V| \ll |H_0|$. V is function of the angles and actions from the unperturbed Hamiltonian and can therefore be decomposed in Fourier series on $\mathbf{\Theta}$:

$$\begin{aligned} H &= H_0(\mathbf{J}) + V(\mathbf{J}, \mathbf{\Theta}, t) \\ &= H_0(\mathbf{J}) + \sum_N h_N(\mathbf{J})\ exp[j(\mathbf{N} \cdot \mathbf{\Theta} - \omega t)] \end{aligned} \tag{2.5}$$

where $\mathbf{N}$ *is a triplet of integers* (N_1, N_2, N_3).

A resonant interaction takes place when for a given $\mathbf{N}$, we have $h_N \neq 0$ and the phase of the perturbation is stationary along the unperturbed trajectory:

$$\sum_N \mathbf{N} \cdot \mathbf{\Omega}(\mathbf{J_0}) - \omega = 0$$

It is important to notice here the difference with the ballistic approach [3] where the local resonance at some point x_g of the trajectory is given by $\omega = \omega_c(x_g)$. Here, we select *entire* trajectories which are in resonance.

[3] based on the resolution of the Newton equation.

2.1.3 *Ion cyclotron interaction*

We take now the specific case of a wave in the cyclotron range of frequencies in a static field represented by the vector potential $\mathbf{A_0}$. The wave is considered in the gauge $(\mathbf{a}, \phi = 0)$ ($\mathbf{a}$ is the magnetic vector potential and ϕ the scalar electric potential) and the Hamiltonian can explicitly be written:

we have normalized the units to the mass m and the unit charge e

$$\begin{aligned} H &= \frac{(\mathbf{p} - \mathbf{A_0} - \mathbf{a})^2}{2} \\ &= H_0 - (\mathbf{p} - \mathbf{A_0})\ \mathbf{a} + \frac{\mathbf{a}^2}{2} \end{aligned} \tag{2.6}$$

The last term, quadratic in $\mathbf{a}$, is called the ponderomotive force and can be neglected for the amplitude of perturbations considered here.

The great advantage of the Hamiltonian approach is its ability to deal with complex configuration like the field of a tokamak. However, we will first consider the homogeneous, straight line case, first as an illustrative example and second because it will be also useful later for the calculation of the Landau and cyclotron damping (section 2.2.1).

Homogeneous straight field plasma

A particle (e, m) in a field $\mathbf{B} = B_0\ \mathbf{e_z}$ with a perturbation $\mathbf{a} = -ay\mathbf{e_z}$, the momentum is given by $\mathbf{p} = m\mathbf{v} + e\mathbf{a}$ and its Hamiltonian is given by the formula 2.6. The configuration is represented on Figure 2.2.

A trick[4] is used to quickly get the canonical transformation. We do

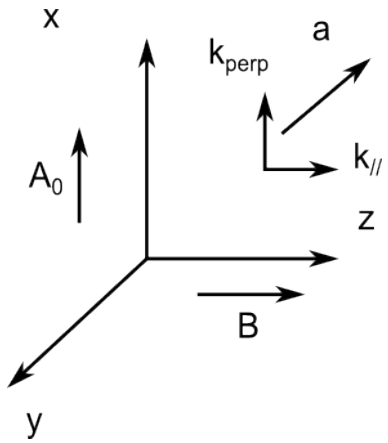

Figure 2.2: Configuration of an homogeneous straight field plasma.

[4] coming from the Hamiltonian analysis of the pendulum [48]

the following change of variable: $(x, y, z, p_x, p_y, p_z) \rightarrow (J, X, P, \theta, Y, z)$ where $x = X + \sqrt{2J}\ sin\theta$, $y = Y + \sqrt{2J}\ cos\theta$ and the unperturbed Hamiltonian can be rewritten in the new coordinates:

$$H = J + \frac{P^2}{2} \tag{2.7}$$

To get the perturbed Hamiltonian:

$$(\mathbf{p} - \mathbf{A_0})\mathbf{a} = \frac{E}{j\omega} \begin{pmatrix} \sqrt{2J}\ cos\theta \\ -\sqrt{2J}\ sin\theta \\ P \end{pmatrix} exp(j[k_\perp(X + \sqrt{2J}sin\theta) + k_\parallel z - \omega t]) \tag{2.8}$$

in a simpler form we use the Jacobi-Anger expansion $exp(jasin\alpha) = \sum_N J_n(a)exp(jN\alpha)$ where J_N is the Bessel function. The perturbed Hamiltonian is finally:

$$V = \frac{E}{j\omega} \sum_N V_N\ exp(j[k_\perp X + k_\parallel z + N\theta - \omega t]) \tag{2.9}$$

and we write V_N back in standard units for future use:

$$\mathbf{V_N}(\mathbf{v}, \mathbf{k}) = \begin{pmatrix} \frac{N\omega_c}{k_\perp}\ J_N(\frac{k_\perp v_c}{\omega_c}) \\ j\frac{v_c}{k_\perp}\ J'_N(\frac{k_\perp v_c}{\omega_c}) \\ v_\parallel\ J_N(\frac{k_\perp v_c}{\omega_c}) \end{pmatrix} \tag{2.10}$$

The argument in the Bessel function represents the ratio of the particle velocity over the wave phase velocity. The derivative of $J_N(x)$ changes its sign from positive to negative for $x = 1$. It will play an important role in section 2.1.4 when we will integrate a distribution function with this factor.

Toroidal geometry

We consider the geometry described in the section 1.3 and our purpose is to write the perturbed Hamiltonian 2.5 of a particle in interaction with a field $\mathbf{a}$ in the form:

$$V = \sum_N h_N(\mathbf{J})\ e^{j(\mathbf{N\Theta} - \omega t)} \tag{2.11}$$

We have to be cautious and distinguish the variables that belong to the configuration space and those that belong to the physical space. A representation of both spaces is given on the Figure 2.3. In the case of ICRF interaction, the perturbed Hamiltonian is written:

$$V = -Z\ e\ \mathbf{a} \cdot \mathbf{v} = -\sum_\omega \frac{jZe}{\omega} \mathbf{v} \cdot \mathbf{E}_\omega \tag{2.12}$$

where we have decomposed $\mathbf{E} = \sum_\omega \mathbf{E}_\omega e^{-j\omega t}$. This harmonic of the field depends on the position $\mathbf{q}$ of the particle and can be decomposed following the fast and slow movement of the particle:

$$\mathbf{E}_\omega = \tilde{\mathbf{E}}_\omega(\mathbf{q})exp(jS(\mathbf{q})) \tag{2.13}$$

$\tilde{\mathbf{E}}_\omega$ is the wave amplitude that varies slowly with the particle position and $S(\mathbf{q})$ is the fast oscillating phase.

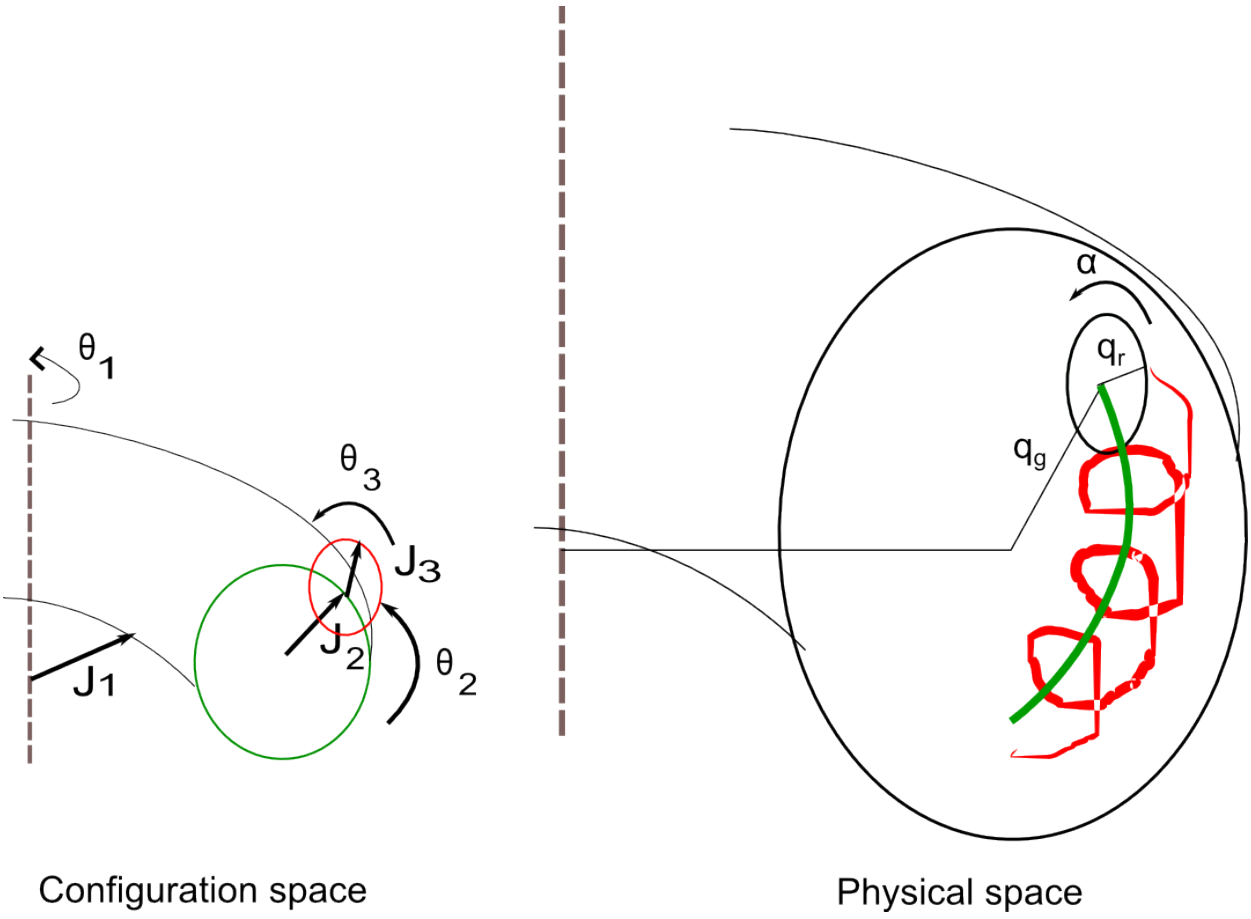

Figure 2.3: The configuration and physical spaces are intertwined in the Hamiltonian formalism: the purpose of the method is to transform the complex trajectory of the particle in physical space (made of the Larmor gyration in red and of the guiding center motion in green)in a regular smooth trajectory in configuration space.

For our case, the typical variation length is longer or comparable to the Larmor radius ρ_L. So we can expand the particle position around the guiding center: $\mathbf{q} = \mathbf{q_g} + \mathbf{q_c}$ where $\mathbf{q_g}$ is the position of the guiding center and $\mathbf{q_c}$ is the Larmor radius. The resulting field is then:

$$\mathbf{E}_\omega = \tilde{\mathbf{E}}_\omega(\mathbf{q_g}) exp(j\mathbf{k}_\perp \cdot \mathbf{q_c}) \tag{2.14}$$

where $\mathbf{k}_\perp = \boldsymbol{\nabla}_\perp S$ is the perpendicular component of the wave vector. In the reference system $(\mathbf{e_1}, \mathbf{e_2}, \mathbf{e_3})$ where $\mathbf{e_1}$ is parallel to $\mathbf{B}$, $\mathbf{e_2}$ is perpendicular to $\mathbf{B}$ and $\mathbf{e_3} = \mathbf{e_1} \times \mathbf{e_2}$, the rotation is described by:

$$\mathbf{q_c} = \rho_L(\mathbf{e_2} sin\alpha + \mathbf{e_3} cos\alpha) \tag{2.15}$$

where α is the gyroangle.

$$\dot{\mathbf{q}}_\mathbf{c} = v_\perp(\mathbf{e_2} cos\alpha - \mathbf{e_3} sin\alpha) \tag{2.16}$$

Now, we can write the perturbed Hamiltonian in the form:

$$V = -\frac{jZe}{\omega} v_\perp (E_2 cos\alpha - E_3 sin\alpha) exp(jk_\perp \rho_L sin\alpha) \tag{2.17}$$

with $E_2 = \tilde{\mathbf{E}}_\omega \cdot \mathbf{e_2}$ and $E_3 = \tilde{\mathbf{E}}_\omega \cdot \mathbf{e_3}$.

It remains to take into account the gyration and to write the electrical field in its rotating reference system: $E_\pm = (E_2 \pm jE_3)/2$ and, as in the straight line case, we expand the perturbed Hamiltonian in Bessel functions.

$$V = \sum_{l=-\infty}^{\infty} h_l(\Theta_2, \mathbf{J}, \omega) e^{jl\alpha} \tag{2.18}$$

where

$$h_l(\Theta_2, \mathbf{J}, \omega) = -\frac{jZe}{\omega} v_\perp [E_+ J_{l-1}(k_\perp \rho_L) + E_- J_{l+1}(k_\perp \rho_L)] \tag{2.19}$$

We can now perform the Fourier transform with respect to the angles $\boldsymbol{\Theta}$ and the coefficients h_N are then given by:

$$\begin{aligned} h_N(\mathbf{J}, \mathbf{N}, \omega) &= \int V e^{j\mathbf{N}\cdot\Theta} \frac{d^3\boldsymbol{\Theta}}{(2\pi)^3} \\ &= \sum_{l=-\infty}^{\infty} \int h_l(\Theta_2, \mathbf{J}, \omega) e^{j(l\alpha - \mathbf{N}\cdot\Theta)} \frac{d^3\boldsymbol{\Theta}}{(2\pi)^3} \end{aligned} \tag{2.20}$$

The gyro-angle α evolves at the local cyclotron frequency: $\dot{\alpha} = \omega_c(\mathbf{q_g}) = \Omega_1 + \tilde{\omega_c}(\mathbf{J}, \Theta_2)$ where $\Omega_1 =< \dot{\omega_c} >$. Therefore $(\alpha - \Theta_1)$ depends only on the position of the particle on its orbit and the integral in Equation 2.20 is zero unless $l = N_1$. In this case, the summation over l is trivial and it remains:

$$h_{l=N1}(\mathbf{J}, \mathbf{N}, \omega) = \frac{1}{\tau_b} \int_0^{\tau_b} h_l e^{j(l\alpha - \omega)} \frac{d^3\boldsymbol{\Theta}}{(2\pi)^3} \tag{2.21}$$

where τ_b is the drift period, i.e., the time to accomplish one poloidal turn.

where we have taken into account the **global** resonance condition 2.1.2 $\omega = \mathbf{N} \cdot \boldsymbol{\Theta}$.

Because of its strongly oscillating nature, the integral is non-vanishing when the phase in the exponential is stationary, i.e., when we have the **local** resonance condition at the point x_g^*: $l\omega_c(x_g^*) = \omega$. To be

precise, the method of the steepest descent can be applied if the variation scale of h_l is larger than the variation scale of the phase, which is given by:

$$\lambda_c = \frac{v_g}{\sqrt{p\mathbf{v_g}\cdot\boldsymbol{\nabla}\omega_c}} \tag{2.22}$$

where $\mathbf{v_g}$ is the velocity of the guiding center

if $\lambda_c < \boldsymbol{\nabla} h_l$, the formula for V can be used without further modification. Otherwise, a WKB[5] decomposition of h_l is necessary: $h_l = h_l e^{jS_0}$ with $S_0 = \mathbf{k}\cdot\mathbf{V}$, which actually induces the Doppler shift. And the resonance condition becomes:

[5] acronym for Wentzel Kramers Brillouin cf [3]

$$l\omega_c(x_g^*) = \omega + \mathbf{k}\cdot\mathbf{V} \tag{2.23}$$

This point will have to be checked later when we will study the mode structure to determine the respective scales of variation of the phase and of the amplitude. With the method of steepest descent, the phase $\theta = \int (l\omega_c - \omega - \mathbf{k}\cdot\mathbf{v_g})\, dt$ is developed around a stationary point:

$$\theta = \theta(x_g^*) + \dot{\theta}(t-t^*) + \frac{1}{2}\ddot{\theta}(t-t^*)^2 + \frac{1}{6}\dddot{\theta}(t-t^*)^3 \tag{2.24}$$

where x_g^* and t^* are the position and the time of stationary point in the trajectory of the guiding center.

In this equation, $\ddot{\theta} = \dot{\omega_c}$ and $\dddot{\theta} = -\ddot{\omega_c}$. We have two cases to consider:

- $\ddot{\theta} \neq 0$ which is the standard interaction of a particle crossing a resonance layer
- $\ddot{\theta} = 0$ which represents a tangential interaction: the particle orbit becomes tangent to the resonance layer.

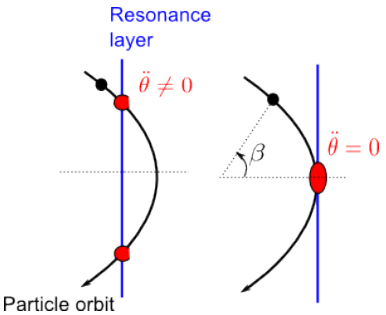

Figure 2.4: Classical and tangential interaction of a particle.

This is an important topic for ICRF heating but also for our ICE study because the interaction is increased by the longer time spent by the particle at the resonance and the phase can in this case be written:

$$\Pi(\theta) = e^{j\theta_0} 2\pi \left(\frac{2}{\dddot{\theta}^2}\right)^{1/3} A_i\left[-\frac{1}{2^{2/3}}\frac{\ddot{\theta}^2}{\dddot{\theta}^{4/3}}\right] \tag{2.25}$$

where A_i is the Airy function and θ_0 is the initial phase.

This formula represents the interaction time of the particle with the wave. As pointed out by [34], the tangential interactions will enhance the growth rate because of their longer duration. For the purpose of simplification in this study, the numerical calculations will be carried out without this term ($\Pi \approx \tau_b$). For future studies, it will be important to add it.

Finally, after integration of 2.20, we arrive to an expression of h_N which represents the Hamiltonian of the interaction between a particle and a single wave mode (l, N).

$$\boxed{h_N = eZv_\perp[E_+ J_{l-1}(k_\perp\rho_L) + E_- J_{l+1}(k_\perp\rho_L)]\Pi(\theta)/\tau_b} \tag{2.26}$$

This Hamiltonian also represents the change of energy of the particle and its sign will depend on the initial phase θ_0 present in the term $\Pi(\theta)$. The study of a single particle is not sufficient to conclude on the excitation or absorption of energy by a wave. We have to consider a whole population of particles and establish the statistics on it. This

is the purpose of the next section. But before, we make a last remark on the term $\Pi(\theta)/\tau_b$: it represents the ratio of the interaction time over the drift period, a term which is typical of the toroidal models ([30], [34]) and which is not taken into account in the homogeneous straight-line models. Its influence is twofold: on one hand, it will globally decrease the intensity of the interaction in comparison with the straight-line models, because it is lower than 1; but, on the other hand, it will distinguish the particles that have orbits tangent to the area of interaction with the wave from those with orbits that only intersect it.

2.1.4 *Interaction of a wave with a population of particles*

In the angle/action space, the density of a given type of particles (thermal ions and electrons, fast ions) is given by $F(\mathbf{J},\mathbf{\Theta},t)d\mathbf{J}d\mathbf{\Theta}$ where F is called the distribution function. The dynamics of this function obeys the Fokker-Planck equation in phase space:

$$\frac{\partial F}{\partial t}+\frac{\partial}{\partial \mathbf{J}}\cdot<\frac{\delta \mathbf{J}}{\delta t}>F+\frac{\partial}{\partial \mathbf{\Theta}}<\frac{\delta \mathbf{\Theta}}{\delta t}>F=0 \tag{2.27}$$

where $\delta\mathbf{J}$ and $\delta\mathbf{\Theta}$ are increments of actions and angles during a time δt and $<$ .. $>$ is the average on the population. These increments are given by the Hamilton equations 2.2, which gives the Vlasov equation:

$$\frac{dF}{dt}=\frac{\partial F}{\partial t}+\frac{\partial H}{\partial \mathbf{J}}\cdot\frac{\partial F}{\partial \mathbf{\Theta}}-\frac{\partial H}{\partial \mathbf{\Theta}}\cdot\frac{\partial F}{\partial \mathbf{J}}=0 \tag{2.28}$$

Using again the perturbative apporach, we can develop the Equation 2.28 in terms of V/H_0. The first order gives the fast response of the particles and the second order will give the slow, secular, evolution of the distribution function. At the first order, the distribution function F can be decomposed in $F=F_0(\mathbf{J})+f(\mathbf{J},\mathbf{\Theta},t)$, the first term being of order 0 in V/H_0 and the second of order 1. Injecting this development in the Vlasov equation and retaining only terms of order 1, we get:

$$\frac{\partial f}{\partial t}+\mathbf{\Omega}(\mathbf{J})\cdot\frac{\partial f}{\partial \mathbf{\Theta}}=\frac{\partial V}{\partial \mathbf{\Theta}}\cdot\frac{\partial F_0}{\partial \mathbf{J}} \tag{2.29}$$

where $\mathbf{\Omega}(\mathbf{J})=\frac{\partial H_0}{\partial \mathbf{J}}$.

To solve this equation, we proceed as for V with a Fourier development of f:

$$f=\sum f_N(\mathbf{J})expj(\mathbf{N}\cdot\mathbf{\Theta}-\omega t)$$

and we substitute it into Equation 2.29:

$$\begin{aligned}\frac{f_N}{V_N}&=\frac{\mathbf{N}\cdot\frac{\partial F_0}{\partial \mathbf{J}}}{\mathbf{N}\cdot\mathbf{J}-(\omega+j\eta)}\\&=\frac{\mathbf{N}\cdot\frac{\partial F_0}{\partial \mathbf{J}}}{\mathbf{N}\cdot\mathbf{J}-\omega}+j\pi\delta(\mathbf{n}\cdot\mathbf{\Theta}-\omega)\mathbf{N}\cdot\frac{\partial F_0}{\partial \mathbf{J}}\end{aligned} \tag{2.30}$$

We have used in the last equation the Plenelj formula that wraps the causality effects in the formal transformation $\omega\rightarrow\omega+j\eta$ where η represents an infinitely small artificial damping term.

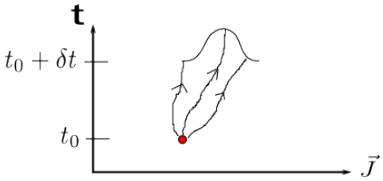

Figure 2.5: From an initial point in phase space, the Fokker Planck gives the probability to get different states at a later time.

The perturbation f of the distribution function F induces a current $\mathbf{j} = ZeN_0 < \mathbf{v} >$ where N_0 is the number of particles and the integral of F_0. The average velocity is defined by:

$$< \mathbf{v} >= \int (\mathbf{p} - \mathbf{A_0} - \mathbf{a})(F_0 + f) d\mathbf{J} d\mathbf{\Theta} \tag{2.31}$$

By keeping the first order terms in V/H_0, this equation provides us with a relation between the current and the electrical field. Defining the **dielectric tensor** $\boldsymbol{\epsilon}$ by:

Here again with have changed the units to normalize with respect to the mass m and the charge e.

$$\mathbf{j} = \epsilon_0(\boldsymbol{\epsilon} - \mathbf{I})\mathbf{E} \tag{2.32}$$

ϵ_0 is the vacuum constant and $\mathbf{I}$ is the unit diagonal matrix.

we can express it in function of the Fourier components of the perturbed Hamiltonian and of the unperturbed distribution function:

$$\boxed{\boldsymbol{\epsilon} = (1 - \frac{\omega_p^2}{\omega^2})\mathbf{I} - \frac{\omega_p^2}{\omega^2} \sum_N \int \frac{V_N^* V_N}{\mathbf{N} \cdot \mathbf{\Omega} - (\omega + j\eta)} L_N F_0 d\mathbf{J}} \tag{2.33}$$

where * represents the conjugate.

where we have defined:

$$L_N = \mathbf{N} \cdot \frac{\partial}{\partial \mathbf{J}} \tag{2.34}$$

which represents the derivative operator along the characteristics of interaction in phase space and where V_N is given by 2.26. The first term of Equation 2.33 represents the fluid response of the plasma and the second term, the gyrokinetic response. $\boldsymbol{\epsilon}$ characterizes the local response of the plasma. Written in function of the actions $\mathbf{J}$, we can establish the relation between the global trajectories (characterized by the invariants and angles) and the local interaction. This is the main advantage of the Hamiltonian to formulate in a clear manner this relation. With Formula 2.33, we develop the properties of the waves supported by the population of ions F. This is valid as well for electrons, ions, thermal or suprathermal. There is also no limitation on the type of wave excited, electrostatic as well electromagnetic.

If we decompose $\boldsymbol{\epsilon}$ in its Hermitian and anti-Hermitian parts: $\boldsymbol{\epsilon} = \boldsymbol{\epsilon}^H - j\boldsymbol{\epsilon}^A$, we see that a part of the current is in phase opposition and the other is in phase. The first part corresponds to a reactive exchange between the particles and the wave that supports the adiabatic propagation of the latter. The second part is an active transfer of power and leads to the absorption or the excitation of the wave by the particles. We will now have a more detailed look at each part, but we will keep the formulas general. The proper application to the waves of interest for ICE will come in section 2.2.1.

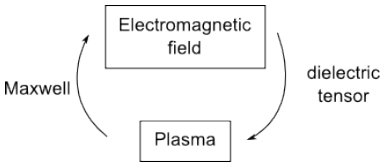

Figure 2.6: Coupling between plasma and electromagnetic field.

Wave propagation

The dielectric tensor gives the response of the particles to an electromagnetic field. The movement of these particles will in turn, following Maxwell Equations 1.10 - 1.13, affect the electromagnetic field. Using the Maxwell-Faraday and Maxwell-Ampere equations, we can obtain the equation of propagation of the wave:

$$\mathbf{D} \cdot \mathbf{E} = \frac{\omega^2}{c^2}[\mathbf{N} \times (\mathbf{N} \times \mathbf{E}) + \boldsymbol{\epsilon}(\omega)\mathbf{E}] = \mathbf{0} \tag{2.35}$$

$\mathbf{D}$ is called the dispersion tensor and $\mathbf{N} = \frac{c}{\omega}\mathbf{k}$ the wave number and $\mathbf{k}$ is the wave vector. The propagation equation has a solution when its determinant $det(\frac{c^2}{\omega^2}\mathbf{D}) = 0$. This gives the dispersion relation between ω and $\mathbf{N}$.

Transfer of power The balance of power is given by:

$$\frac{\partial W}{\partial t} + \boldsymbol{\nabla} \cdot \mathbf{S} = -\frac{\omega}{8\pi}\mathbf{E_0}^* \cdot \boldsymbol{\epsilon}^A(\mathbf{k}, \omega) \cdot \mathbf{E_0} \tag{2.36}$$

where we define the reactive energy stored in the wave:

$$W = \frac{1}{16\pi}[|\mathbf{B_0}|^2 + \mathbf{E_0}^* \cdot \frac{\partial(\omega\boldsymbol{\epsilon}^H)}{\partial\omega} \cdot \mathbf{E_0}] \tag{2.37}$$

and $\mathbf{S} = \mathbf{S_0} + \mathbf{T}$ with the **Poynting vector**:

$$\mathbf{S_0} = \frac{c}{8\pi} Re(\mathbf{E_0}^* \times \mathbf{B}) \tag{2.38}$$

and the kinetic part of the power flux:

$$\mathbf{T} = -\frac{\omega}{16\pi}\mathbf{E_0}^* \cdot \frac{\partial\boldsymbol{\epsilon}^H}{\partial\mathbf{k}}\mathbf{E_0}. \tag{2.39}$$

Consequently, the power dissipated by the wave is given by:

$$P_{abs} = \frac{\omega}{8\pi}\mathbf{E_0}^* \cdot \boldsymbol{\epsilon}^A \cdot \mathbf{E_0} \tag{2.40}$$

We can relate it to the dispersion Equation 2.35 by noting that the growth rate of a wave instability is given by:

$$\gamma = Im(\omega_0(\mathbf{k_0})) = \frac{Im(D(\omega_r, \mathbf{k_0}))}{(\frac{\partial D}{\partial\omega})_{k=k_0}} \tag{2.41}$$

which leads to the general definition of the growth rate:

$$\gamma = -\frac{P_{abs}}{2W} \tag{2.42}$$

In a more heuristic way, we can write the power balance equation of an instability in the following form:

$$\frac{dW}{dt} = 2(\gamma - \gamma_{damping})W - L - C_{nl} \tag{2.43}$$

where W is the energy of the wave, γ is the growth rate previously defined, $\gamma_{damping}$ corresponds to the absorption of the wave by different mechanisms (Landau, cyclotron dampings), L corresponds to the losses (by convection, radiation outside the plasma) and C_{nl} is the non-linear coupling with other waves (through parametric decay instability for instance; cf [47]).

2.1.5 *Evolution of the distribution function*

The dielectric tensor gives the local fast response of the plasma perturbation. The second step is to analyze the effect of the perturbation on the ion population in the long term [6], its secular effect. This corresponds to the development at the second order in V/H_0 of the

[6] Long term means here long with respect to the frequency ω and the time scale $\frac{\partial H_0}{\partial \mathbf{I}}$ of the unperturbed system

Vlasov Equation 2.28. We assume that the Random Phase Approximation (RPA) (more details in [1]) is valid and that we can average on the phase angles Θ of the different particles. Then, we can write the Fokker-Planck equation in the form:

$$\frac{\partial F}{\partial t} = -\frac{\partial}{\partial \mathbf{I}} \cdot \frac{< \delta \mathbf{I} >_{\Theta_0}}{\delta t} F + \frac{\partial}{\partial \mathbf{I}} \cdot \frac{\partial}{\partial \mathbf{I}} \frac{< \delta \mathbf{I} \delta \mathbf{I} >_{\Theta_0}}{2\delta t} F \tag{2.44}$$

We can now use the **Einstein relation** ([48]): $< \delta \mathbf{I} >_{\Theta_0} = \frac{\partial}{\partial \mathbf{I}} \cdot \frac{\partial}{\partial \mathbf{I}} \frac{<\delta \mathbf{I} \delta \mathbf{I}>_{\Theta_0}}{2}$ to get the evolution of F:

$$\frac{\partial F}{\partial t} = \frac{\partial}{\partial \mathbf{I}} \cdot \frac{\partial}{\partial \mathbf{I}} \frac{< \delta \mathbf{I} \delta \mathbf{I} >_{\Theta_0}}{2\delta t} \cdot \frac{\partial}{\partial \mathbf{I}} F \tag{2.45}$$

As done for the wave in the section 2.1, $\delta \mathbf{I}$ is developed at the first order in V/H_0 and Fourier-transformed to get the following result:

$$\frac{\partial}{\partial \mathbf{I}} \cdot \frac{\partial < \delta \mathbf{I} \delta \mathbf{I} >_{\Theta_0}}{2\delta t} + \sum_N \frac{\pi}{2} \frac{q^2}{\omega^2} N \cdot N |E.V_N|^2 \delta(\Omega) \tag{2.46}$$

and the evolution equation for F is therefore:

$$\frac{\partial F}{\partial t} = \frac{\pi}{2} \frac{q^2}{m^2 \omega^2} \sum_N L_N \cdot |V_N \cdot E|^2 \delta(\Omega) L_N \cdot F \equiv D_{QL}(F) \tag{2.47}$$

This equation corresponds to a diffusion in phase space of the population of fast ions under the action of the ICE. $D_{QL}(F)$ is called the Quasi-Linear Diffusion operator. We have the same type of operator in the case of ICRF heating (Cf. Chapter 2.2.2), the difference being the direction of diffusion: for ICRF, the wave gives its energy to the ions and "pushes" them to higher energies; for ICE, the waves extract energy from them and diffuse them to lower energies. The Equation 2.47 deals only with the ICE interaction; in a realistic case, we have to add terms corresponding to the source of fast ions (fusion reactions), the collisions and the diffusion by ICRF heating. Thus, we can write a general form for the evolution of the distribution function F:

$$\frac{\partial F}{\partial t} = S + C(F) + D_{QL}(F) + D_{ICRF}(F) \tag{2.48}$$

where S is the source term, $C(F)$ is the collision term, that we will see in section 2.2.2 and $D_{QL}(F)$ is the previously derived Quasi-Linear Diffusion operator and $D_{ICRF}(F)$ is the diffusion operator for ICRF.

The set of equations 2.43 and 2.48 constitutes a closed system that makes it possible to model the coupled evolution of the wave and of the distribution function. This is of course valid if the quasi-linear approximation is verified, which requires a "not too large" growth rate in comparison with the drift period and the validity of the Random Phase Approximation (RPA). The first requirement is a major point of controversy between the gyrokinetic theory of Gorelenkov [30] which respects it and the straight-line homogeneous theory of Dendy [17] which supposes a fast growth rate. In the first case, we have a retro-action loop between waves and exciting particles, in the second case, a saturation mechanism is required, either non-linear coupling, or wiping out of particles or wiping out of the wave. We will use the results from AUG to check the validity of the model presented here.

2.2 *Application to the ICE theory*

We have now presented the general theoretical tools to study particles/waves interactions in the ion cyclotron range of frequency. We now apply them to the case of ICE. We recall that there are four types of ICE which can take place either in the center or at the edge, either with fusion products, beam ions or ICRF-accelerated ions. We have seen that the Hamiltonian formalism constitutes a general approach of the particle trajectories and of the interactions, which makes possible to address the four types of ICE with this common framework.

The central element of the analysis is based on the transfer of energy between a population of fast particles and a wave (or a group of waves), which is obtained by the anti-hermitian component of the dieletric tensor 2.33. It is made of three fundamental components:

- A resonance condition $\omega = \omega_c + \mathbf{k} \cdot \mathbf{v_g}$ which imposes a strong constraint between the parameters of the distribution function and the structure of the wave: only ions with a given velocity and reaching the resonance layer will be able to trigger a wave with a given frequency.
- a gradient of the distribution function represented by the term L_N: it is the characteristics of the interaction in the state space: the evolution of the distribution function along these characteristics will determine the sign of the integral and the direction of the power transfer.
- A mode structure characterized by its spatial characteristics (localization, extension) and by its frequency and its wavenumber.

Our main task is to characterize each of these components and their relations. But, before starting, we summarize the limits of the Hamiltonian model:

- it is a perturbative approach: $V \ll H_0$, which means that only weak instabilities can be considered,
- the model is linear: no saturation effect is considered,
- the Larmor radius of a particle is smaller than the resonance layer: the ion resonates during at least a complete gyration.

Taking these limits into account, we will follow these steps to investigate each type of ICE:

1. Identification and characterization of the waves able to interact with the ions and to support the growth of the instability; these waves must have a phase velocity lower or approximately equal to the velocity of the fast ions in resonance. Either they are electromagnetic, Alfvén-like, with a group velocity equal to the Alfvén velocity v_a (which is the case for FP-ICE or m-ICE) or they are far slower and are thus electrostatic (case of beam-driven ICE). We will determine the spatial characteristics of the wave amplitude,

the frequency and the wavenumber. The local or global (with eigenmodes) character of the wave will also be a point of analysis. The attenuation of the wave by damping on thermal ions and electrons will also be estimated in a local approach.

2. Identification of the fast ions population with a reserve of free energy. They must be able to meet the resonance conditions and to provide a source of energy to the wave at the location of the interaction.

3. Estimation of the growth rate and impact on the operational parameters to trigger the emission; analysis of its resulting characteristics in time and frequency domain.

4. Analysis of the long term evolution of the emission and of the fast ion population. The characteristics of the interaction L_N also define the quasi-linear trajectory in phase space of the distribution function on a longer time scale. The purpose is to evaluate if the evolution leads to saturation of the signal, to the quasi-linear evolution of the distribution or to its complete elimination at the edge.

2.2.1 *Plasma waves in the ICRF range of frequencies*

We will consider the existence and propagation of two types of waves: electromagnetic and electrostatic; the first ones can be excited by super-alfvénic or near super-alfvénic particles and the other by less energetic fast ions (from the beam).

A. Compressional Alfvén waves in a tokamak

We will investigate the propagation by following these steps:

1. We first study a local case to get a better understanding of the underlying physics. We look only at the cold background plasma to get the relation of dispersion.

2. The hot plasma effect near the resonances is then studied, still in the local approach.

3. We have a brief look at the effect of the fast ions on the structure of the waves to check that we can neglect them without loss of information.

4. We turn on to the tokamak configuration where we will consider waves with a dominant radial wavenumber (which is the typical case for the ICRF wave and maybe for central ICE) and with a dominant poloidal wavenumber, revealing eigenmodes localized at the edge of the plasma (and probably playing a role for the FP-ICE and the m-ICE).

5. To finish, we will deal with the damping of these waves by thermal electrons and ions through Landau/TTMP[7] and cyclotron interaction.

[7] TTMP: Transit Time Magnetic Pumping

Local case

We consider a homogeneous collisionless, magnetized, cold plasma. We have a constant magnetic field $\mathbf{B_0} = B_0\mathbf{z}$ and we look for perturbations of the form:

$$\mathbf{E_1}(t, y) = \mathbf{E_1} e^{j(\mathbf{k}\cdot\mathbf{x} - \omega t)}$$

where $\mathbf{k} = k_\perp \mathbf{y} + k_\parallel \mathbf{z}$.

We consider a range of frequency $\omega_{ce} \gg \omega \geq \omega_{ci}$ and plasma parameters with $\omega_{pi} \gg \omega_{ci}$. We could directly use the results of section 2.1.3 in the straight field case using a Dirac function for the distribution function (which corresponds to the cold plasma approximation), but to get a better insight in the physics we consider a two-fluids model with electrons and ions which verify the Newton equation[8]:

[8] the subscript 0 corresponds to the static field and 1 to the perturbation

$$-j\omega \mathbf{v_{s1}} = \frac{q_s}{m_s}(\boldsymbol{E_1} + \mathbf{v_{s1}} \times \mathbf{B_0}) \tag{2.49}$$

where $s = e, i$. We can neglect for these frequencies the electron inertia:

$$v_{e1x} = \frac{E_{1y}}{B_0} \qquad\qquad v_{e1y} = -\frac{E_{1x}}{B_0} \tag{2.50}$$

For ions, keeping all terms, we get:

$$v_{i1x} = \frac{jq_i}{\omega m_i}[\frac{E_{1x} + (j\omega_{ci}/\omega)E_{1y}}{1 - \omega_{ci}^2/\omega^2}] \tag{2.51}$$

$$v_{i1y} = \frac{jq_i}{\omega m_i}[-j\frac{E_{1x} + (j\omega_{ci}/\omega)E_{1y}}{1 - \omega_{ci}^2/\omega^2}] \tag{2.52}$$

$$v_{i1z} = \frac{jq_i}{\omega m_i} E_{1z} \tag{2.53}$$

From the velocities, we determine the current that is used in the Maxwell equations to get the wave equation

$$\boldsymbol{\nabla}(\boldsymbol{\nabla} \cdot \mathbf{E_1}) - \boldsymbol{\nabla}^2 \mathbf{E_1} = j\omega\mu_0 \mathbf{j}$$

The determinant of this equation is zeroed to get the dispersion relation taking into account the quasi-neutrality condition: $\frac{\omega_{pi}^2}{\omega\omega_{ci}} = -\frac{\omega_{pe}^2}{\omega\omega_{ce}}$; we obtain the following quadratic equation in ω^2:

$$\omega^4 - \omega^2[k^2 v_A^2 + k_\parallel^2 v_A^2(1 + \frac{k^2 v_A^2}{\omega_{ci}^2})] + (k_\parallel v_A)^2(k^2 v_A^2) = 0$$

For $k_\parallel \ll k_\perp$, we find two roots in ω^2:

$$\omega^2 \approx k_\parallel^2 v_A^2 \qquad \text{Slow wave} \tag{2.54}$$

$$\omega^2 \approx k_\perp^2 (v_A^2 + k_\parallel^2 D_H^2) \qquad \text{Fast wave} \tag{2.55}$$

where $D_H = v_A^2/\omega_{ci}$ *and* v_A *is the Alfvén velocity.*

The first solution corresponds to the shear Alfvén wave and the second, in case of $k_\parallel = 0$ to the compressional Alfvén wave. The $k_\parallel \neq 0$ correction corresponds to the whistler branch and the wave takes the name of magnetoacoustic wave. It will be useful for the analysis of the CAE. A scheme of the dispersion relation of the two

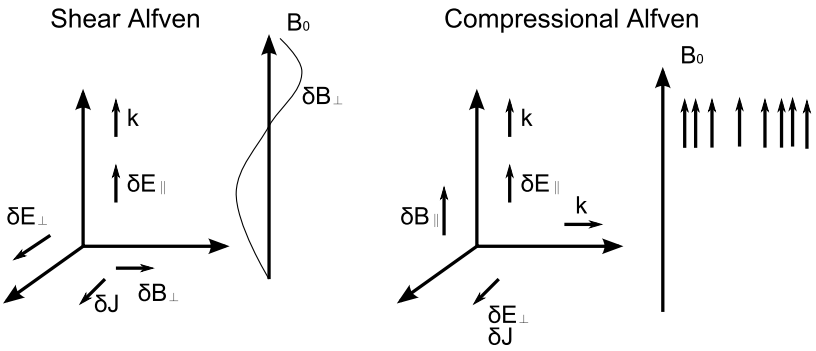

Figure 2.7: Spatial structure of the Alfvén waves.

Alfvén waves is presented on the Figure 2.7, and the spatial structure, on Figure 2.8.

It is also straightforward to get the dielectric tensor for these waves:

$$\epsilon(\omega) = \begin{pmatrix} \epsilon_\perp & -j\epsilon_x & 0 \\ \epsilon_x & \epsilon_\perp & 0 \\ 0 & 0 & \epsilon_\parallel \end{pmatrix} \tag{2.56}$$

where we define:

$$\epsilon_\perp = 1 - \frac{\omega_{pe}^2}{\omega^2 - \omega_{ce}^2} - \frac{\omega_{pi}^2}{\omega^2 - \omega_{ci}^2} \tag{2.57}$$

$$\epsilon_x = \frac{\omega_{ce}}{\omega}\frac{\omega_{pe}^2}{\omega^2 - \omega_{ce}^2} - \frac{\omega_{ci}}{\omega}\frac{\omega_{pi}^2}{\omega^2 - \omega_{ci}^2} \tag{2.58}$$

When $k \to +\infty$, we have a resonance where absorption and conversion of the wave takes place; the cold plasma approximation breaks down. When $k \to 0$, we have a cutoff and the wave becomes evanescent or is reflected.

The polarization of the fast wave is given by:

$$\frac{E_x + jE_y}{E_x - jE_y} = \frac{n_\parallel^2 - \omega_{ci}/(\omega + \omega_{ci})}{n_\parallel^2 - \omega_{ci}/(\omega - \omega_{ci})} \tag{2.59}$$

It is an elliptical polarization and we note that it becomes zero near the cyclotron frequency.

Hot plasma effects and fast ions

We stay in the homogeneous straight-line approximation to have a look at the hot plasma effects on this magneto-acoustic wave, i.e., when we approach the second harmonic and above, and when we take into account the effect of fast ions on the propagation. To do that, we use the dielectric tensor given in this approximation by Equation 2.10. For the background thermal ions, we use a classical Maxwellian function for their distribution, which gives ([6]):

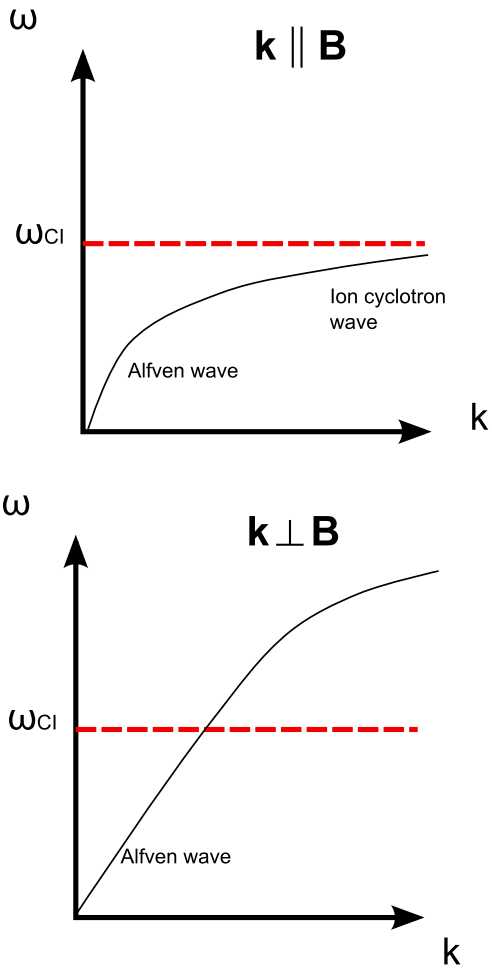

Figure 2.8: Representation of the dispersion relations for the shear and compressional Alfvén waves.

$$\epsilon^i_{11} = \frac{\omega^2_{pi}}{\omega^2} \sum_l \frac{l^2 e^{-a_i} I_l}{a_i} \zeta_0 Z(\zeta_l) \tag{2.60}$$

$$\epsilon^i_{22} = \frac{\omega^2_{pi}}{\omega^2} \sum_l \left(\frac{l^2 e^{-a_i} I_l}{a_i} + 2a_i e^{-a_i}(I_l - I'_l)\right) \zeta_0 Z(\zeta_l) \tag{2.61}$$

$$\epsilon^i_{12} = i\frac{\omega^2_{pi}}{\omega^2} \sum_l l e^{-a_i}(I_l - I'_l) \zeta_0 Z(\zeta_l) \tag{2.62}$$

where Z is the plasma dispersion which appears when using Gaussian distribution function in the general dielectric tensor, $\zeta_l = (\omega - l\omega_{ci})/k_\parallel v_i$, $I_l = I_l(a_i)$ is the modified Bessel function of the first kind of order l and $a_i = k^2_\perp v^2_i / 2\omega^2_{ci}$.

For the population of fast ions, following the method of [25], we take a shifted Maxwellian distribution function that we apply to the dielectric tensor 2.33 written in velocity space:

$$\epsilon^\alpha_{ij} = \sum_N \frac{\omega^2_{p\alpha}}{\omega^2} \int d^3v v^2_\perp \frac{\boldsymbol{V_N} \boldsymbol{V_N}*}{\omega - \mathbf{k}\cdot\mathbf{v_g} - N\omega_{c\alpha}} L_N F \tag{2.63}$$

where α is the subscript for fast ions, $L_N = \omega \frac{\partial}{\partial E} + \frac{N\omega_{c\alpha}}{B_c} \frac{\partial}{\partial \mu}$ and $\mathbf{V_N}$ is defined by 2.10.

The sum of the two previous dielectric tensors gives the total response of the plasma (if we neglect the effect of electrons) and we can numerically calculate the dispersion relation 2.35 of waves near the cyclotron resonance. The result is displayed on Figure 2.9. It was obtained by calculating the value of the dispersion vector. The values in dark purple and white correspond to its zeros, therefore to the solutions of the dispersion relation.

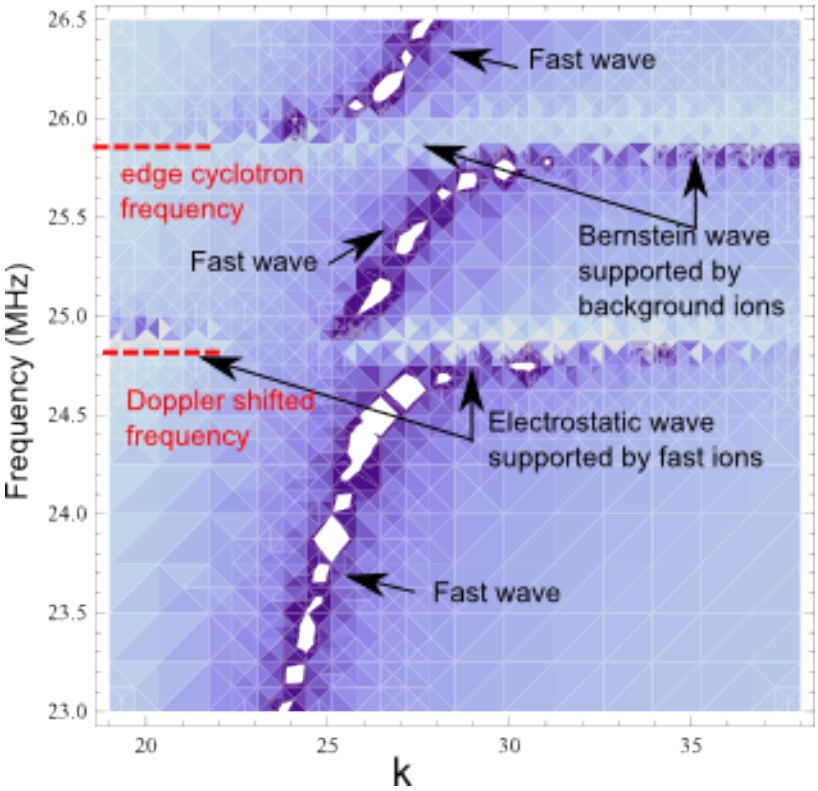

Figure 2.9: Calculated dispersion function of waves supported by background thermal ions and a small beam of fast ions of concentration 10^{-6} for $B = 1.7T$ corresponding to the edge of AUG. k is the wave vector. We sobserve the electrostatic modes corresponding to the mode conversion near the 1st harmonic of the cyclotron frequency of the thermal ions and the electrostatic modes supported by the fast ions near the Doppler-shifted resonance.

The main mode visible is the fast wave with its linear dispersion relation. Near the 1st harmonic of the cyclotron frequency of the background ions, we have the typical mode conversion which is normally used for ICRF operations, where the fast wave is converted to

a Bernstein wave with a high $k_{\|}$. At a frequency corresponding to the cyclotron frequency of the fast ions in their moving referential (i.e. Doppler shifted), we have another mode conversion. This is where the cyclotron emission takes place. So, to be absolute rigorous, an electrostatic component should be taken into account in the computation of the interaction. However, we will suppose that this part is negligible since it will be relatively quickly damped on the electrons due to its high parallel wave vector. We retain in our assumption only the magneto-acoustic component to study the toroidal case.

Global case: Compressional Alfvén Eigenmodes (CAE). The interest for the modes localized at the edge is threefold: the source of the observed FP-ICE and m-ICE signals originates from the edge mid-plane, the damping of waves is lower there because of the lower densities and temperatures and the eigenmodes can act as an amplifier of the signal if the instability is weak. To get an edge localization, we have to look for waves with a poloidal propagation higher than the radial one: $k_p \gg k_r$.

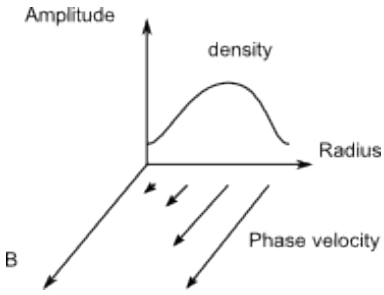

Figure 2.10: Attenuation of the shear Alfvén wave in a cylinder geometry due to the variation of the phase velocity along the radius.

Important note These modes are different from the more famous Toroidal Alfvén Eigenmodes (TAE). These latter are due to the shear Alfvén wave which has a parallel propagation $\omega = k_{\|} v_A$. In a cylindrical configuration, the dispersion relation evolves continuously in function of the radius due to the dependence on the magnetic field. As a result, it disperses very rapidly (cf. Figure 2.10).

But in a toroidal configuration, the wave sees a periodic variation of the density along the helical magnetic line (see Figure 2.11) and, like gaps in a transmission line with a periodic index, waves interferes and we have amplification at the gap modes (like the Bragg frequency).

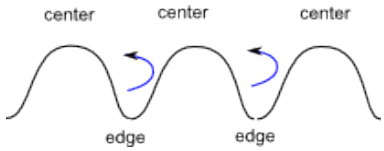

Figure 2.11: In toroidal configuration, the shear waves reflect on the repeated change of density along the magnetic line and interfere.

For a start, we take the simple case of a plasma cylinder with a constant magnetic field and a density profile peaking in the center. The case can be treated with a 1D model obtained by writing the wave propagation Equation 2.35 for the magnetosonic wave in cylindrical coordinates:

$$\frac{d^2E}{dr^2} + \frac{1}{r}\frac{dE}{dr} + \left(\frac{\omega^2}{v_A^2(r)} - k^2\right)E = 0 \tag{2.64}$$

where $k^2 = k_p^2$ (we are interested in modes where $k_r \ll k_p$ and $k_{\|} \ll k_p$ to get a confinement near the edge without risk of damping). Because of the poloidal symmetry, we can write k_p in the form $k_p = \frac{m}{r}$. We suppose that E vanishes at the edge $r = a$ (purely confined mode) and we take the density profile of the form $n_i(r) = n_0(1 - r^2/a^2)^{\sigma}$. The existence of a solution is guaranteed by the condition

$$\frac{\omega^2}{v_A^2(r)} - k^2 > 0$$

which means the formation of a potential well represented on Figure 2.12. A solution can be found numerically and the result is given on Figure 2.13.

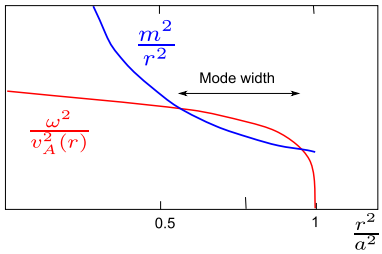

Figure 2.12: Representation of the potential well constrained by the evolution in m/r of k and by the density profile.

When we consider the toroidal configuration, the density and the magnetic field are now function of the poloidal angle θ. There are two possibilities to find the solutions:

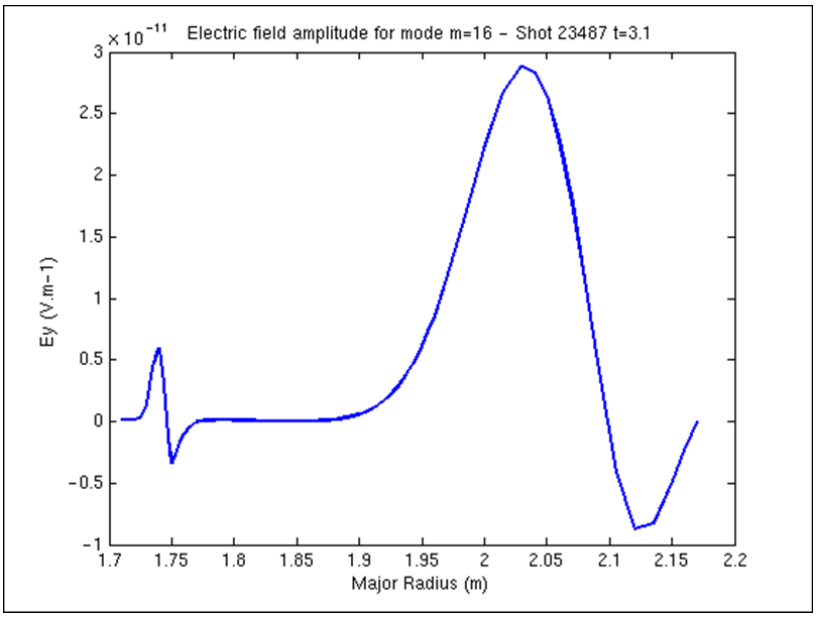

Figure 2.13: Solution of Equation 2.64. with density profile and radius from ASDEX Upgrade.

- the use geometry optics, considering short wavelengths. The ray trajectories

$$\frac{dx}{dt} = \frac{\partial \omega}{\partial k} \propto \frac{k}{\omega v_A^2} \tag{2.65}$$

$$\frac{dk}{dt} = -\frac{\partial \omega}{\partial x} \propto -\frac{k}{\omega}\frac{\partial v_A}{\partial x} \tag{2.66}$$

  can be calculated and we check that they are closed when they come back to the starting point. This is the method used by Coppi([13]).

- The second solution is the direct solving of the wave Equation 2.35 in cylindrical coordinates, assuming a constant poloidal number and a poloidally varying radial electric field. It is the method used by Kolesnichenko ([43]) and we will use it for a numerical model of the CAEs. The advantage is that it directly gives the frequency and the amplitude of the wave required to get the growth rate.

Hellsten ([36]) used a combination of both methods, using geometry optics in the poloidal direction (with varying k_p) and a solution of the wave equation in the radial direction. The coherence between the two models is insured by checking the energy balance in a toroidal section.

The detail of the model is presented in the appendix 1 and we refer the reader to it to have the full mode equations. The essence of the physics related to the toroidicity is caught in the equation:

$$\frac{\partial^2 B_\parallel}{\partial r^2} - (k_p^2 - \frac{\omega^2}{v_A^2} + k_p \frac{\omega}{\omega_{ci}} \frac{n_i'}{n_i}) B_\parallel = 0 \tag{2.67}$$

A term in n_i'/n_i appears and is related to the whistler component of the wave. It introduces a constraint on the poloidal mode number to

insure the existence of a potential well. Another important remark is that we used the dielectric tensor of the magnetoacoustic wave which is, strictly speaking valid only for $\omega \geq 3\ \omega_{ci}$. However, we will use it down to $2\omega_{ci}$ (as done in [30]).

We use our *CAE2D* model to compute the modes. An exemple is given on the Figure 2.14.

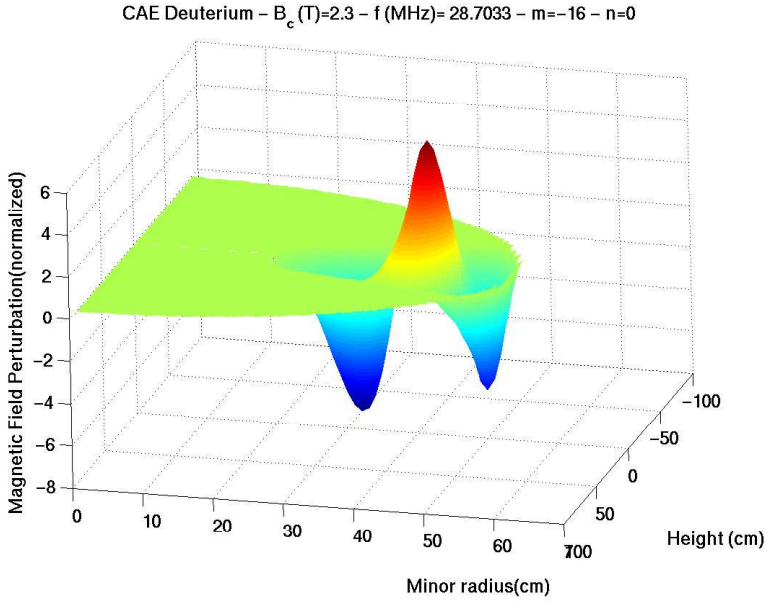

Figure 2.14: Spatial structure of the mode m=-16, n=0 envelope for a central density profile $n_{i0} = 3.8 \cdot 1^{19} m^{-3}$. It is represented for a half section of the plasma.

The main parameters that control the mode structure are the magnetic field, the density profile and the ellipticity. It is interesting to do a parametric study of the modes in function of these parameters. However, the use of this 2D code is time consuming and not adapted to a parametric study of the modes. Therefore, we used an analytical solution from [27] by variational analysis of the wave equation. The wave frequency ω_0 is then given in function of k by:

$$\omega_0 = \frac{|m| v_A}{\kappa r} \{ \frac{sgn(m) v_A n_i'}{2\omega_{ci} n_i} + [(1 + K_n) + (\frac{v_A n_i'}{2\omega_{ci} n_i})^2]^{1/2} \}_{r=r_0} \quad (2.68)$$

This analytical formula is used to get the mode structure and to compare it for some points with the results of the 2D code. We have also used a simplified model for the plasma density profile defined by:

$$n_i = n_{i0}(1 - (\frac{r}{a})^{\sigma_1})^{\sigma_2} \quad (2.69)$$

But, first, we examine the potential well function, which controls the existence and location of the solution. The Figure 2.15 presents the effect of the poloidal mode on the size (in the radial direction) of the potential well. We notice that, for the range of parameters used on ASDEX Upgrade (see section 3.1.1), there is no potential well for positive values of m. This asymmetry comes, as noted previously, from the whistler component of the CAEs.

We now turn on to the main point of our mode study: the presentation of the mode structure, i.e., the dependency of the frequency

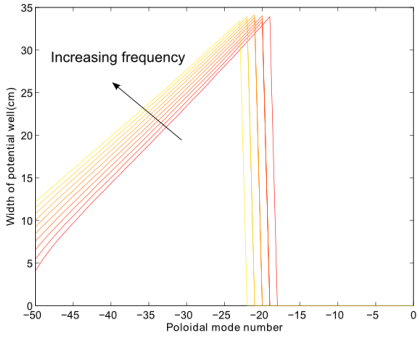

Figure 2.15: Evolution of the radial size of the potential well with respect to the poloidal number at different frequencies for standard ASDEX Upgrade parameters.

where $K_n = (v_A n)^2/(\omega_{ci} R)^2$, r_0 is the minimum of the potential well.

where n_{i0} is the central plasma density and σ_1 and σ_2 are two parameters chosen so that this model fits the density profiles measured with the IDA diagnostics.

on the poloidal and toroidal mode number. The result is given on Figure 2.16.

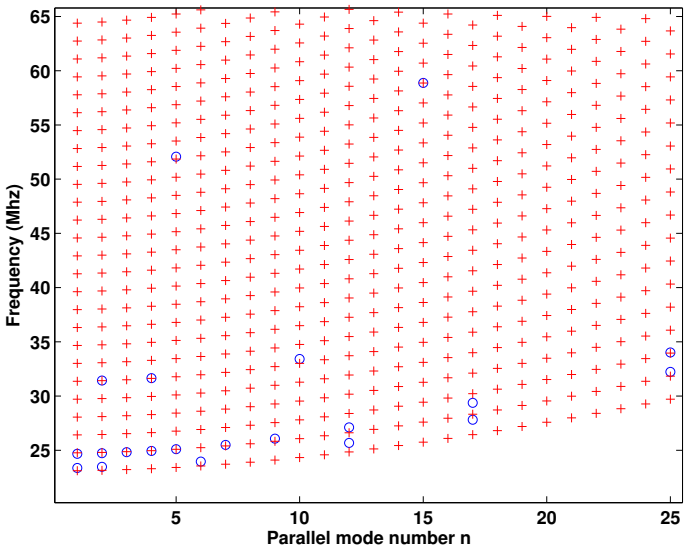

Figure 2.16: Mode structure of CAEs on ASDEX Upgrade. The red crosses are calculated with the analytical formula 2.68 and the blue dots are 2D solutions. At a given n, the different solutions correspond to decreasing values of m, the highest being -15.

The analytical solutions are very sensitive to the n_i'/n_i product which has to be chosen very carefully: we will see in the next section that a comparison with the measured mode structure is helpful to find the best solutions. We notice that they fit well with the 2D solutions for lower frequencies but that a shift appears with increasing n and m, due to the inaccuracy of the numerical model. As for the structure itself, it appears quite regular in poloidal mode number. The gaps between modes are regularly spaced for values of n above 10.

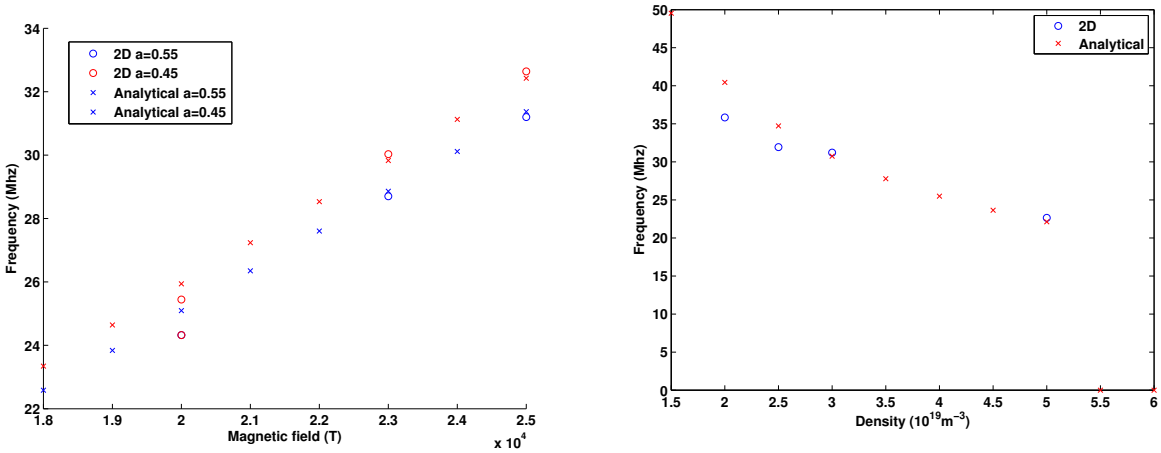

Figure 2.17: Evolution of the frequency of the mode m=15, n=0 with: *Left:* the magnetic field, *Right:* the density.

It is now interesting to see how the mode structure evolves with the plasma parameters. The main factors are the magnetic field and the density profile. In this case, we also compare with the results of the 2D code to check the relevance of the analytical formula. The

results are presented on Figure 2.17.

The last point to investigate is the localization of the mode and its spatial extent. We have done a parametric study of the radial borders of each mode in function of the poloidal number, of the toroidal number and of the density. The result is presented on Figure 2.18.

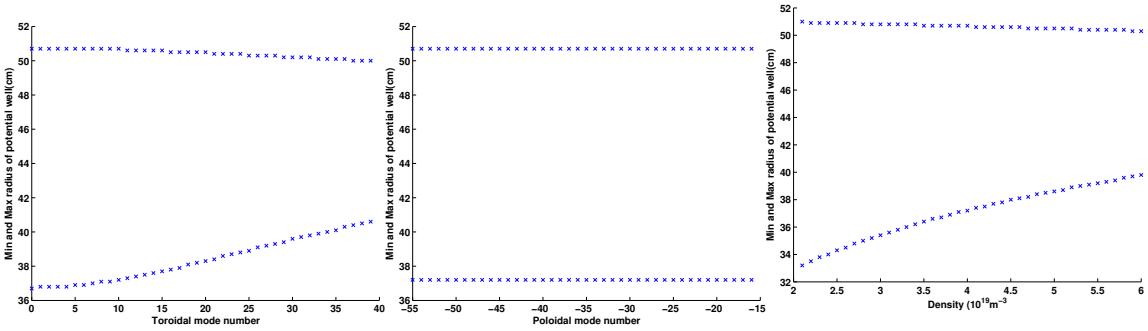

Figure 2.18: Evolution of mode spatial width with: *Left:* toroidal mode number; *Middle:* poloidal mode number; *Right:* density. Each line represents the location of the radial boundaries of the mode.

Absorption of CAEs

Once the structure of the modes is established, we have to check if any absorption mechanism can damp them and prevent their excitation. For the compressional wave, there are two main effects that can attenuate them:

- The Transit Time Magnetic Pumping (TTMP) which is due to the resonant absorption of the wave by the thermal electrons
- The cyclotron absorption which is due to the resonant interaction with the thermal ions. It is actually the mechanism used by the ICRF heating to transfer the power from the wave to the plasma.

We consider here only a local absorption without taking into account the toroidal effects. This is possible by assuming that we do not have a too large spatial variation of the eigenmode structure and that the number of thermal electrons in resonance with the waves is small. With this local approach, we can use the results from the section 2.1.3 in the case of an homogeneous straight line plasma and use the Equation 2.10 with thermal ions and electrons. We don't need to analyze all terms in n in this equations. The TTMP damping comes from the $n = 0$ term for electrons and the cyclotron absorption from the term $n = 1$.

Landau/TTMP damping

The argument of the Bessel function J_n in Equation 2.10 is called $\lambda = k_\perp^2 v_{th}^2 / 2\omega_c$ and represents the ratio of the wave vector to the Larmor radius. In the limit of a vanishing $\lambda \to 0$, the only contribution comes from the ϵ_{zz} term and is the source of the Landau damping; but, since the compressional wave has no parallel electrical field, this term is negligible. The highest term with $\lambda \neq 0$ is ϵ_{yy}. The force $\mu \cdot \nabla \mathbf{B}$ acts in this case on the electrons. The power transfered by the

wave to the electrons is given by:

$$P_{MP} = \frac{\omega}{8\pi}\beta_e \left|\frac{c}{\omega}\mathbf{k}_\perp \times \mathbf{E}_\perp\right|^2 \cdot \sqrt{\pi}\frac{\omega}{|k_\parallel| v_{te}} e^{-\frac{v^2}{k_\parallel^2 v_{te}^2}} \tag{2.70}$$

where $\beta_e = \frac{8\pi n_e T_e}{B^2}$.

The damping rate is then given for $\omega > \omega_{ci}$ by:

$$\gamma_e \approx -\omega \beta_e \zeta_e e^{-\zeta_e^2} \tag{2.71}$$

where $\zeta_e = \frac{\omega}{|k_\parallel| v_{te}}$.

We note that the two main factors driving the TTMP damping rate are the electron temperature (via v_{te}) and the parallel wave number $k_\parallel$. The higher they are, the stronger is the damping. As a result, two conditions are necessary to have a limited TTMP damping:

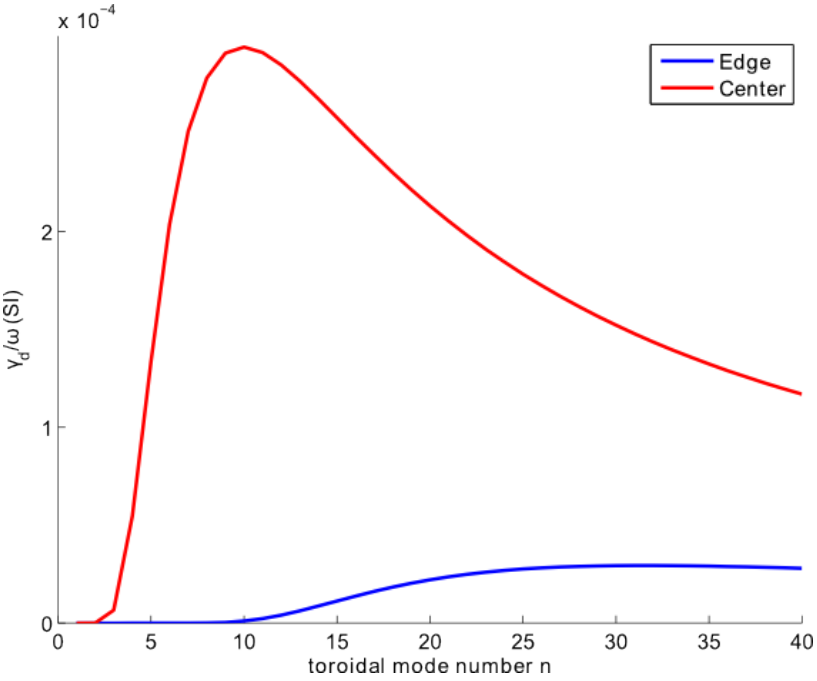

Figure 2.19: Damping rate due Transit Time in function of the toroidal mode number at the edge and in the center of the plasma for a frequency $\omega = 30\ MHz$. T(edge)=200 eV and T(center)=2 keV.

- a localization of the modes near the plasma edge where the electron temperature is lower,
- a small wave number. As a rule of thumb, the TTMP damping is considered negligible (or, more precisely, exponentially small) when we have $|k_\parallel| < \omega/v_{te}$, which is visible on Figure 2.19. For the case of the CAEs on ASDEX Upgrade, this limit the toroidal wave number n to values below 20. The mode structure will also be limited to this range of toroidal modes.

Cyclotron damping

We take now the term $n = 1$ for thermal ions in the Equation 2.10. It corresponds to the dielectric tensor of the thermal ions developed in the Equation 2.60. Two main factors drive the cyclotron damping of a wave: the density of the plasma where the wave propagates and the proximity of cyclotron frequency (given by ζ_l). Therefore, for a

CAE to be damped, the cyclotron frequency layer of the background plasma has to intersect its localization area, at the edge. In this case, we have a low density, and, consequently, a low attenuation. The range of modes which are intersected is very narrow. Most of them are not affected by the cyclotron damping. Therefore, we neglect it as simplification for the further computations.

2.2.2 *Sources of fast ions*

We now focus on the characteristics of the fast ions that can excite the ion cyclotron emission. They have special features due to their high energy and their large Larmor radius. To deal with them, we will use a set of invariants of motions that simplify the equations of the ion/waves interaction in the cyclotron range of frequencies. This approach was developed by [24].

The banana orbit detailed in the section 1.3.4 is defined when its width verifies:

$$\delta_b = 2Ze\rho_L\sqrt{\frac{2R_0}{r}} \ll r$$

which is not valid for high energy particles, which do not stick to the magnetic surfaces but drift across them.

We also consider the three following constants of motions for a tokamak configuration:

- The kinetic energy: $E = \frac{m}{2}(v_\parallel^2 + v_c^2)$ which is an exact invariant,
- the magnetic moment: $\mu = \frac{m}{2}\frac{v_c^2}{B}$ which is an adiabatic invariant,
- and the toroidal angular moment: $J = mR\frac{B_\phi}{B}v_\parallel - \frac{e}{2\pi\phi_p}$ which is exact due to the invariance of the tokamak configuration through a toroidal rotation[9].

Following the methodology of [24], we use a slightly different set of invariants, more suited to ICRF interactions:

$$E = \frac{1}{2}mv^2 \qquad \text{Energy} \tag{2.72}$$

$$\Lambda = \frac{\mu B_c}{E} - 1 \qquad \text{Generalized pitch angle} \tag{2.73}$$

$$P_\phi = -\frac{J}{mvR_c} \qquad \text{Toroidal angular momentum} \tag{2.74}$$

We can express the position (x, z, ψ) of the particle in function of these invariants and obtain the orbit equation. From the definitions of Λ and P_ϕ, we get:

$$x = \frac{R_c}{2-\Lambda}[1 - \Lambda + (\psi - P_\phi)^2] \tag{2.75}$$

and the flux ϕ is given in function of $r = \sqrt{x^2 + z^2}$ by the equilibrium reconstruction.

$$\psi = F(x^2 + z^2) \tag{2.76}$$

The orbit of the particle is thus given by the intersection of the surfaces represented by equations 2.75 and 2.76 as shown on Figure 2.22.

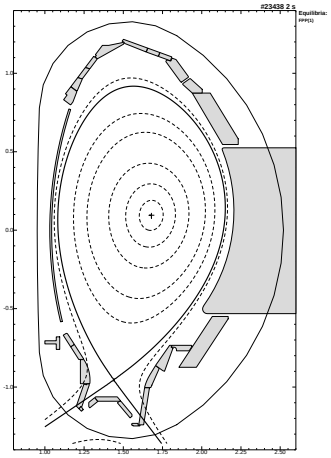

Figure 2.20: Representation of the poloidal fluxes on ASDEX Upgrade. They are reconstructed from the magnetic measurements with the EQE code. Shot 23438.

[9] The poloidal flux ϕ_P is taken equals to zero in the center and is represented on Figure 2.20.

where the indice c refers to the center of the plasma.

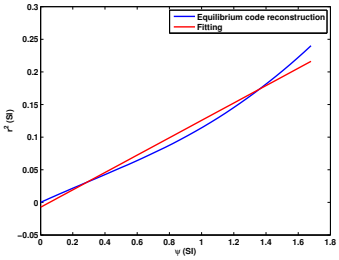

Figure 2.21: Relation between the square of the minor radius and the poloidal flux for a discharge with a current of $0.8MA$.

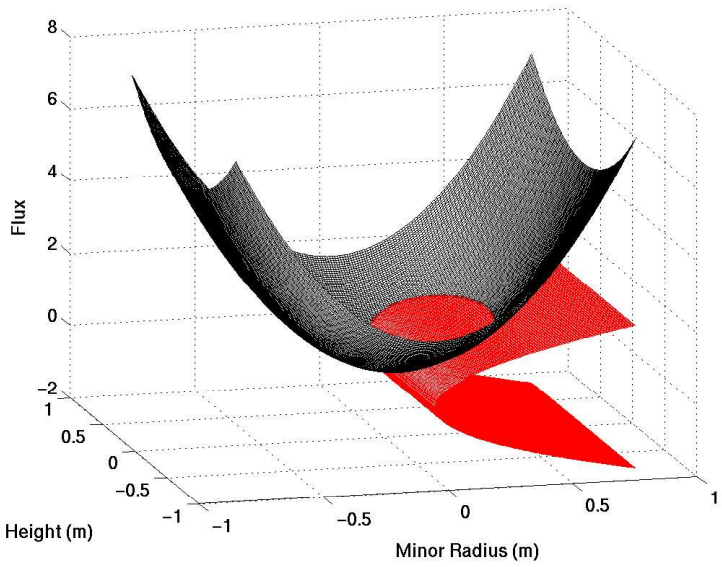

Figure 2.22: Determination of the orbit through the intersection of the surfaces given by equations 2.75 and 2.76.

A comparison of the analytical result with the full equation code GOURDON has been done. An example is given on Figure 2.23.

We can notice some differences far from the midplane, mainly due to the ellipticity of the real plasma. But the most important point for ICE is the agreement of the results at the outer edge on the midplane

As pointed out by [49], the different types of orbits that a fast ion follows can be classified by inspecting their intersection with the midplane:

$$\begin{aligned} z^2 = r^2 - x^2 = 0 \\ \Rightarrow r^2(\psi) - (\frac{R_c}{2-\Lambda})^2[1-\Lambda+(\psi-P_\phi)^2]^2 = 0 \end{aligned} \tag{2.77}$$

This important equation will give us a relation between the invariants for an orbit to reach a given radius, for instance, the radius where the ICE interaction takes place.

We distinguish four limiting orbits:

- those going through the magnetic axis: $\psi = 0 \Rightarrow \Lambda = P_\phi^2$. They will be important for us in the case of central ICE (A on Figure 2.24).
- the deeply trapped orbits: $v_\parallel = 0$ in the midplane (B on Figure 2.24).
- the pinch orbits which have three intersections with the midplane (C on Figure 2.24)
- the stagnation orbits where the vertical drift velocity compensates the poloidal velocity of the particle (D on Figure 2.24).

The details of the classification of the orbits will not be used in details for this study: we will not study the effect of the ICE on

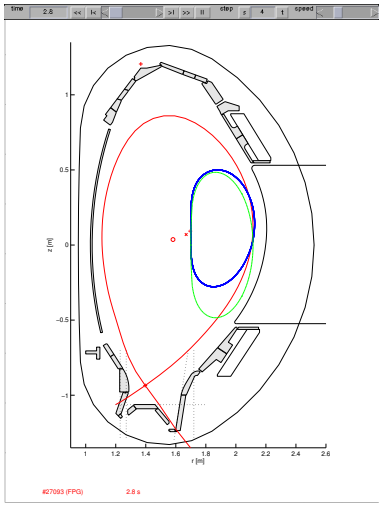

Figure 2.23: Comparison of the guiding center trajectories calculated with the analytical solution and with the full-orbit code GOURDON [28]. In blue, the result from GOURDON and in green the analytical solution.

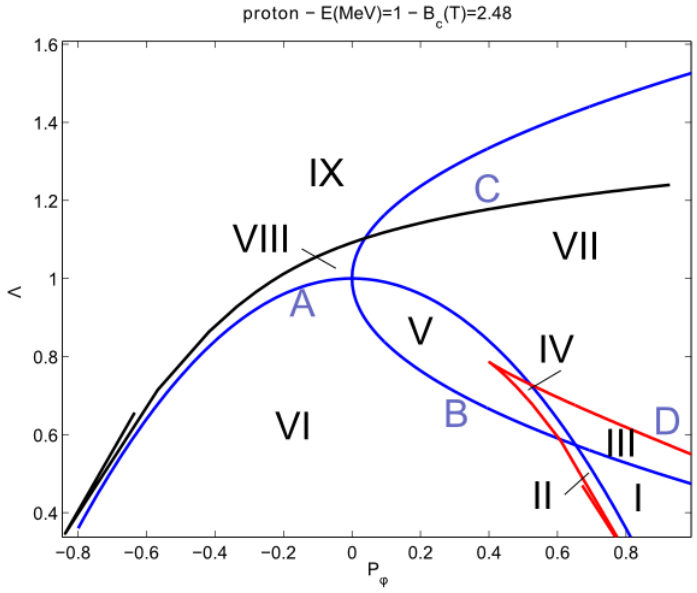

Figure 2.24: Classification of orbits in (λ, P_ϕ) space for a given energy. The meaning of the numbers is given in Table 2.1.

Table 2.1: Classification of the different types of orbits for fast ions, as displayed on Figure 2.24

Number	Type
I	co/counter passing orbits encircling the axis
II	counter passing orbit encircling the axis; co-passing orbit confined to high field side
III	Trapped orbit encircling the axis; copassing orbit encirciling the axis
IV	Trapped orbit encircling the axis; Copassing orbit confined to High field side
V	trapped orbit encircling the axis; counter passing orbit encircling the axis
VI	counter-passing orbit encircling the axis
VII	trapped orbit on Low Field Side
VIII	Counterpassing orbit not encircling the axis
IX	no orbit

.

the transition by the fast ions from one type of orbit to the other and the converse effect from this transition on the ICE. This is an important aspect for further studies because we do not know if this phenomenon has an impact on the emission.

We now have a suitable description of the adiabatic movement of the fast particles. Before going to their source and to their interaction with the cyclotron emission, a last point of interest is the slowing down process of these fast ions.

Slowing down of fast ions This is a summary of the method used by [51] to calculate the heating efficiency of neutral beams. With the assumption that $v_i \ll v_\alpha \ll v_e$ (we keep α as subscript for fast ions even if they are not alpha particles), the theory of collision states that the energy varies following the law:

$$\frac{dE}{dt} = -\alpha/E^{1/2} - \beta E \tag{2.78}$$

where α correspond to the collisions with background ions and β with the background electrons.

We define the critical energy $E_{cr} = (\alpha/\beta)^{2/3}$, which is the energy at which the energy loss rate is equally distributed between ions and electrons. Using the explicit values for α and β, we can express E_{cr}

as:

$$E_{cr} = 14.8kT_e[A^{3/2}/n_e \sum_j (n_j Z_j^2 / A_j)]^{2/3} \quad (2.79)$$

where A is the atomic mass of the fast ions, A_j of the background ions.

Above the critical energy, the fast ions transfer energy to electrons. Below the critical energy, the fast ions transfer energy to the ions.

An analytical formula can be given for the slowing down time:

$$\tau_{sd} = \int_0^{E_0} \frac{dE}{dE/dt} = \frac{t_s}{3} \cdot ln[1 + (\frac{E_0}{E_{cr}})^{3/2}] \quad (2.80)$$

where we have defined the *Spitzer slowing down time*:

where Λ is a constant between 16-20.

$$t_s = 6.27 \cdot 10^8 \frac{T_e^{3/2}}{n_e ln\Lambda} \cdot \frac{A}{Z^2} \quad (2.81)$$

Sources of fast particles

There are three main sources which are interesting for this study: the fast ions coming from the neutral beam injection: with an energy of several tens of keV, they are suprathermal but not super-alfvénic; the fast ions coming from the primary fusion reactions: protons, tritons and He-3. And the fast ions created by ICRF heating.

a) Fast ions from the Neutral Beam Injection

As schematically represented on Figure 3.2, fast neutrals are produced by charge exchange on positive ions (for ASDEX Upgrade) and injected into the plasma. They are transformed there in confined fast ions through ionization.

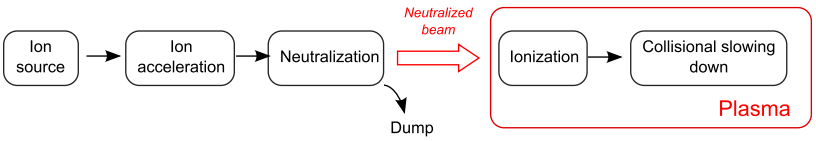

Figure 2.25: Plasma heating through Neutral Beam Injection - Sketch of the sequence of neutrals production and their ionization in the plasma.

Three mechanisms are at stake: charge exchange, ionization by ions, ionization by electrons. The two first are dominant in a tokamak. The mean free path of the neutrals is defined by:

$$\lambda = \frac{1}{n_e \sigma_\epsilon} \quad (2.82)$$

where we have defined the effective cross-section:

$$\sigma_\epsilon = \sigma_{CX}(v_{beam}) + \sigma_{ii}(v_{beam}) \quad (2.83)$$

For the neutrals to reach the center, the condition $\lambda \approx a$ has to be fulfilled (where a is the minor radius). The fast ions created heat the plasma by slowing down mostly on electrons since $E_{beam} \gg E_{critical}$. The trajectories of the beam fast ions are represented on Figure 2.26 in (Λ, P_ϕ) space for the two NBI boxes of ASDEX Upgrade (cf. section 3.1.2).

The distribution function of these fast ions is thus the result of a competition between the ionization, the slowing down and the losses. There can be two possibilities to have an inversion of the distribution function:

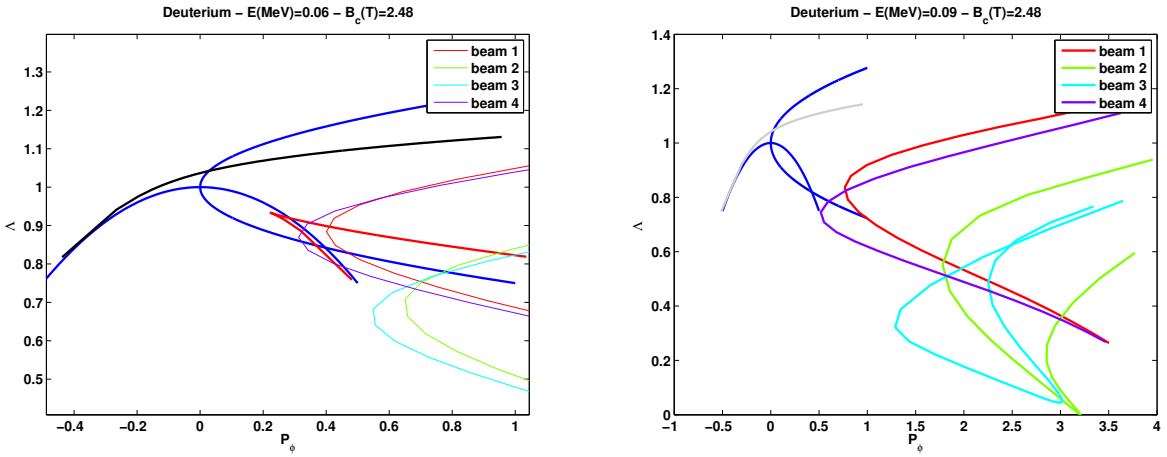

Figure 2.26: Orbits of the different beam fast ions in (Λ, P_ϕ) space. Left: box 1 of ASDEX Upgrade; Right: box 2 of ASDEX Upgrade

- at the beginning of the neutral injection, in the center, before the fast ions have time to slow down
- in steady state, near the edge: the ionization rate is low but the long slowing down time due to the low density and the high rate of losses can maintain a tail of high energy ions.

b) Fusion products

The main reaction on ASDEX Upgrade is Deuterium-Deuterium. The reactions can occur in three way during neutral beam injection:

- thermal: thermal deuterons at high temperature react
- beam-thermal: the reaction occurs between a fast ion from the neutral beam and a thermal ion from the background plasma. It is the dominant reaction on ASDEX Upgrade (see [52]).
- beam-beam: reaction between two fast ions from the neutral beam injection.

For the edge ICE, we need a description of the fusion products which are born at the center and that can reach the edge. Therefore we choose a simple model for the distribution function:

$$f \propto exp(-\frac{r^2}{\Delta r^2})\ exp(-\frac{(E_0 - E)^2}{\Delta E^2}) \tag{2.84}$$

where Δr is a characteristic length for the area near the center where fusion reactions are the most intense and ΔE represents the width of the energy tail. E_0 is birth energy of the fusion product; it depends on the species.

The distribution function is general but we are more interested on the part of the fast ions which can reach the edge of the plasma at $\psi = \psi_r$ to excite the ion cyclotron emission. For these ions, we have, following Equation 2.77, a relation between Λ, E and P_ϕ:

$$\Lambda = f(E, P_\phi)$$

which turns to be, for a given energy, a parabola represented in blue on Figure 2.27.

The intersection A between the black and blue curves on this figure gives the set of (Λ, P_ϕ) values of particles born in the center with a given energy and reaching the plasma edge. The value of Λ is thus

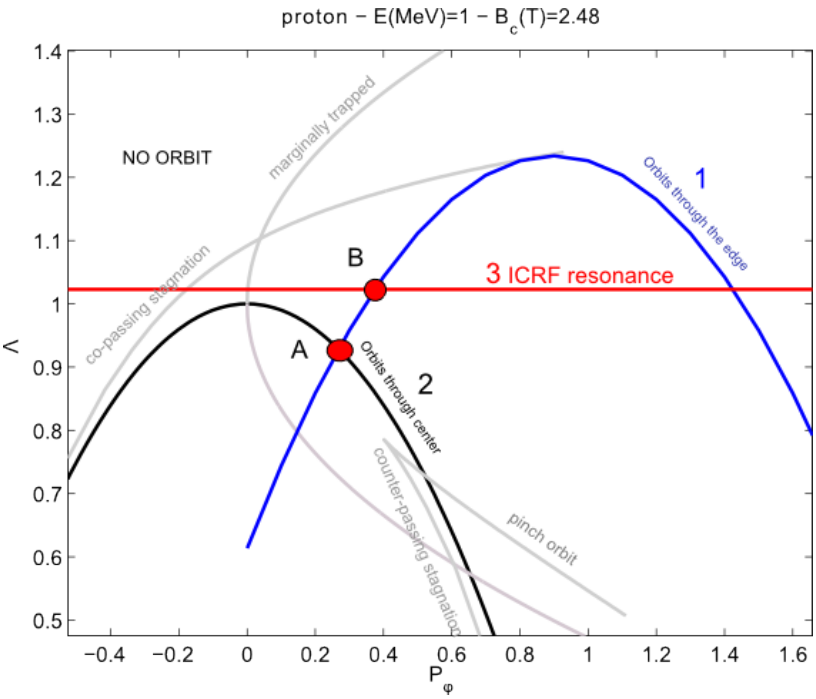

Figure 2.27: Blue: characteristic curves for particles reaching the plasma edge at $\psi = 0.9$. Black: characteristic curve of particles running through $\phi = 0$. Red: position of the ICRF resonant layer $\gamma_r = 0.04$.

determined by the value of P_ϕ and the distribution function 2.84 can be expressed only in terms of E and P_ϕ. The result is represented on Figure 2.28. We note that the contour is very narrow in configuration space (if we compare with the distribution function of ICRF-accelerated fast ions on Figure 2.32). This will be important for the comparison of the spectra of mICE and FP-ICE in section 2.2.3.

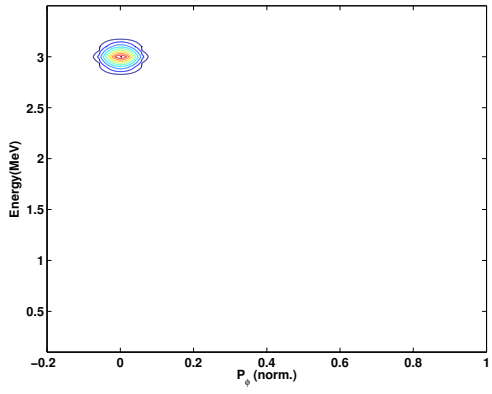

Figure 2.28: Contour plot of the normalized distribution function of protons reaching the plasma edge with $\Delta E = 0.5$ and $\Delta r = 0.05$.

c) ICRF accelerated fast ions

The ICRF heating is based on the launch by an external antenna of a compressional Alfvén wave into the plasma. As depicted on Figure 2.29, the system is made of a generator that creates a RF wave which propagates into a transmission line to the antenna where it radiates. The wave is evanescent in the vacuum layer between the wall and the plasma. To overcome this layer and make the wave tunnel to the plasma, high voltages have to be produced on the antenna

straps. This is achieved with a matching system, which adapts the impedance of the antenna coupled to the plasma to the impedance of the generator.

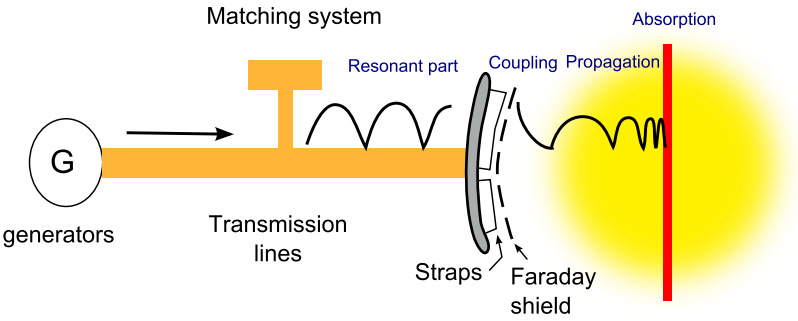

Figure 2.29: Principle of ICRF heating.

The evaluation of the ICRF heating is splitted in three part:

- the calculation of the coupling between the antenna and the plasma: the wave is evanescent in the vacuum of the scrape-off layer and has to tunnel until it reaches a sufficient density to propagate (the cut-off layer). The ICRF antenna can launch a wave with a small (continuous) parallel wave vector, which results in a mostly radial propagation towards the center of the plasma.
- the propagation of the wave inside the plasma: it is calculated with the cold plasma approximation with ray-tracing. The wave is in this case solution of the Equation 2.55 with a dominant k_r (whereas CAEs have a dominant k_p). It is solved considering a constant ω which is the generator frequency and the cyclotron frequency ω_{ci} depends on the radial position through the magnetic field. When $\omega = \omega_{ci}$, the cold plasma approximation breaks down: we have a resonance.
- near the resonance, it is required to use the hot plasma dielectric tensor 2.60 for the dispersion relation and to calculate the absorption of power by the ions.

The methodology is quite similar for both ICRF heating and ICE excitation but in reverse. We have to be careful that in one case, the frequency and the wave vector of the wave are fixed while, for ICE, it is free: we have more degree of freedom.

In a pure Deuterium plasma, the component of the wave electrical field rotating in the same direction as the ions disappears at the location where the cyclotron frequency of the deuterons is equal to the wave frequency, preventing any resonant interaction. Two main schemes have been developed and are regularly used to overcome this issue:

- heating at the second harmonic of the cyclotron frequency in the center,
- injecting a small amount of Hydrogen in the plasma: they do not change the characteristics of the wave which are defined by the

background deuterium but they can enter in resonance when their cyclotron gyration has the same frequency as the wave. A tail of fast ions is also created with energies beyond 1 MeV (cf. [46]).

This second scheme is the most used on ASDEX Upgrade and we will focus on it for the rest of the report.

The Hamiltonian formalism used for this study of ICE was initially developed for ICRF. [1] and [23] have shown that ICRF heating corresponds to a diffusion of the fast ions in phase space, given by the operator 2.45.

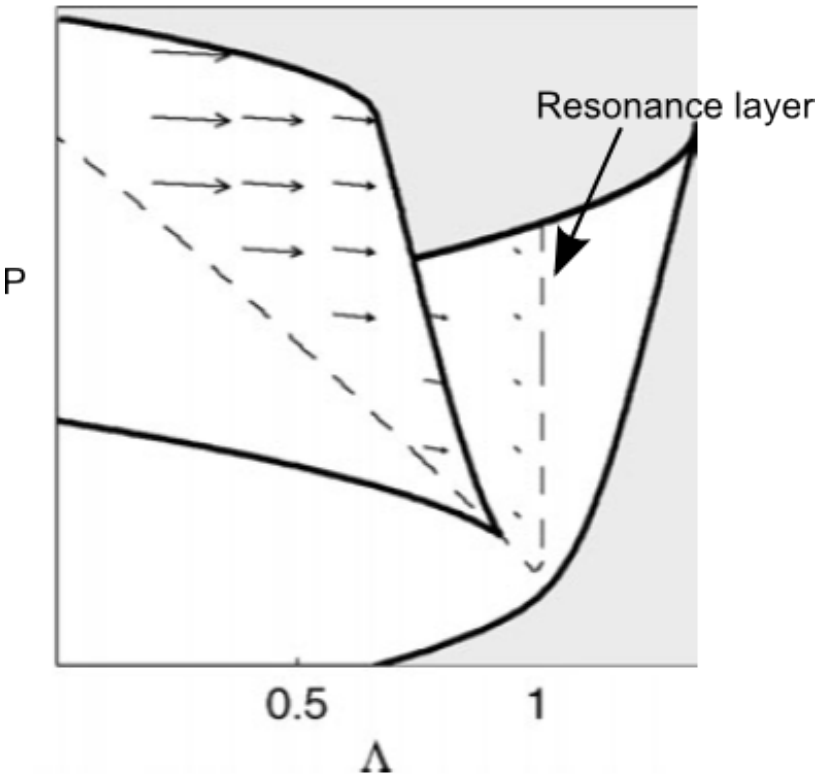

Figure 2.30: Effect of ICRF diffusion in (Λ, P_ϕ) space, represented by arrows. The bouncing points of the fast ions are diffused towards the cyclotron resonance layer [35].

The effect of this diffusion operator is to "move" the bounce points of the fast ions orbits towards the ion cyclotron resonance layer as represented on Figure 2.31.

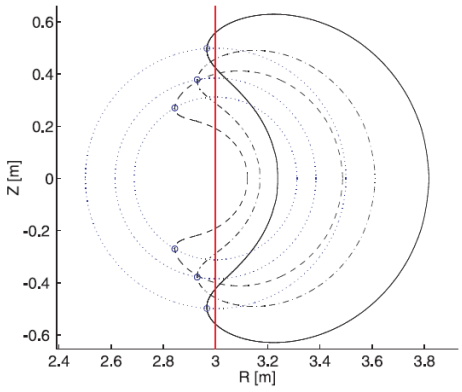

Figure 2.31: Diffusion in physical space of a fast ions heat by ICRF [35].

Therefore, for mICE, we need a population of fast ions that both can reach the edge and that are "born" on this resonant layer. This is represented by intersection B between the red line and the blue curve on Figure 2.24. It is indeed these ions which have the higher energies and that are the most certain to excite the instability. We model the distribution function in the form $F \propto exp(-\frac{(\Lambda-\Lambda_r)^2}{\Delta\Lambda^2})\ exp(-\frac{(E-E_{cen})^2}{\Delta E^2})$ where Λ is actually a function of P_ϕ for a given energy. The contour plot is represented for different parameters on Figure 2.32. It is more elongated than for the fusion products because of the different relation between Λ and P_ϕ at the "birth" location (ICRF-accelerated ions are not born on the resonance layer, but just diffuse to it).

We have obtained a simple parametrization for fusion products

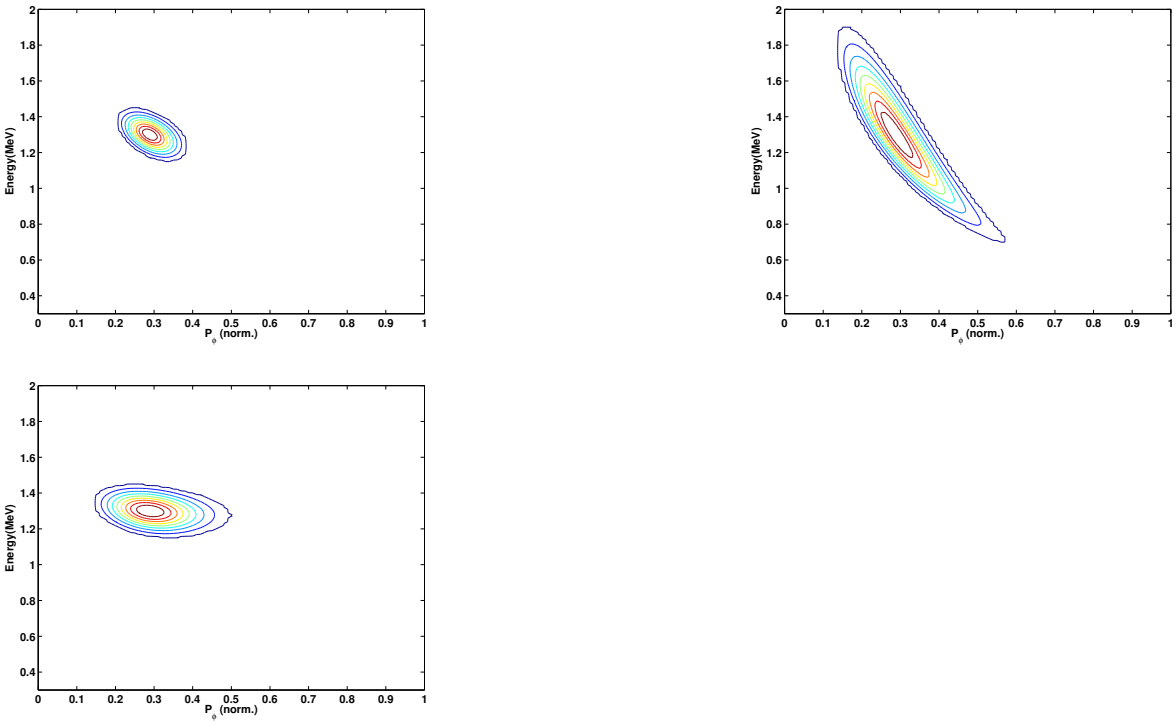

Figure 2.32: Contour plots of the normalized distribution function for ICRF accelerated Hydrogen ions reaching the edge. Left: $\Delta E = 1.10^5$, $\Delta\Lambda = 0.04$. Middle: $\Delta E = 5.10^5$, $\Delta\Lambda = 0.04$. Right: $\Delta E = 5.10^5$, $\Delta\Lambda = 0.08$

and fast ions which will be useful for the calculation of the ICE growth rate, which is the object of the final section.

2.2.3 *Ion Cyclotron Emission*

We have presented all tools and results which are required to analyze the ion cyclotron emission. In this part, we will assemble all these elements together to get the big picture of the instability. Our main purpose is to establish a relation between the distribution function of the fast ions and the spectrum of the emission. We will split our analysis in three parts:

- the ICE due to fusion products and ICRF-accelerated ions where we will be able to have a detailed theory of the interaction based on previous works,
- the ICE due to the beam: we will sketch here only some hypotheses. A more detailed analysis will come in the discussion in section 5.2 because we need the results of our experiments to establish a more robust theory,
- the central ICE: as in the previous case, we will only draw the main lines of what the theory can be, postponing a refined analysis to the discussion.

A/ FP-ICE and m-ICE

This emission takes place at the edge and is due to fast ions coming from the center (either fusion products or ICRF-accelerated hydrogen) exciting magneto-acoustic modes. Using the dielectric ten-

sor 2.33 written in (E, Λ, P_ϕ) coordinates:

$$\epsilon^{\alpha} = -\frac{\omega_{p\alpha}^2}{\omega^2} \sum_N \int \frac{\mathbf{V_N^* V_N}}{N\omega_c + \mathbf{k}\cdot\mathbf{v_g} - (\omega + j\eta)} \frac{\Pi}{\tau_b} L_N \cdot F \, dE \, d\Lambda \, dP_\phi \quad (2.85)$$

where $\mathbf{V_N}$ is defined by Equation 2.10:

$$\mathbf{V_N}(\mathbf{v}, \mathbf{k}) = \begin{pmatrix} \frac{N\omega_c}{k_\perp} J_N(\frac{k_\perp v_c}{\omega_c}) \\ j\frac{v_c}{k_\perp} J'_N(\frac{k_\perp v_c}{\omega_c}) \\ v_\parallel J_N(\frac{k_\perp v_c}{\omega_c}) \end{pmatrix}$$

and L_N is the derivative operator along the characteristics line in the configuration space (E, Λ, P_ϕ):

$$L_N = \omega \frac{\partial}{\partial E} + \frac{N\omega_c - \Lambda\omega}{E} \frac{\partial}{\partial \Lambda} \quad (2.86)$$

Π/τ_b represents the fraction of the trajectory duration where the population of fast ion is in resonance with the wave. To simplify the computations and as explained in Section 2.1.3, we will take this ratio equal to 1 (straight field approximation).

There are three intertwined components in the Equation 2.85:

- The wave, through its frequency and its location. This is given by the mode structure of the compressional Alfvén eigenmodes,
- the distribution function of the fast ions which weighs in through its derivative,
- and the local resonance condition $\omega = N\omega_c + \mathbf{k}\cdot\mathbf{v_g}$.

The dielectric tensor contains the information required to calculate the growth rate which correspond to the short term evolution of the instability. Our first step will be to calculate it. In a second step, we will use the energy balance to evaluate the long term evolution.

Growth rate of the edge ICE

We can calculate the growth rate 2.42 of the emission in the case of compressional waves and with the assumption of a weak instability $|\gamma/\omega| \ll 1$:

$$\frac{\gamma}{\omega_0} = -\frac{\omega_0^2}{2\omega_{pi}^2} Im\epsilon_{11}^{\alpha}(\omega_0) \quad (2.87)$$

We have on the three variables two constraints:

- the fast ions must reach the position where the CAEs are localized, at the edge. Given the respective sizes of the Larmor radius and of the eigenmodes, this constraint is strong. We will suppose in this study, that the position of the mode is given by a single radius and not by a range of radii. This strong constraint is justified by the fact that the theory supposes that the whole gyration takes place inside the mode location; if we leave too much room for the variation of the radius of intersection between orbit and mode, we break this assumption. As a result, for a given energy E, Λ and P_ϕ are constrained by the Equation 2.76 with $\Psi = \Psi_{res}$ (it is characterized by the blue parabola on Figure 2.27 and, in Equation 2.85, Λ will be considered a function of P_ϕ, which eliminates one integral.

- the second constraint is the resonance condition $\omega = \omega_{c\alpha} + \mathbf{k} \cdot \mathbf{v_g}$. This relation creates a strong dependence between P_ϕ of the fast ions and ω of the modes. For each mode (m, n), we have to calculate the intersection between the line ω and the curve $\omega_{c\alpha} + \mathbf{k} \cdot \mathbf{v_g}$ which depends on (m, n) through $\mathbf{k}$ and on P_ϕ. The principle is represented on Figure 2.33. The integration in P_ϕ of the term $1/\delta(\Omega) = 1/\delta(N\omega_c + \mathbf{k} \cdot \mathbf{v_g} - \omega)$ reveals the term $d\Omega/dP_\phi$ which, as mentioned by [25], enhances interactions with low $k_\parallel$ (cf. Figure 2.34).

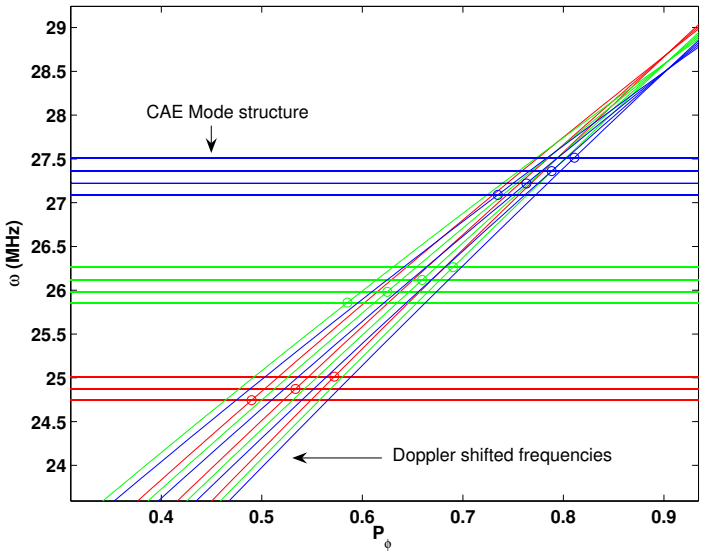

Figure 2.33: Graphical representation of the resonance condition in (P_ϕ, ω) axes for some CAE eigenmodes. Each color represents a mode with a different poloidal number. The constant lines correspond to the mode structure the ω part of the resonant condition. The curves represent the Doppler shifted cyclotron frequency at the mode location.

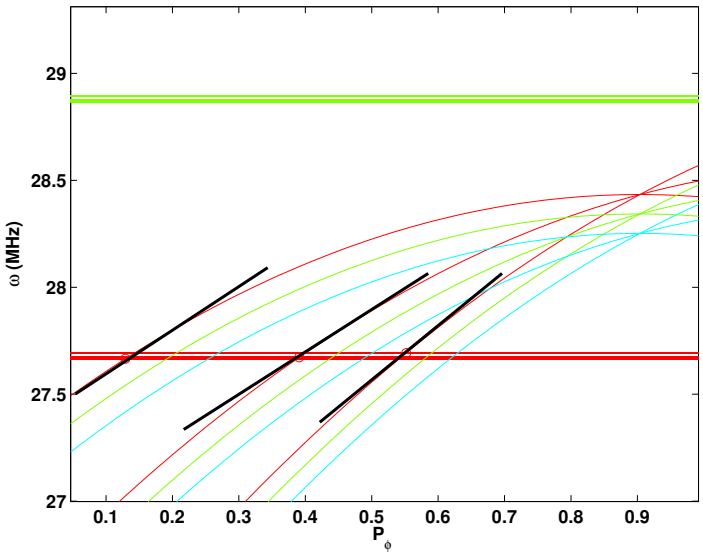

Figure 2.34: Zoom on the resonance condition for one poloidal mode with different toroidal numbers. The circles represent the values of P_ϕ and ω for which we have resonance. We have highlighted the slope at these resonances that modifies the intensity of the interaction.

After having integrated in P_ϕ, respecting the resonance condition, we can integrate in E, along the characteristic paths on the given distribution function, as represented on Figure 2.35.

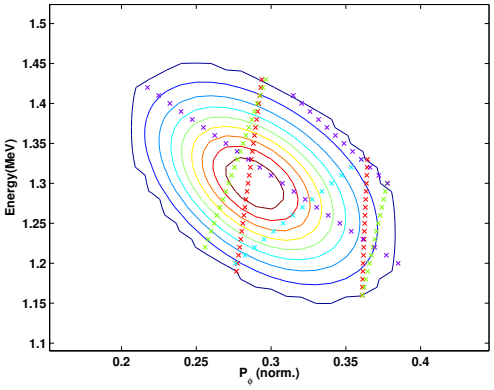

Figure 2.35: Paths of integration of $L_N F$ for different modes superimposed on the contour of the distribution function.

We are now able to calculate the growth rate for each mode of the instability from a simple model of distribution function based on a limited number of parameters. We can thus get a "spectrum" of growth rates in function of the frequency. We have two families of parameters:

- The parameters of the background plasma that determine the structure of the eigenmode (cf. 2.2.1): the magnetic field B and the density profile modeled with n_c (density in the center) and the doublet (σ_1, σ_2) for its shape.
- The characteristics of the fast ion population (Cf. 2.2.2): its species (proton, Helium-3, hydrogen) with the associated birth energy, its concentration n_α/n_i at the edge, and its distribution function parametrized by $(\Delta P_\phi, \Delta E)$ for fusion products and by $(E_0, \Delta E, \Delta\Lambda)$ for minority species accelerated by ICRF (and the position of the ICRF resonance layer).

Our purpose is first to describe the frequency structure of the growth rate and, second, to do a sweep on the parameters of the distribution function and of the background plasma to check how each of them influences the spectrum.

To obtain a reference case, we have calculated the growth rates for two different ion populations in the same type of plasma ($B = 2.6\ T$, $n_{i0} = 4.10^{19}\ m^{-3}$) with the same concentration ($n_\alpha/n_i = 10^{-6}$): a population of fusion protons ($E_0 = 3\ MeV, \Delta E = 100\ keV, \Delta P_\phi = 0.01$) and a population of hydrogen ions accelerated by ICRF ($E_0 = 1\ MeV, \Delta E = 500\ keV, \Delta\Lambda = 0.1$). The result is presented on Figure 2.36.

The frequency sweep goes above the third cyclotron harmonic of both species of fast ions. For the fusion protons, we observe three frequencies: the main one at the cyclotron frequency of proton slightly shifted due to Doppler effect. Another one is present at a lower frequency due to a larger Doppler shift; no damping effect is taken into

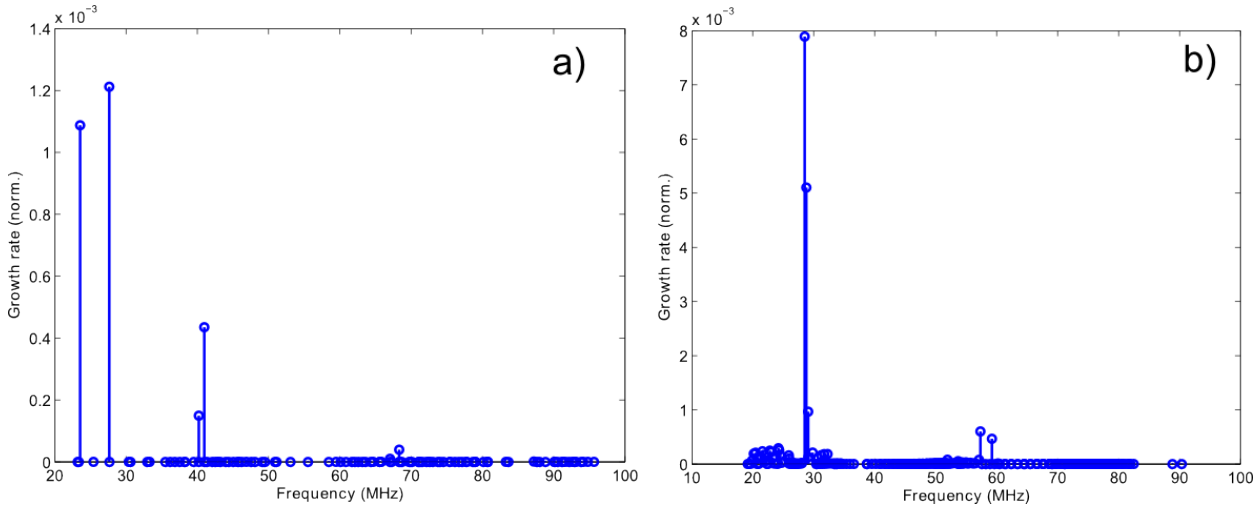

Figure 2.36: Spectrum of growth rates for a) fusion protons ($E_0 = 3\ MeV, \Delta E = 100\ keV, \Delta P_\phi = 0.01$) b) ICRF accelerated hydrogen ions ($E_0 = 1\ MeV, \Delta E = 500\ keV, \Delta\Lambda = 0.1$). The background plasma is made of Deuterium ($B = 2.6\ T$, $n_{i0} = 4.10^{19}\ m^{-3}$).

account, but it is probable that this latter frequency will be strongly attenuated by cyclotron resonance on the background ions. In addition, we said previously that the CAE model was valid above the second cyclotron harmonic of Deuterium; the peaks far below can consequently be considered unreliable. The peak with the lowest intensity is found near the third harmonic of Deuterium above 40 MHz. For ICRF hydrogen ions, there is a triplet of peaks at the hydrogen cyclotron frequency near 30 MHz and another doublet of peaks with a lower intensity near the second harmonic. With these preliminary observations, we can already draw an important conclusion: without taking into account any damping effects, the spectra obtained feature peaks which are located in very limited area of the frequency range; the shape of the distribution function and the resonance condition combine so that only a limited number of frequencies is excited.

If we compare both results, we first see that the mICE has a higher growth rate than the FP-ICE for the main cyclotron frequency. The concentration being the same, this is due to the extension of the fast ion population in configuration space: ICRF heating creates a larger tail in energy than the fusion reactions. The second observation concerns the number of frequencies excited near the cyclotron harmonics: one for FP-ICE and three for mICE. Here again, it is due to the shape of the distribution functions as displayed on Figures 2.28 and 2.32. There is more "room" for several paths of integration on the ICRF distribution function; in other words, the population of ICRF-accelerated hydrogen ion can be in resonance with more modes, offering a richer mode structure.

We turn now on a more specific study of the spectrum due to FP-ICE. The main question in this case is to know if we can excite more frequencies by varying the parameters. This is actually possible when we change the density profile and its slope at the edge (by varying the parameter σ_2 in the Equation 2.69). Two different cases are presented on Figure 2.37. The position of the frequencies in the spectrum remain the same but with a large variation in their ampli-

tude. At 30 MHz, there is only one frequency, but it is possible to get a triplet near $3\omega_{ci}(D)$. What is important to note is the extreme sensitivity of the result to the variation of the density profile: the amplitude of the frequency can change very quickly for a slight variation of the slope, which means that the spectrum is very dependent on the mode structure (which is determined by the density profile).

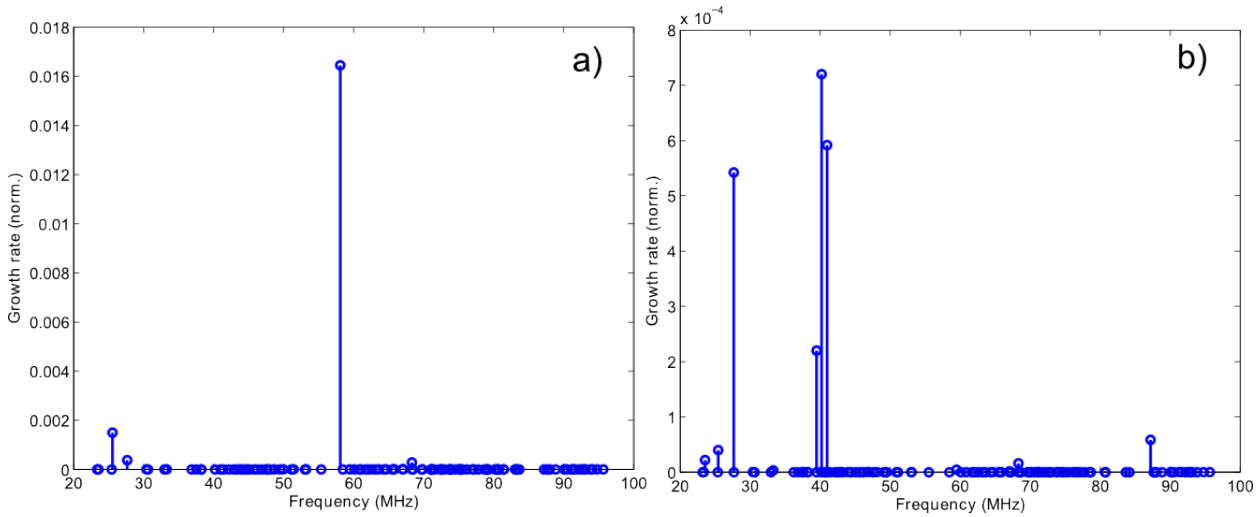

Figure 2.37: Spectrum of growth rates for fusion protons with the same conditions as for Figure 2.36 except for the density profile: a) $\sigma_2 = 0.3$ and b) $\sigma_2 = 0.7$ where σ_2 is defined in the Equation 2.69. The case in Figure 2.36 was calculated with $\sigma_2 = 0.5$.

It is also interesting to see how changes brought to the distribution function can affect the spectrum. The parametric study in function of ΔP_ϕ is presented on Figure 2.38. We focus on the frequencies near 30 MHz. The growth rate evolves in two phases with growing ΔP_ϕ: a rather steep increase followed by a smooth decrease. This is due to the competing effect in the integral of the dielectric tensor of Equation 2.85 between, on one side, the extension of the distribution function in configuration space and, on the other side, its gradient; for small ΔP_ϕ, the integral increases but, above a given threshold in ΔP_ϕ, the distribution function flattens more and the gradient decreases, diminishing the value of the integral.

The case of mICE with its rich spectrum will bring more details to the analysis of the growth rate. We study first the evolution of the spectrum near the first cyclotron harmonic of Hydrogen with the density. The result is presented on Figure 2.39. The frequencies follow the evolution of the Alfvén velocity, conversely proportional to the square root of the density. We also notice that the upper and lower limits of the excited frequencies evolve as well towards the lower values.

The evolution of the characteristics of the distribution function also affects the growth rate. We did a parameter study both for the extension ΔE in energy of the tail of fast ions and for its average value E_0. Both results are displayed on Figure 2.40. The change due to ΔE is similar to the effect produced by ΔJ on the proton population on Figure 2.38. The variation induced by E_0 has more impact on the structure of the spectrum: when E_0 varies, new frequencies

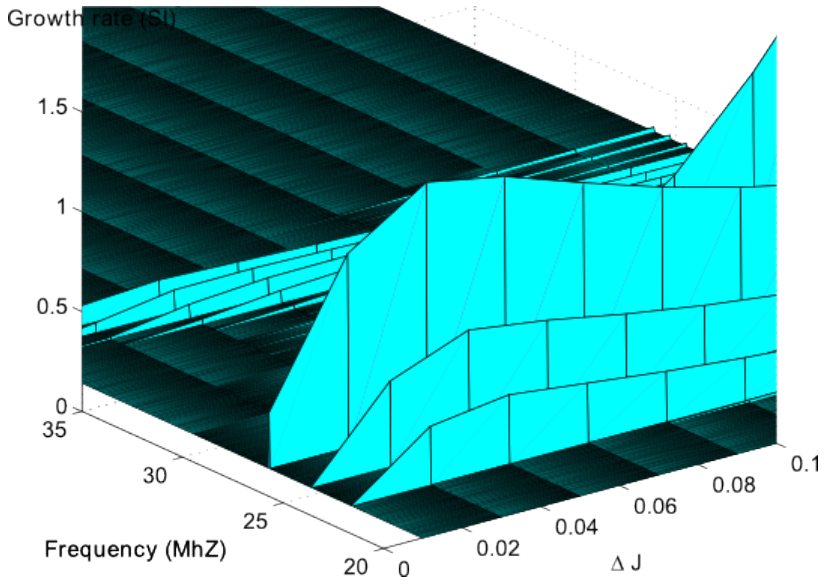

Figure 2.38: Variation of the spectrum with respect to ΔP_ϕ. The other parameters are the same as for the results of Figure 2.37 b).

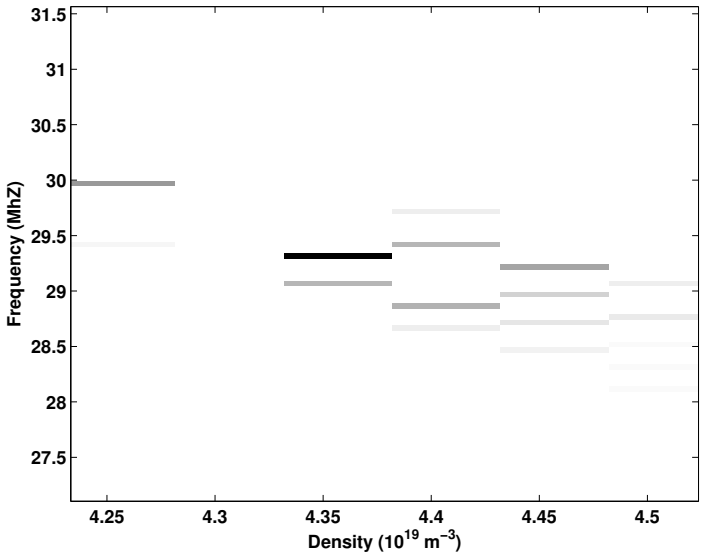

Figure 2.39: Evolution of the growth rate spectrum with the density at the center (which is related to the density at the center through the profile given by Equation 2.69) for a population of ICRF-accelerated hydrogen ions. The frequencies decrease when the density grows up, which is a characteristic behavior of Alfvén waves.

grow up and others disappear. The consequence is important: the energetic "size" of the tail acts on the intensity of the growth but it is the average energy of this tail which selects which frequencies are present.

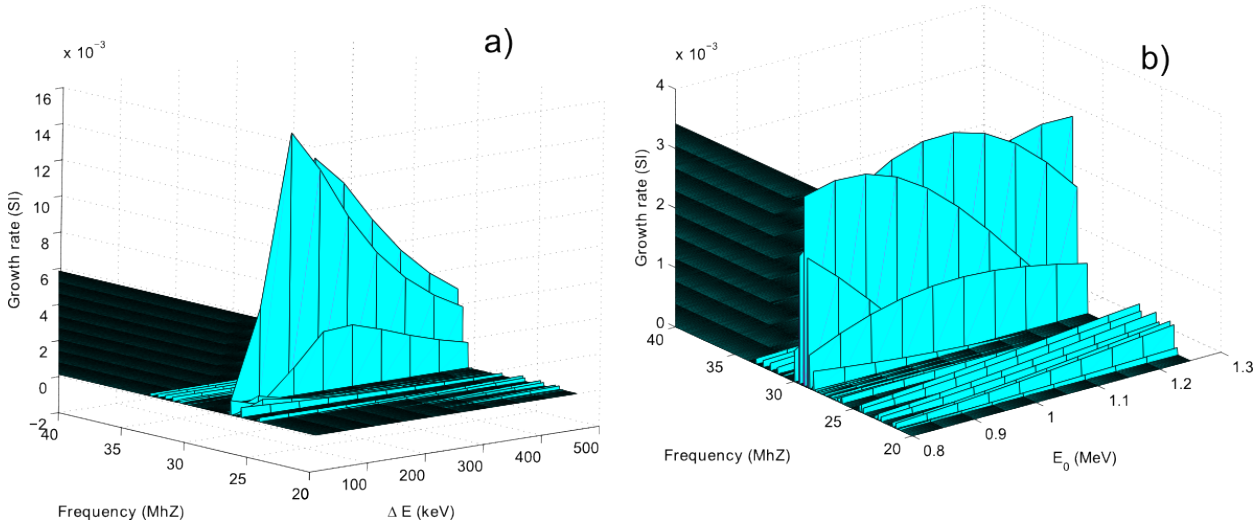

Figure 2.40: Evolution of the growth rate spectrum in function of a) ΔE the widening in energy of the tail of fast ions and b) E_0 the average energy of the tail of fast ions for mICE.

Quasi-linear evolution

The long term evolution of the wave and of the fast ions population is given by Equations 2.43 and 2.48:

$$\frac{dW}{dt} = 2(\gamma - \gamma_{damping})W - L - C_{nl}$$
$$\frac{\partial F}{\partial t} = S + C(F) + D_{QL}(F) + D_{ICRF}(F)$$

We will do several assumptions to make them more tractable for a comparison with the experimental results. First, we consider only one mode of CAE (ω, m, n) excited by a population with a density n_{res} of fast ions. In the energy balance, we neglect the losses and non-linear effects, keeping only the term of emission and of damping. The growth rate γ is proportional to the density of the fast ions, so that the equation can be rewritten:

$$\frac{dW}{dt} = A\ n_{res}\ W - B\ W \tag{2.88}$$

The diffusion equation is more delicate to handle: it describes how the curve 1 on Figure 2.41 is distorted along the lines of diffusion under the action of the ICE resonance. To get the time evolution of the population without too much computation, we simplify the model by assuming that the distribution of ions in resonance with the CAE mode (ω, m, n) is point-like of the form $\delta(E - E_0)\delta(J - J_0)\delta(P_\phi - P_{\phi 0})$ where δ is the Dirac function. The density of this population is n_{res}. Now, we have to separately consider the cases of fusion products

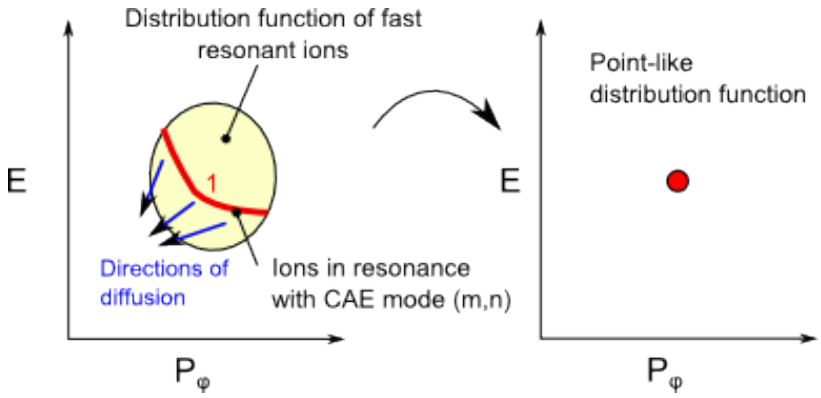

Figure 2.41: Simplification of the distribution function in a point-like function.

and minority species accelerated by ICRH. In addition, we will neglect the Coulomb collisions (represented by the term $C(F)$).

For the fusion products, we have a source term that corresponds to a fraction of the rate of fusion reactions, the fraction of ions that have $P_\phi = P_{\phi 0}$ and $\Lambda = \Lambda_0$. The quasi-linear diffusion term due to ICE is transformed by supposing that the resonant particles are escaping the resonance region through diffusion; the corresponding loss is obtained from the energy balance between the energy gained by the wave and the energy lost from the escaping ions:

$$\frac{dn_{res}E_{res}}{dt} = -An_{res}W \rightarrow \frac{dn_{res}}{dt} = -\frac{A}{E}n_{res}W \tag{2.89}$$

For the ions accelerated by minority heating, the source term is more difficult to evaluate because heating occurs through a diffusion process. We separate the heating term in two parts: first, a fraction of the power is transfered to the non-resonating ions to create new resonant ions:

$$\frac{dn_{res}}{dt} = xP \tag{2.90}$$

where P is the heating power and x is a fraction corresponding to the concentration of fast ions at the edge (this is rough, we admit it).

This term is independent of W and n_{res} and is only due to the heating of the background ions. But we have to add another term due to the "re-heating" by ICRF of the resonant ions which are diffused through ICE interactions. The amount of diffused resonant ions is, as in the fusion products case: $dn_{res}/dt = A/E\ n_{res}W$. A fraction y of it is reheated and "pushed" again in the resonance, overall decreasing the losses. Thus, the term due to ICRF heating is:

$$\frac{dn_{res}}{dt} = \frac{xP}{E} - \frac{A}{E}(1 - \frac{yP}{E})n_{res}W \tag{2.91}$$

To sum up, we have a system of two equations of the energy W and the resonant ions density n_{res} of the form:

$$\frac{dW}{dt} = An_{res}W - BW \tag{2.92}$$

$$\frac{dn_{res}}{dt} = C - DWn_{res} \tag{2.93}$$

These Lotka-Volterra equations constitute a "predator-prey" model and can be solved numerically, what we did for the cases of mICE

and FP-ICE, as shown on Figure 2.42. For this computation, we have chosen a value of the ICE growth rate $\gamma/\omega = 10^{-3}$ for an initial concentration of fast ions of $10^{-5}\ m^{-3}$. The damping coefficient has a value $\gamma_D/\omega = 10^{-4}$. For ICRF, we consider a power of 4 MW, for fusion products, the total production rate is $10^{15}\ s^{-1}$.

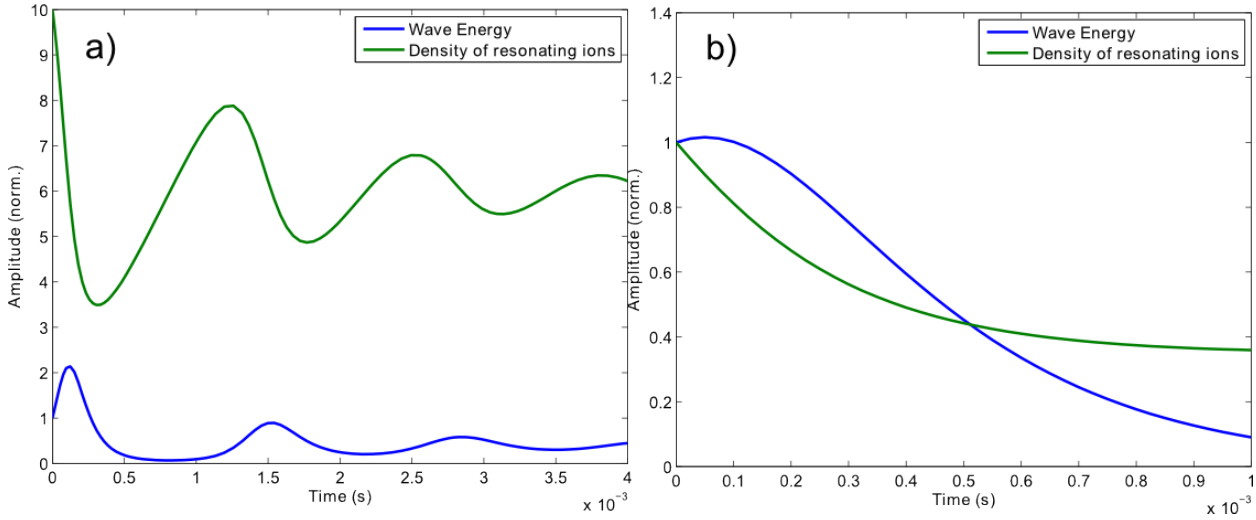

Figure 2.42: Numerical solution of the system 2.92 for a) ICRF accelerated hydrogen ions and b) fusion protons.

With these values taken as representative as possible of ASDEX Upgrade parameters, we obtain two different cases for mICE and FP-ICE. The former presents oscillations of both the distribution function and the wave energy with a small attenuation: the system is stable and leads to a steady-state emission. For fusion protons, the slightest emission sweeps out the fast ion population and the system collapses in few milliseconds. It is important to notice that the system is very sensitive to the parameters and the stability can change abruptly. For instance, if we consider the increase of the production of fusion protons, the emission increases with an overshoot followed by a plateau as seen on Figure 2.43 a). If we increase the reaction rate to the hypothetical value of $10^{18}\ s^{-1}$, the emission completely overcomes the damping rate and is exponential: it leaves the linear domain of validity and a mechanism of saturation has to be considered.

We now have a set of tools that predicts the growth rate and the quasi-linear evolution of the ICE emission and of the population of fast ions. We consider the two aspects separately but, in the future, a code should integrate both together to predict the spectrum that can be measured in a tokamak. The prediction is one aspect but it would also be interesting to proceed with the reversed operation: from a measured spectrum, we could reconstitute the parameters of the population of fast ions at the origin of the emission.

Reconstruction of the distribution function

The theory proposed in this chapter makes possible this reverse operation because it clearly highlight the relation between the frequencies excited and the parameters (E, Λ, P_ϕ) of the exciting pop-

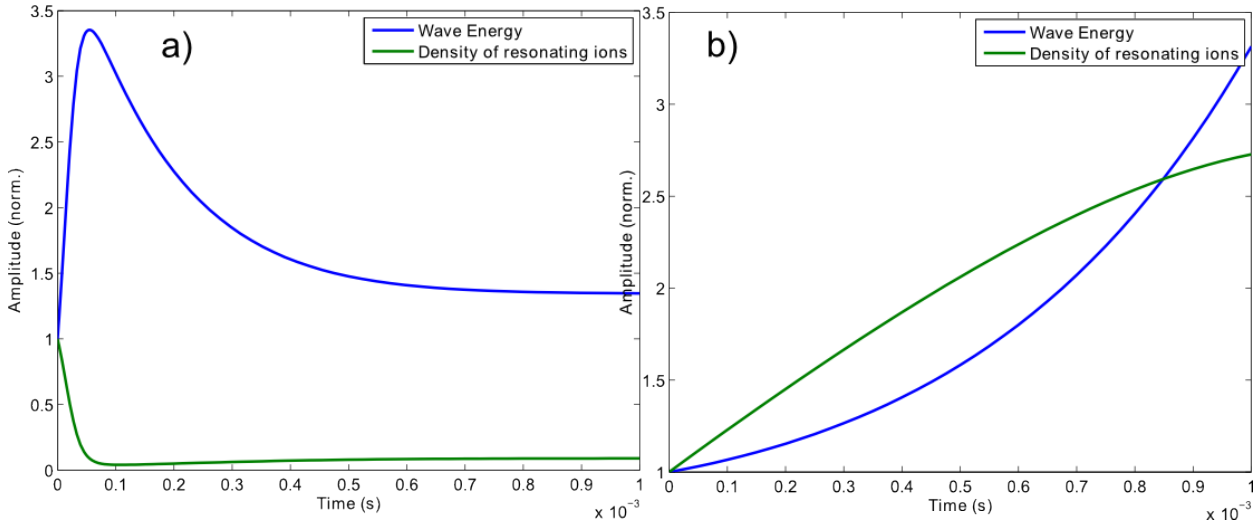

Figure 2.43: Numerical solutions of the system 2.92 for fusion protons with a fusion reaction rate of 10^{16} for a) and 10^{18} for b).

ulation. As said before, this was the reason for the choice of the Hamiltonian theory. In the ideal case, an array of probes toroidally and poloidally arranged should give us the frequency spectrum associated with the $k_{\|}$ and $k_{\perp}$ of each mode, so that we have a direct measurement of the mode structure. But we will see in the next section that we have for this study only two probes in positions that prevent any attempt at measuring the wave vector. In this case, we have to rely on the CAE models of the section 2.2.1 and to tune the parameters to get a frequency structure similar to what is observed[10]. Once the mode structure is established, we can sweep the parameters of the distribution function until the resulting theoretical spectrum matches the measured spectrum. In the present state of the codes, this is done by hand using parametric curves like those of Figures 2.38 or 2.40. We will see in the chapter 5 how it works on an example.

[10] In principle, if the models were perfect, they would fit the measurement without tuning. But we saw how sensitive they were to parametric sweeps.

B/ Beam-driven ICE

The exact mechanism of the beam-driven ICE has not yet been demonstrated: the main difficulty is to distinguish this emission from the FP-ICE which appear under similar conditions. The principal theory has been developed by Dendy ([18]) in homogeneous plasma and adapted by Fulop to the toroidal case ([26]). The idea is to imagine that the beam particles ionized at the plasma edge can support and excite an instability. Given the beam velocity (around 100 keV), the mode excited can be only electrostatic, thus, we can take the electrostatic limit of the dielectric tensor 2.33 in the straight-line homogeneous case and inject it into the dispersion relation to get back to the equation used by Dendy for his theory:

$$\sum_s \frac{\omega_{ps}^2}{k^2} \sum_N \int d^3v \frac{J_l^2(k_\perp v_\perp/\omega_{cs})}{k_\| v_\| + N\omega_{cs} - \omega} \left(\frac{l\omega_{cs}}{v_\perp}\frac{\partial F_s}{\partial v_\perp} + k_\| \frac{\partial F_s}{\partial v_\|}\right) = 1 \quad (2.94)$$

where s represent either thermal ions with a Maxwellian distribution function or beam ions with a shifted Maxwellian function at the beam

velocity.

We compute the growth rate and the dispersion relation following the analytical simplification proposed in [18]. The results are presented on Figure 2.44 in function of the parameter $z_b = k_\perp u/\omega_{cb}$ where u is the perpendicular velocity of the beam ions at the edge.

We see that, provided that the ionization profile of the beam ions

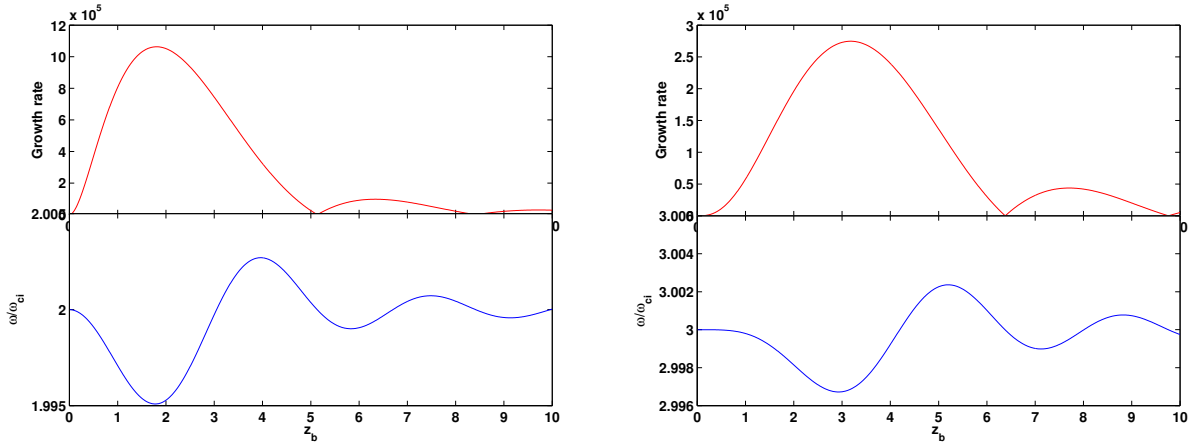

Figure 2.44: Growth rate and dispersion relation of the beam-driven ICE for N=2 (Left) and N=3 (Right)

is narrow in phase space, a wave can be both supported and excited by the beam itself. This requires a compromise on the edge density to have a sufficiently high level of ionization and a slowing down time long enough to keep the beam ions at their birth energy. This leads to a localized source of emission, which corresponds to what has been observed on other machines (cf. 1.4.1).

C/ Central ICE

No theory has been developed to model a potential central ICE, probably because of the lack of experimental data. We can note the attempts [39] and [38], which cover both electron and ion central emission. But they do not rely on experimental data and it is not clear whether the assumptions are valid for ASDEX Upgrade. Instead of developing a theory from scratch, we will postpone its construction after we have presented the experimental results to use them as a basis for an explanation of the emission.

However we can still mention some guidelines to interpret some potential data coming from the center in the ion cyclotron range of frequencies. The excited wave can be electrostatic (like the Bernstein wave) or electromagnetic (like the fast wave). The first one has the advantage to require less energy to be excited: beam ions in the range of 100 keV have enough energy to excite them. The problem is that they are strongly damped in the plasma core where both density and temperature are high. The chances are low on a machine of the size of AUG for this emission to reach the edge with an intensity sufficient to be detected. The fast wave requires far more free energy to propagate and can be excited only by super-alfvénic or almost super-alfvénic ions; the only candidates are the fusion products, especially

the proton. Therefore, our main concern for the analysis of the data will be to discriminate between these two potential candidates.

3 Hardware

This section is dedicated to the description of the hardware used to carry out our measurement of the Ion Cyclotron Emission. In the first part, we will give an overview of the ASDEX Upgrade tokamak, on which the observations were conducted, including the main operational parameters, the heating systems used and the diagnostics relevant for the study. In the second part, we will focus on the dedicated diagnostic develop to measure the instability and to process the data.

3.1 ASDEX Upgrade

3.1.1 Machine

The tokamak ASDEX Upgrade, located in Garching at the Max Planck-Institut fur Plasmaphysik (IPP) started its operations in 1992. Its parameters are listed in Table 3.1. The magnetic field is created by 16 toroidal field (TF) coils, each defining one sector of the machine and the poloidal magnetic field is produced by a usually counter clockwise directed plasma current I_p [0.6-1.4 MA] that is mainly driven by a central transformer coil. The vertical position of the plasma is controlled using a passive stabilizing loop (PSL) and active poloidal field coils. External coils are used to balance the varying magnetic field from the transformer coil and to generate an elongated, triangular shaped magnetic field structure since circular plasmas are less stable with respect to MHD modes. The first, i.e. inner, wall of the experiment is made of tungsten coated graphite tiles which tolerate large heat loads and which have a high sputtering threshold. The generated plasmas mainly consist of deuterium, as tritium would activate the machine and as hydrogen is less fusion reactor relevant. The duration of plasma discharges is up to 10 seconds which is a multiple of the global confinement time. Its name is derived from the german **Axial Symmetrisches Divertor EXperiment** which refers to a special magnetic field configuration which was successfully tested on several machines. In the divertor configuration, the outermost flux surfaces are not closed but end in the divertor region (see Figure 2.20). Particles expelled from the plasma do, consequently, not impact on neighboring walls. Plasma experiments in fusion devices are also called discharges or shots.

Characteristics	Value
Major plasma radius	1.65 m
Minor plasma radius	0.5 m
Plasma elongation	1.6
Plasma current	2M A
Discharge duration	10 s
Plasma density	<3.10^{20} m^{-3}
Magnetic field	< 3.9 T

Table 3.1: Main characteristics of ASDEX Upgrade

3.1.2 *Heating*

There are three auxiliary heating systems on AUG: neutral beam injection, ICRF and ECRF. The last one has never lead to any observation of ICE and has not been involved in the discharges where ICE took place. We will consequently focus only on the two first ones.

Neutral Beam Injection

This method consists in adding power to the plasma through the transfer of energy momentum from energetic particles to the background plasma. Because of the strong toroidal field, there is no way to inject energetic charged particles directly in the core of the plasma (where the energy is needed). Instead, neutral particles are injected from outside: they do not interact with the magnetic field until they are ionized by the background plasma on their way to the center.

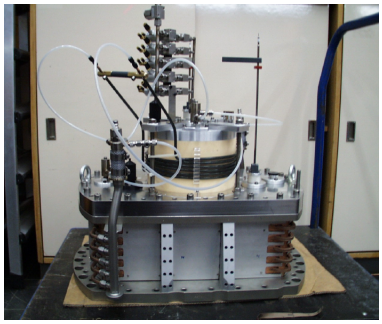

Figure 3.1: an experimental RF ion source tested at IPP.

The different steps involved in the plasma heating through an ion beam are briefly summarized in Figure 3.2. A plasma discharge is first initiated in an ion source (an example can be seen of Figure 3.1) and the ions are immediately extracted by an electrical potential: for a Deuterium beam (the mostly used species used on AUG), it produces ions: D^+, D^*, D_2^+ and D_3^*. These ions are then accelerated at a high energy E_0 and neutralized with different efficiencies. They are after that injected as a beam inside the plasma near the equatorial plane for better efficiency. In the plasma, the molecules are dissociated and ionized at full energy E_0 but also at $E_0/2$ and $E_0/3$. The ionization is due to the impact on electrons, charge exchange and multi-step ionization.

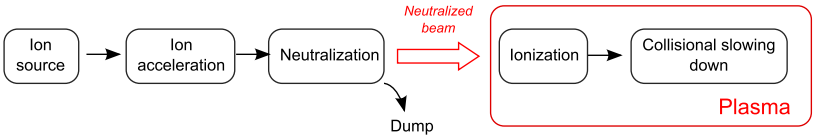

Figure 3.2: Schematic principle for injection of neutrals inside a tokamak plasma.

The NBI system on ASDEX Upgrade has two boxes with each four ion sources. The first box works at 55 kV for Hydrogen and 60 kV for Deuterium (the main scheme). The second box at 70 kV for Hydrogen and 93 kV for Deuterium. The total amount of power that can be injected in the plasma is 14 MW with Hydrogen and 20 MW with Deuterium.

ICRF Heating

As for the technology involved, the ICRF system consists of three

main subsystems:

- the high power RF source which are, most of the time, vacuum electronic tubes with four electrodes and called (tetrodes),
- the transmission line and matching system: in this range of frequencies and at the MW power levels, the best solution for guided transmission is the coaxial transmission line. The matching system tunes the value of the antenna coupling impedance to the impedance of the generators, optimizing the delivering of power into the plasma,
- the antenna which is an array of current straps fed by the coaxial lines. The straps are protected against the plasma interaction by a Faraday shield, a structure made of conducting metallic rods.

The advantages of ICRF heating are the localized heating, the broad range of magnetic field over which the heating is efficient, the technology is relatively cheap and flexible. The disadvantage is the difficulty of coupling the wave through the evanescent layer ([5], [11]) and the problems of sheath rectification ([10], [19]) leading to increased impurity sputtering into the plasma. We have to emphasize that many experiments during the thesis where impaired by this kind of problem due to the increased use of tungsten on ASDEX Upgrade, forcing the ICRF operators to limit the electromagnetic injected power in the plasma.

3.1.3 Diagnostics

We present here the main diagnostics which were useful for our studies.

Magnetic measurements (EQE code)

The equilibrium is calculated by the CLISTE code which solves the Grad-Shafranov equation for a toroidal configuration. An iterative approach is used based on the information from the 63 magnetic pick up coils that measure the local poloidal magnetic field at their position, and from 18 flux difference measurements as well as information on the currents in the TF-coils, the ohmic transformer, the poloidal shaping coils and the PSL are used.

Electron temperature (ECE)

The electron temperature is measured by the electron cyclotron emission (ECE) diagnostic with a high temporal resolution (up to 1 MHz). The diagnostic observes the cyclotron radiation of gyrating electrons along its viewing direction. The radial position of the observed cyclotron radiation depends on the frequency as the latter is a function of the magnetic field strength. At the position of the so called resonance of a given frequency, the plasma is optically thick which means that Planck law can be applied to infer the electron temperature from the intensity of the measured radiation.

Electron density (IDA, LID) The electron density profiles used in this work are taken from an integrated data modeling approach

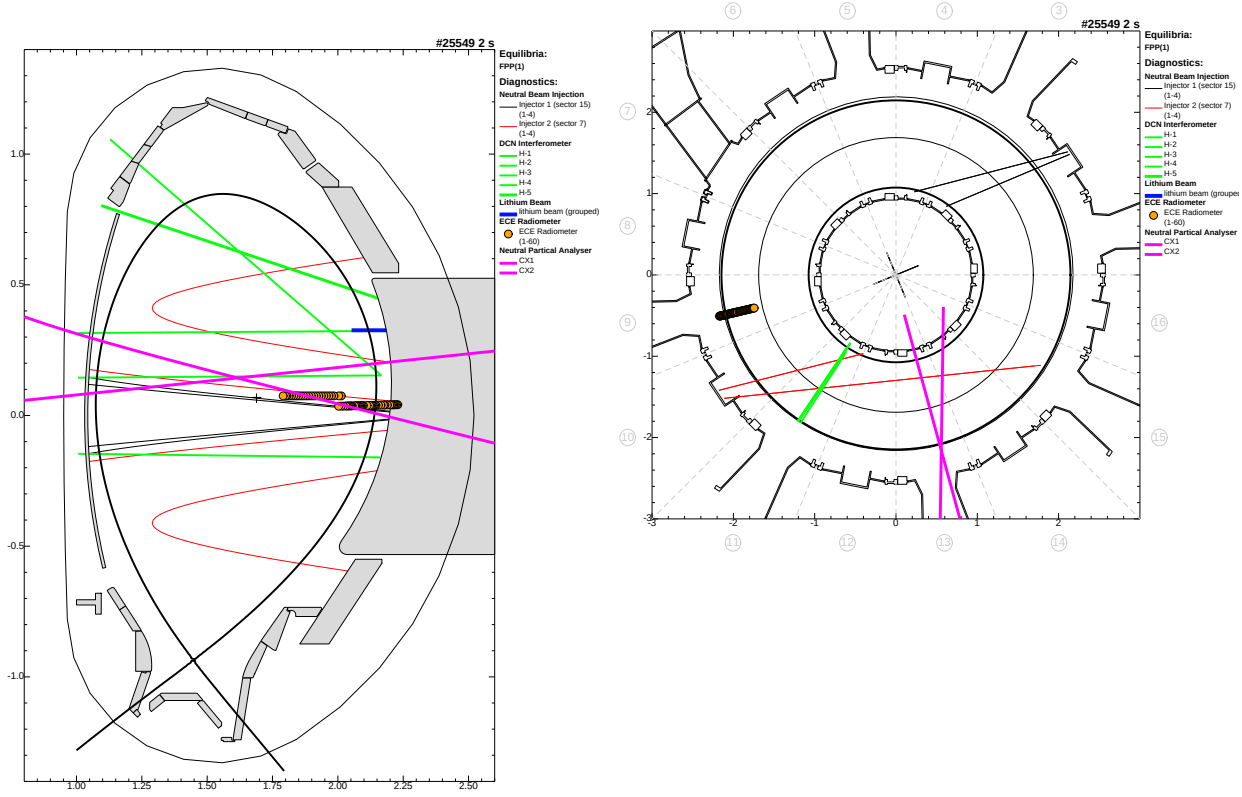

Figure 3.3: Side- and upper view of the locations of the heating systems and diagnostics used in this study.

(IDA) that combines the measurements of two diagnostics. The line integrated measurements from interferometry are used to obtain information on the electron density in the plasma core. Five (H1 to H5) laser beams are used to determine the line integrated electron density. The laser beams pass through the plasma and experience a phase shift relative to a second beam that does not propagate through the plasma. By analyzing the interference pattern between the two lasers, the line integrated electron density can be determined. On the other hand, a Lithium beam diagnostic measures the electron density at the plasma edge. Lithium neutrals are injected into the plasma with injection voltages of up to 50 keV at about 30 cm above the mid plane. The lithium neutrals are excited and ionized when penetrating into the plasma. The ionization, the excitation and subsequent photon emission depend mainly on the electron temperature and electron density. Knowing the electron temperature from the ECE measurement, the radial profile of the light intensity of the injected lithium neutrals is used to calculate the electron density. The time resolution of the lithium beam diagnostic limits the time resolution of the electron density profiles computed by IDA. It is in the order of 1ms.

Fast Ions Loss Detector (FILD) The fast ion loss detector acts as a magnetic spectrometer, dispersing fast ions onto a scintillator, with the strike point depending on their gyroradius (energy) and pitch angle (angle between ion velocity and magnetic eld line) [29]. The emitted light pattern allows particle identification in the phase space

with a high time resolution.

3.2 *Diagnostic to measure Ion Cyclotron Emission*

3.2.1 *Hardware*

The main difficulty with radio-frequency measurements is the optimization of the Signal to Noise Ratio (SNR): we have to maximize the amount of useful information and to decrease the background noise and other disturbances. This is particularly difficult in the case of mICE given that the measurements are supposed to be carried out during ICRF operations with a high amount of power present in the vacuum vessel exactly in the ICE range of frequencies.

Techniques to measure frequency spectra have considerably progressed in the last ten years thanks to the development of digitizer boards which can acquire signals in the MHz and GHz range over several seconds. Our study has benefited from these advances and made it possible to find new results which were impossible to access with the analog spectrometer used in the ICE studies on JET or TFTR. However, a digitizer, even good, can acquire only the information contained in the signal at its input: if the quality of this signal is not good enough, no relevant data will be retrieved from the sampled data. Thus, the signal conditioning between the captor and the acquisition system has to be carefully designed.

As seen on Figure 3.4, the measurement setup is divided into three parts that we describe in more details in the next paragraphs. At the beginning of the study, there were uncertainties about the nature of the signal that we wanted to record, which made it difficult to write accurate specifications for the diagnostics to develop. Therefore we designed as flexible as possible so that it can pick up a wide range of signals, both electrostatic and electromagnetic and using a maximum of existing hardware to limit the costs. As a result, we used RF probes already installed on the tokamak but which calibration data were missing and we benefited from the acquisition system in charge of measuring arc events in the ICRF system. This has limited the time of availability since the system was shared between our study and projects on arc detections.

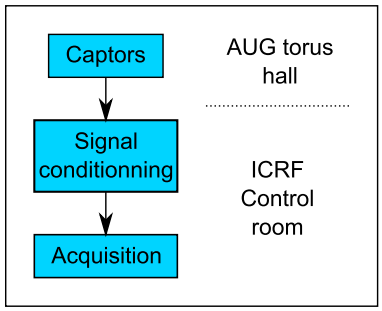

Figure 3.4: Overview of the diagnostic architecture

Captors The design and development of new captors would not have fit in the time frame of the study. As a result we have used two electromagnetic probes already installed in the vacuum vessel of AUG (and almost forgotten...). These two probes are cross-dipole antennas (cf. Figure 3.5) located near antenna 4, one at the low field side and the other at the high field side. No calibration data was available for these probes and no time window was found to unmount and calibrate them. However we used the conditioning of the ICRF system to get an idea of the attenuation factor of these probes. Indeed, during this operation aiming at cleaning the components of the auxiliary heating system, the ICRF antennas inject several hun-

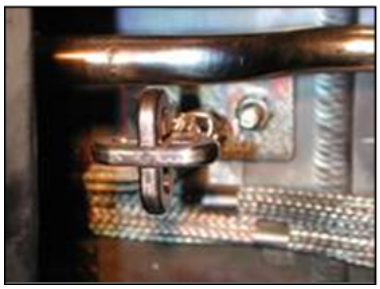
Figure 3.5: Cross-dipole antenna on the HFS of AUG.

dred of kilowatts inside the vessel. The injected power being known through the internal ICRF measurements, we can evaluate the fraction of the power received by our RF captors. During this operation, it appeared that the captor located on the low field side had a very poor transmission factor, giving a very low and distorted signal. As a result, most of our results were based on the remaining probe.

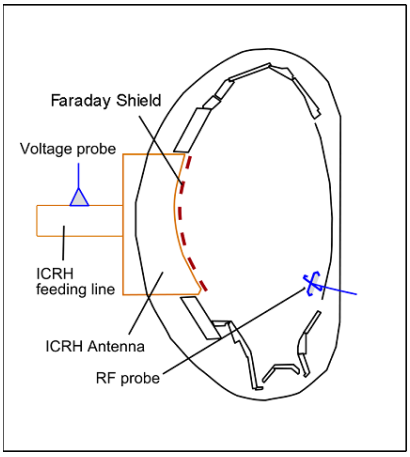

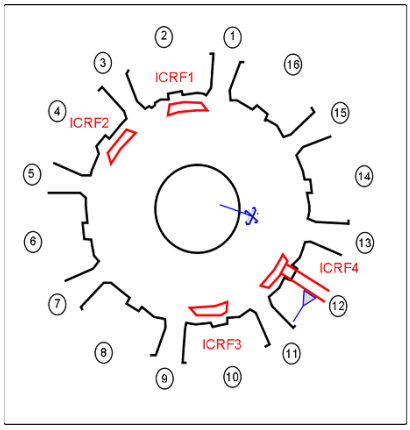

Figure 3.6: Top view of captors location.

However, other sources of information were available to confirm the data from the RF probe, though not with the same quality. These sources were the voltage probes located inside the ICRF antennas. The antennas benefit from their large surface but any signal is attenuated by the Faraday Shield that protects the straps from the hot plasma and remove electrostatic components from the waves. In addition, the ICRF system is matched for one given frequency and tends to strongly attenuate all other frequencies. In spite of these drawbacks, it would have been interesting to measure the signal on all antennas but the limited number of channels of our acquisition system and the fact that most voltage probes were already used for ICRF routine diagnostics constrained us to measure only one voltage signal on the antenna 4. The voltage probe was mounted near a maximum point of the voltage profile in the transmission line and gave us a satisfying SNR.

Signal conditioning This is the delicate part of the acquisition, the part where most of the SNR increase is gained. The first element of the signal conditioning chain is a tunable notch filter that eliminate the main ICRF frequency which pollutes the signal. The filter is not used when there are NBI-only operations.

An additional 1 MHz high pass filter is used to remove the low-frequency background noise and as a safety device to protect the digitizers against the surges initiated by arcs.

An anti-aliasing filter with a cut-off frequency at 100 MHz was also tested to see whether it could improve the quality of the signals. It was removed because, although it cleared all spurious frequencies, its attenuation factor was so high that the end result was less good

in SNR.

The last element of the signal conditioning chain is a low noise 30 dB pre-amplifier which increases the intensity of the received and filtered signal. This is a key element that made it possible to detect signals even from the center where they have undergone a strong attenuation.

Acquisition Our first attempts to acquire the frequencies of the signal were realized with an analog oscilloscope, which has the advantage to provide a high quality signal without all distortions due to digital effects. The results, like on Figure 3.7 showed that there were indeed frequencies present in the vacuum vessel (their intensity was higher than the intensity of the signal inside the transmission line). The difficulty was to locate the emission time of these frequencies during a plasma discharge to determine the criteria for their development.

Consequently, we decided to developed a more advanced acquisition system with the main requirement to be able to visualize the evolution of these frequencies during a shot. We used the idea of the Thomson scattering diagnostic, which probes the plasma with pulses of lasers at a given pulse rate of several Hertz. We did the same with a far higher pulse frequency to get a spectrum every 15 ms.

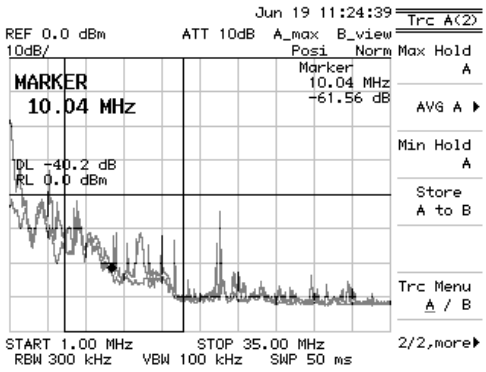

Figure 3.7: Example of a spectrum acquire with an analog device.

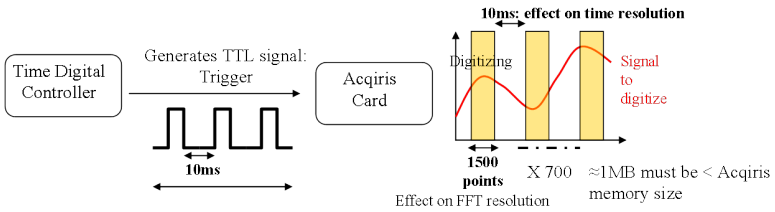

Figure 3.8: Method of acquisition of the signal triggered by a train of TTL pulses.

The central part of the acquisition system is an Acqiris digitizer with 2 cards of 4 channels each. The digitizer is connected to a time digital control (TDC), the purpose of which is to trigger acquisition signals in the digitizer at a given pulse rate. The Acqiris cards are connected through a PCI interface to a Sun workstation in charge of the control of the digitizer and of the archiving of the data. The Acqiris digitizer have a sampling rate up to 500 MS/s with a bandpass of 100 MHz, which is suitable for the kind of phenomena to observe. Each channel has a memory of 2 MB.

The principle of the acquisition is the following one: the digitizer is switched on in stand-by mode by the TDC when the signal TS06 (sent by AUG to signal the beginning of a shot) arrives. From this point on, the TDC sends a trigger signal to the digitizer every predefined time interval, say 15 ms. When the digitizer receives this trigger, it starts to acquire a small amount of data, actually enough points to make a FFT with the required accuracy. Then it stops and waits for the next trigger from the TDC. The number of trigger impulses and the interval between them is set up to cover the whole

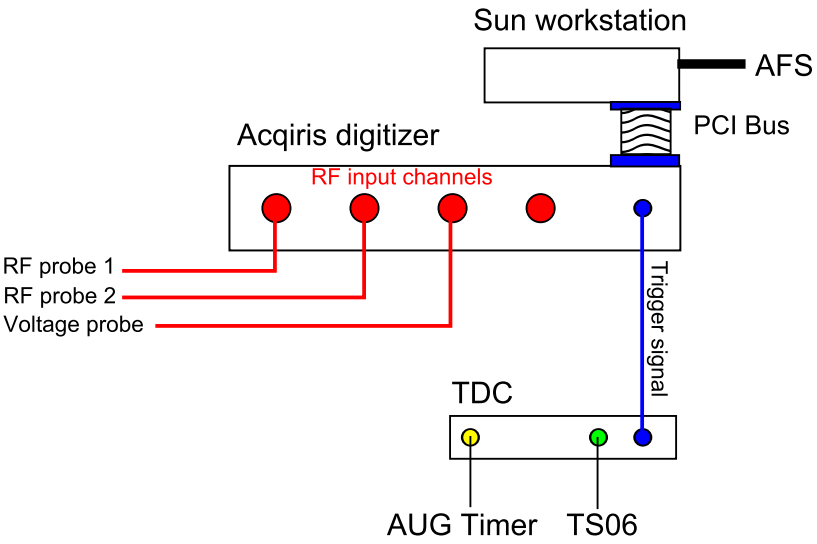

Figure 3.9: Configuration of the acquisition system

duration of the shot. The amount of data recorded for each trigger is also limited by the memory size of the digitizer: the sum of data recorded during all the pulses should fit in the memory. We thus have a double constraint on the number of points to be acquired during each pulse. But in the end, we have in the memory of one channel a sequence of data corresponding to the different pulses.

The capacities of this acquisition system represent a big improvement over the devices used 15 years ago for the investigations of the Ion Cyclotron Emission. This will make it possible, as we will see it later, to get more precise information on the nature and the behavior of this emission.

However we have to be clear on the limitations of the system; there are three of them:

- the upper cut-off frequency of the digitizer at 100 MHz, which is too low to see some ICE phenomena above the fifth harmonics of the ion cyclotron frequency. But we will go back to this topic in the further sections.
- The 7 bits resolution of each channel; modern digitizers can have a resolution up to 12 bits. Here we cannot hope to get the fine evolution of the signal.
- The limited memory of 2 MB per channel. If it is an improvement over the analog spectrum analzyers, it is limited in comparison with modern digital oscilloscopes which have memories above 12 MB.

These limitations mostly come from the fact that we wanted to use existing material. For the future, these limitations have to be taken into account in the specifications of a potential ICE diagnostic.

3.2.2 *software*

The software development ranged from the device driver in C to control the interface between workstation and digitizer to the Matlab program to analyze the results.

Control of the acquisition It involves two steps: the control of the interface between the digitizer and the workstation; this is achieved with the device driver. And the setup and command of the digitizer during the acquisition.

- the driver: it controls the flow of data at low machine level. It is based on an old version of the driver for the Thomson scattering diagnostic. There are two modes of transfer between the digitizer and the computer: the classical bit by bit operation or the Direct Memory Access (DMA) where the whole memory of the digitizer is transfered in one shot to the computer. This latter method is very fast and would make it possible to transfer a bigger part of the memory during two pulses than with the former method. Therefore we focused at the beginning on this method and modified the driver to support it; one difficulty is that the size of the digitizer memory is 2 MB but the memory of a Sun workstation running on Unix is divided in pages of 64 kB length: it is called pagination control. The transfered data have to be split between different pages. The mode was successfully tested on several shots but two problems occurred: first, the instability of the Unix operating system during the transfer: random fatal errors happened during some transfers of data without any obvious reasons to explain it. Second, to realize this mode, it was necessary to put the OS in real-time mode with the highest priority granted to the transfer of data in the workstation memory. This imply to be administrator to have enough rights to access this mode. And last and important problem, the speed of transfer was not as high as expected. As a result, we went back to the first mode, the bit-by-bit transfer, which in spite of its low speed, was stable and user-friendly enough for our needs.
- the control software: it represents the high-level layer: it is where the acquisition parameters are set up and where the control of the digitizer takes place. The configuration is done with a simple text file: the main parameters include the voltage amplitude to be recorded by each channel, the nature of the signal (DC, RF), the number of pulses, the interval between them, the sampling rate,... The configuration file is processed by the control software that sends the setup data to the digitizer during the initialization.

Data processing The last software component concerns the processing of data after their acquisition. Data saved on the workstation are raw, only attached to the configuration parameters of the digitizer. Data are first converted to a Matlab file and provided with

a header containing the meta-data (shot number, sampling rate and some other AUG parameters). The data are then saved in a database dedicated to ICE. We chose Matlab after a benchmark with IDL because it was faster to develop a code and to interface with existing routines.

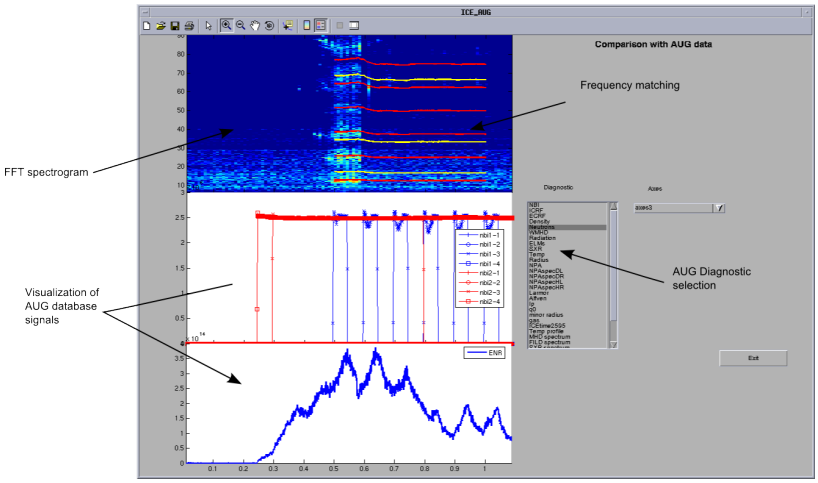

Figure 3.10: Screenshot of a typical session of *ICEAnalysis*, with the spectrogram and database signal windows.

All routines to analyze the data are gathered in a single interface called *ICEanalysis* which also integrates the database of ICE discharges. For each shot, it is easy to recall the shot data from the AUG journal and to visualize the frequencies of the discharge. There are in addition two main tools to interpret the data. The first one is dedicated to the FFT analysis of the data. It makes possible to display the spectrogram of the signal, i.e., the Fast Fourier Transform for each time slice corresponding to a pulse. This part of the code also enables frequency matching which consists in overlaying the ion cyclotron frequency calculated with the magnetic data from ASDEX Upgrade at a given location inside the plasma. The second part displays the AUG data from other diagnostics and relevant to ICE to compare their evolution with the evolution of the emission.

4 Observations

We now deal with the results of the measurements carried out during several campaigns of ASDEX Upgrade. We have sorted the results in three categories: the edge ICE during NBI injection, which covers both FP and beam-driven ICE; the ICE during ICRH and the central ICE. We have kept FP and beam-driven ICEs grouped because of the difficulty to discriminate them. This may be related to a flaw in our measurements (the impossibility to determine the wavevector $\mathbf{k}$) but there could also be a more profound relationship between these two types of emission and we would not like to miss it.

For each category of ICE, we will analyze the data in this order: inspection of the emission characteristics in frequency domain (mode structure), evolution in time of the signal, condition of existence (in terms of the plasma parameters, heating power,...), and the relation with other instabilities.

We have to keep in mind, as explained in the previous chapter, that the experimental setup does not make it possible to evaluate the wavevector. The task of analysis has thus to rely on the theoretical models from Section 2.2.1 to relate the observed frequencies to the wave vector $\mathbf{k}$.

4.1 Edge ICE during NBI

We start with the observation of the edge ICE during NBI heating, which has been the most studied emission on other machines.

4.1.1 Frequency structure

A standard spectrogram measured during edge ICE with NBI is presented on Figure 4.1. The first step is to verify the matching of the observed frequencies with the edge cyclotron frequency of the different species (we take $r = 0.95\ a$ for the measurement of B). This makes it possible to conclude on the relation between the signal and the cyclotron frequency of the species with the correlation on the magnetic field and classify the different frequencies. The matching is presented for one case on Figure 4.2.

We observe three different types of frequencies: two that correspond to the harmonics of the deuterium cyclotron frequency, with a small shift towards lower values for the first one and a bigger shift for the second one; it is clearly visible on the Figure 4.4. A third

frequency that corresponds to Helium-3, also a fusion product[1], is also visible. One type is quite low in intensity, noisy and wideband (sometimes up to 2MHz). The other is higher in intensity and has a narrower bandwidth (below 100kHz). By analogy with what is observed on TFTR or on JT-60U, the first type of frequencies is called beam-driven ICE and the second type proton-ICE. We do not have any way to distinguish their wave vector.

[1] We have never observed frequencies that could correspond to Tritium

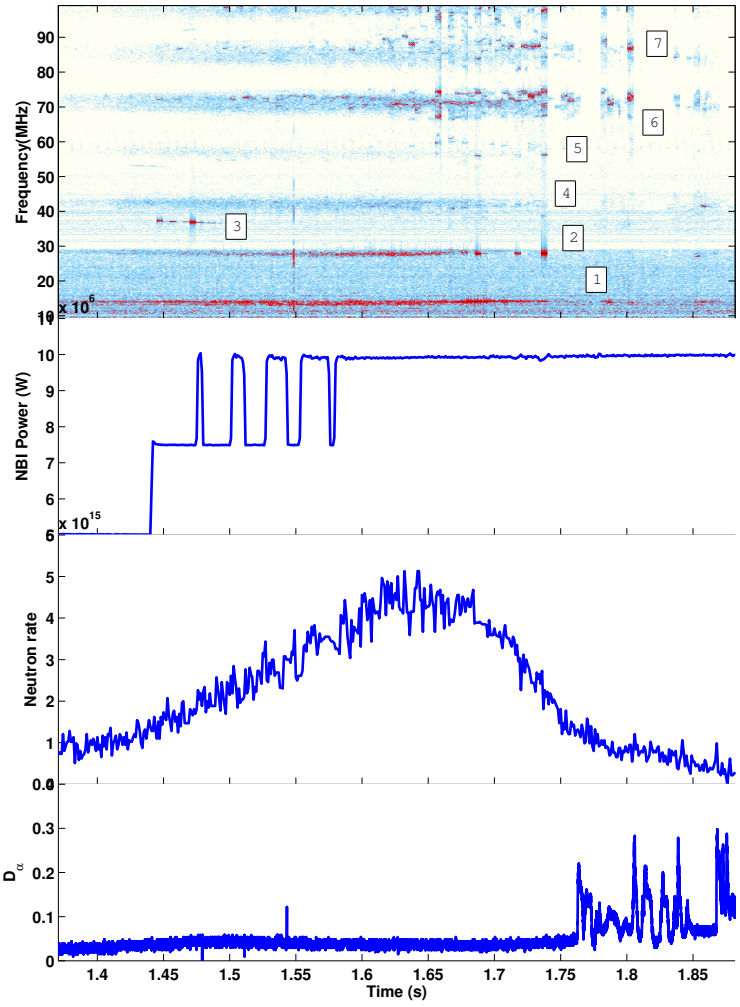

Figure 4.1: Shot 26915 - Spectrogram and evolution of the main discharge parameters related to ICE. The lines 1, 2, 4, 5, 6 and 7 correspond to harmonics the Deuterium cyclotron frequency at the edge (from 1 to 6). The line 3 to the second harmonic of He^3.

We have plotted on Figure 4.3 the evolution of the shift for the two types of ICE in function of the edge density. The shift of the FP-ICE is rather independent from the density but the shift of the beam-driven ICE shows a clear increase when the density grows up.

On some rare cases, a fine structure can be visible on the proton ICE spectrum, with at least a peak at the second harmonic. But the signal is very transient and it is difficult to measure a spectrum with a good accuracy. The He-3 spectrum can also present a doublet as shown on Figure 4.8. The signal of the beam-driven emission is low and noisy and, consequently, difficult to interpret. However, for

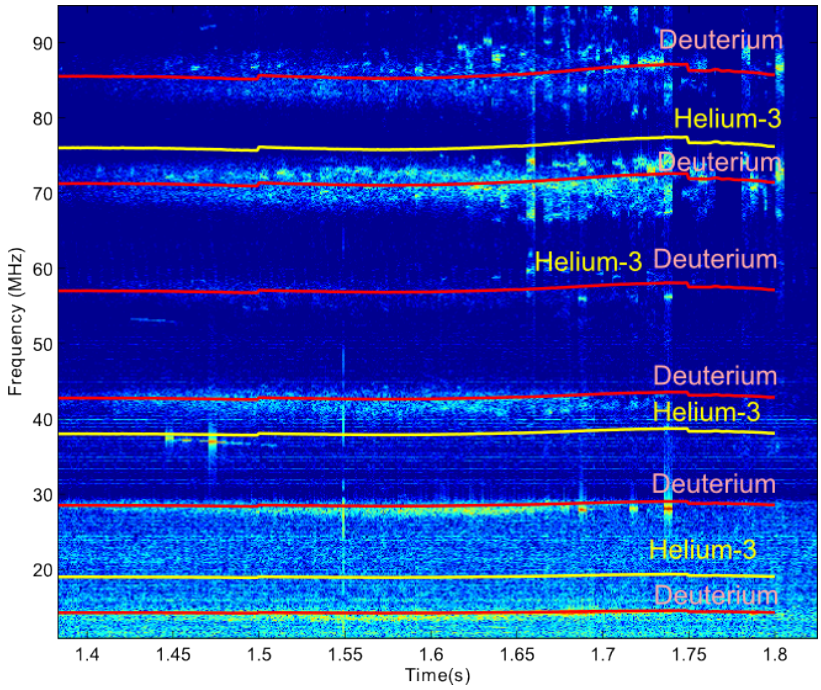

Figure 4.2: Frequency matching for the spectrogram of Figure 4.1. The red lines correspond to the harmonics of Deuterium. The yellow lines, to harmonic of He^3. Some of them are degenerate and are not visible.

some discharges, it is possible to observe a structure on the spectrogram, as on Figure 4.5.

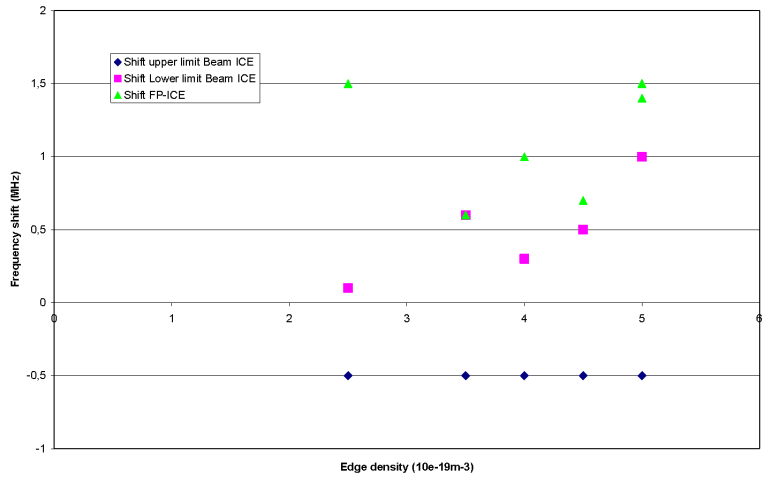

Figure 4.3: Shift of frequencies of beam-driven ICE and Fp-ICE in function of the frequency. The shift is positive towards the lower frequencies (.i.e. outside the the plasma). There is a clear widening and increase of the shift of the beam-driven ICE with increasing density.

If we consider the harmonics present, we have, for FP-ICE, mostly the 2nd and 6th harmonics with a strong intensity. But a signal is also visible at the 1st and 3rd harmonic. On one case, the third harmonic is even the most intense (cf. Figure 4.4). This is surprising because, if the emission is excited by protons (which has the higher concentration and the more free energy), it should not appear at these half harmonics of the deuterium cyclotron frequency.

But this phenomenon has been detected also on other machines and is one of the intriguing issues of ICE theories. For He-3 ICE,

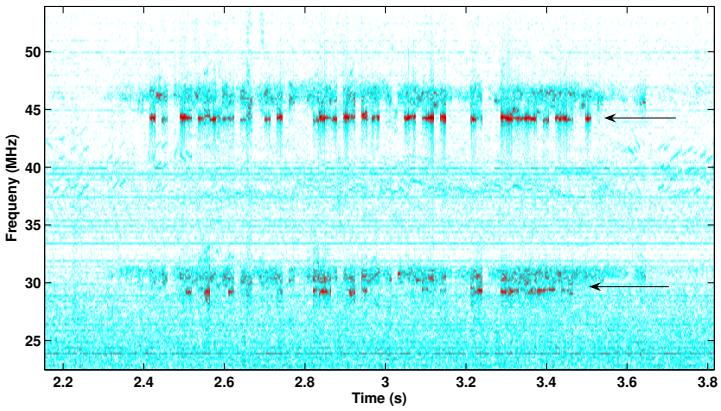

Figure 4.4: Shot 27093 - Case with dominant third harmonic. The arrows correspond to the second and third harmonics. The distinction between the wide band beam-driven ICE and the proton-driven ICE is also clearly observed.

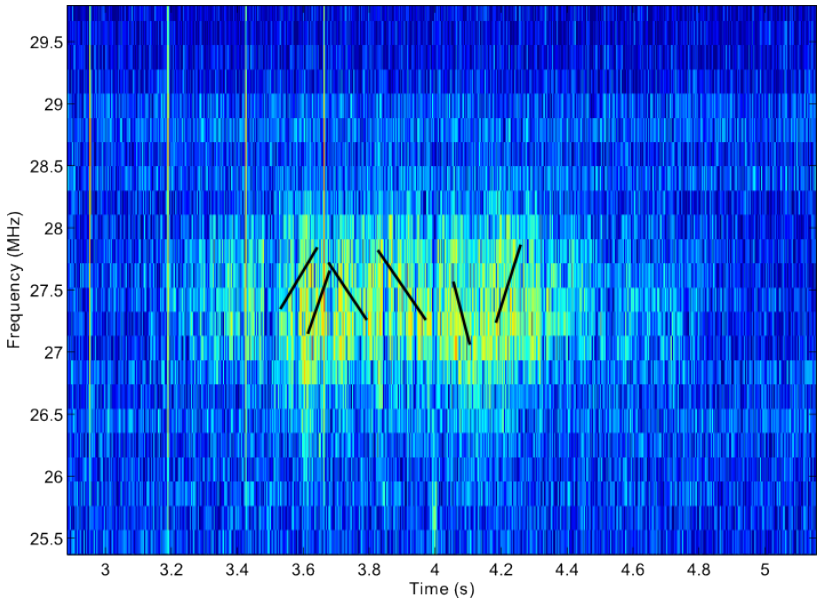

Figure 4.5: Structure visible on the 2nd harmonic of the beam-driven ICE: they can be eigenmodes evolving in time but the signal is too noisy to draw definitive conclusions.

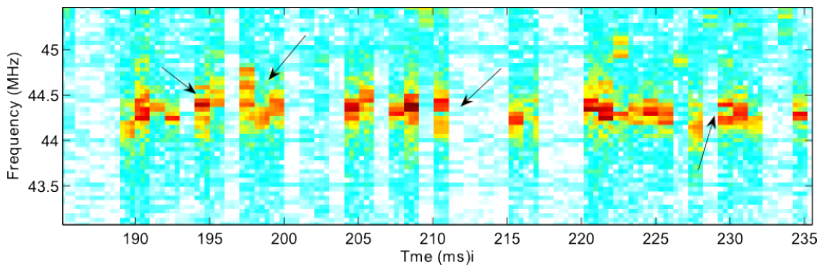

Figure 4.6: Structure of the 3rd harmonic of Deuterium cyclotron frequency- Splitting visible in doublets and triplets. Shot 26915.

generally only the second harmonic is present.

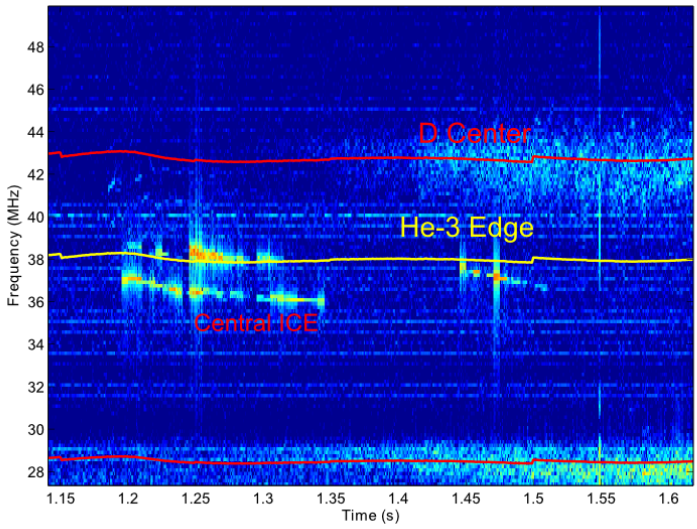

Figure 4.7: 2nd harmonic of He^3 during NBI injection - Shot 26915. The lower frequency corresponds to Central ICE (cf. 5.3).

Beam-driven ICE is excited at the various harmonics, except the fourth one which is never observed (it is not present for FP-ICE). It is not clear if it is due to a "hole" in our measurement system which accidentally rejects this range of frequency or whether there is a physical reason behind this absence.

The question of the upper harmonics is dubious on ASDEX Upgrade. Most of the time, we do not observe anything above the 6th harmonics, even when we increase the sampling rate up to 500 MS/s (cf. Figure 4.9). It may be due to the upper cut-off frequency of the digitizer but, for discharges with counter-current injection, we observe a mixture of different frequencies. On JET and TFTR, a continuum appears at high harmonics which carries most of the signal energy. It is not clear if what we see corresponds to this continuum. It could be an effect due to a bad anti-aliasing filter.

A last point concerns the experiments with reversed field (where we have counter-current neutral beam injection). As visible on Figure 4.10, all frequencies are strongly enhanced in intensity and widened in bandwidth. A surprising structure appears near the fourth harmonic of the Deuterium cyclotron frequency. It seems to be made of several modes increasing with time.

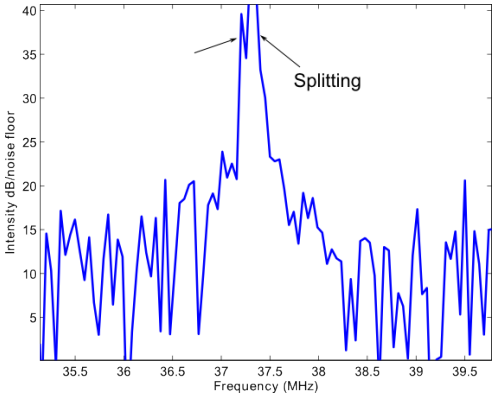

Figure 4.8: Splitting of He^3 frequencies near its second cyclotron harmonics. The signal is a bit satured.

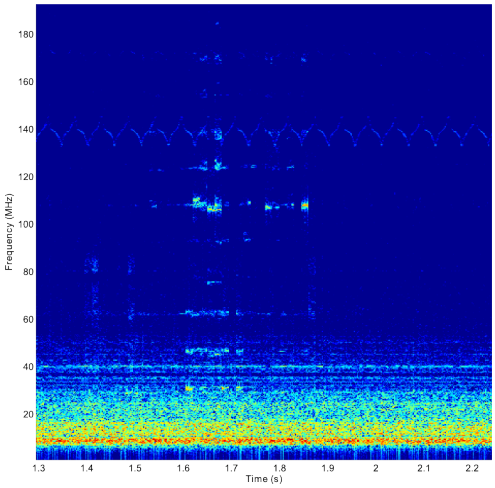

Figure 4.9: Spectrogram for acquisition at 500MS/s. No continuum is observed in the upper range of frequencies.

4.1.2 *Time evolution*

Concerning the time evolution of FP-ICE and beam-driven ICE, they present a visible difference (cf. Figure 4.4): the first one is transient, with bursts of emission, the second is steady state, continuous. Helium-3 ICE appears only at the beginning of NBI injection and lasts only for several tens of milliseconds. It disappears completely after that, except when there is a strong instability inside the plasma. Since the experiments where this frequency is observed were carried

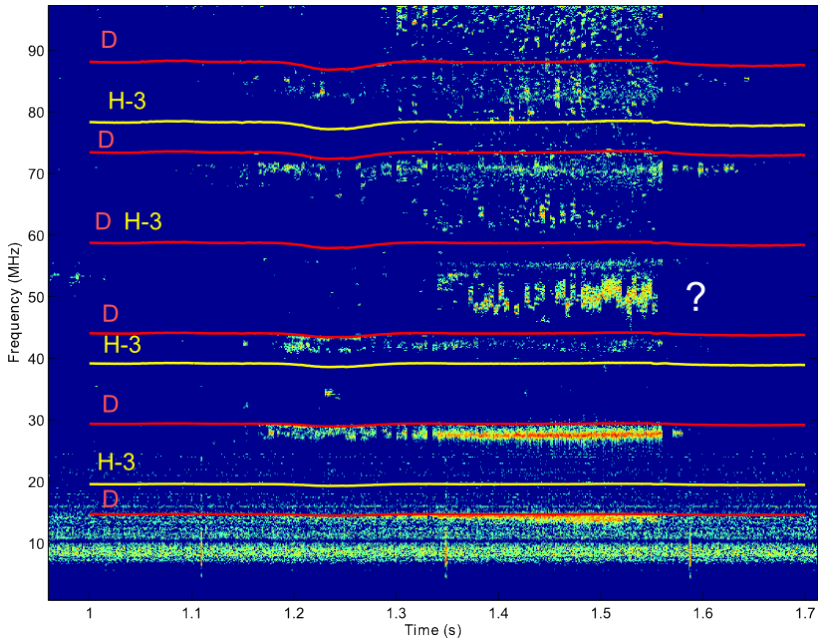

Figure 4.10: Shot 27287 with reversed field (counter NBI injection). The spectrogram is rich in frequencies: they are more intense with a wider band. They mix up for frequencies above 60MHz. The question mark indicate a small mode structure, the origin of which is unknown.

out only with Deuterium, the source of Helium-3 can only be the fusion reactions. The proton ICE is transient but can oscillate during several seconds, permanently emitting bursts of radiation, more or less intense. When we look at a sample of acquisition in a time window of 50 μs, we can see that even on this time scale, the intensity is strongly transient, oscillating from 0 to 100 %, which is coherent with what was observed on TFTR. It is interesting to note, that the evolution of the signal presents a regular structure, almost cyclic but with an intensity and a period that can vary from burst to burst.

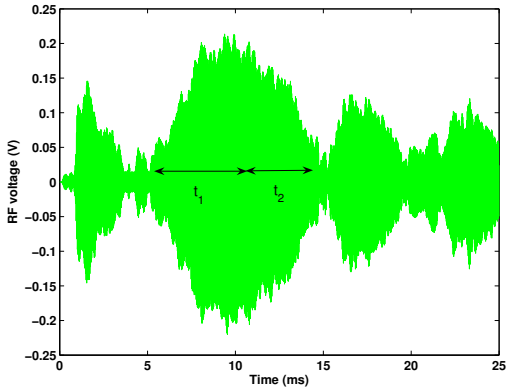

Figure 4.11: Time evolution of FP-ICE signal (2nd harmonic) on very short scales - Shot 26915. Bursts of emission are visible with a signal ranging from 0 % to 100 % of its value.

4.1.3 *Condition of existence*

The signal that correlates the best with the ICE observation, either beam-driven or due to FP, is the neutron rate. A neutron rate above a given threshold seems to be required to observe the ICE during NBI heating.. Indeed, the beam-driven ICE shows a direct dependence

between the neutron rate and its intensity (Figure 4.12). For FP-ICE, the correlation is less clear, mostly because the signal is too short and too transient to precisely determine its amplitude with respect to the neutron rate. But the signal is always present when the neutron rate exceeds a threshold of $10^{14}\ s^{-1}$.

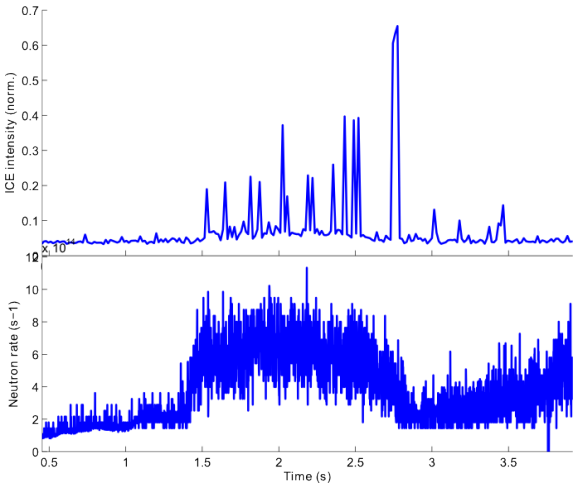

Figure 4.12: Correlation between the ICE signal and the neutron rate. Shot 26407.

4.1.4 *Correlation with instabilities*

As on JET or TFTR, we observe a clear correlation between the presence of the FP-ICE signal and instabilities either at the edge (ELMs) or in the center (sawteeth), instabilities that typically act on the population of fast ions.

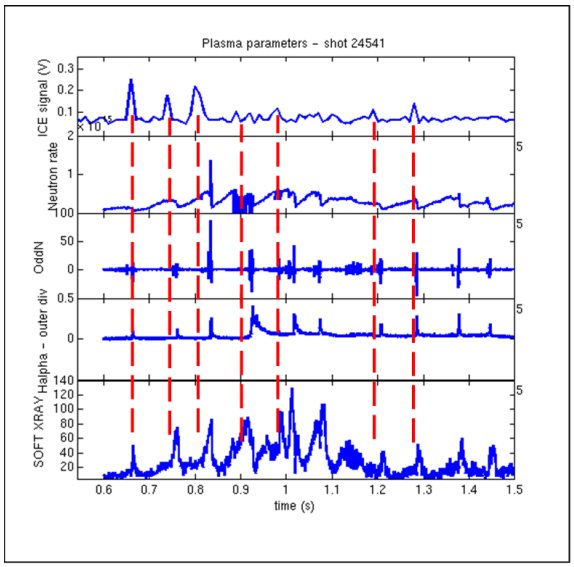

Figure 4.13: Correlation between ICE signal and ELMs. The limited accuracy of the trigger generator does not make it possible to know which one comes first.

Before turning on to the minority ICE, a last comment concerns the absence of results from the FILD: no losses of fast ions is correlated with the ICE signal. It means either that the FILD was not set up to receive the fast ions exciting the ICE (which should not be the case since it was configured on dedicated experiments to measure these losses) or it means that there was no or a very small

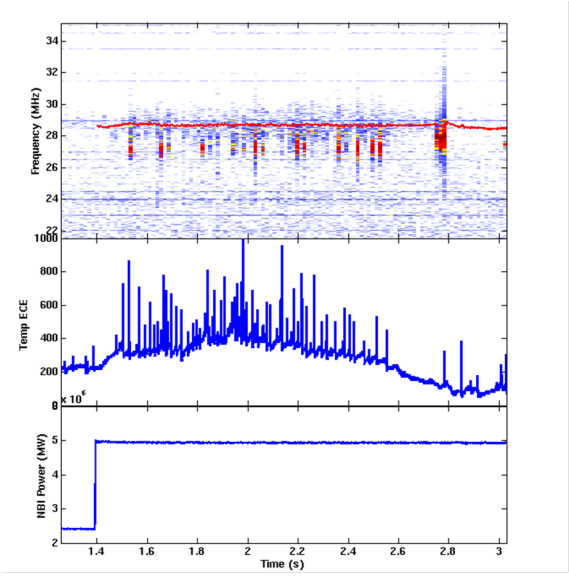

Figure 4.14: Correlation between ICE signal and sawteeths.

amount (too small to be measured) of fast ions lost from the plasma. If this latter case is confirmed, we can draw two conclusions: first, the source of excitation is a population of confined ions (which is in agreement with the theory) and, second, the ICE interaction does not eject the ions from the plasma.

4.2 *Edge ICE during ICRF heating*

4.2.1 *Frequency structure*

The typical spectrogram is presented on Figure 4.15. The matching shows that the frequency is correlated with the magnetic field and the frequency observed corresponds to the Hydrogen principal cyclotron frequency at the edge.

The second harmonic can also be visible but with a far lower intensity. The principal harmonic can be modulated by the ICRF generator frequency to create new frequencies.

With ICRF, it was possible on some discharges to capture a long portion of several milliseconds of the signal and to make a high resolution spectrogram, revealing a fine structure of the m-ICE (cf. Figures 4.16 and 4.17). We observe three main types of frequencies, one separated by about 1 MHz, the other by 200 kHz and a third one, very small and not always present at less than 50 kHz (these values give an order of magnitude and depend on the plasma discharge, and more precisely on the density). The gap is rather constant between the frequencies except on some rare cases.

The number of sub-frequencies present on the spectrum depends on the discharge, it can vary between one and three visible. We observe that, on a short time scale, the number of modes excited vary with time and in a quite periodic way.

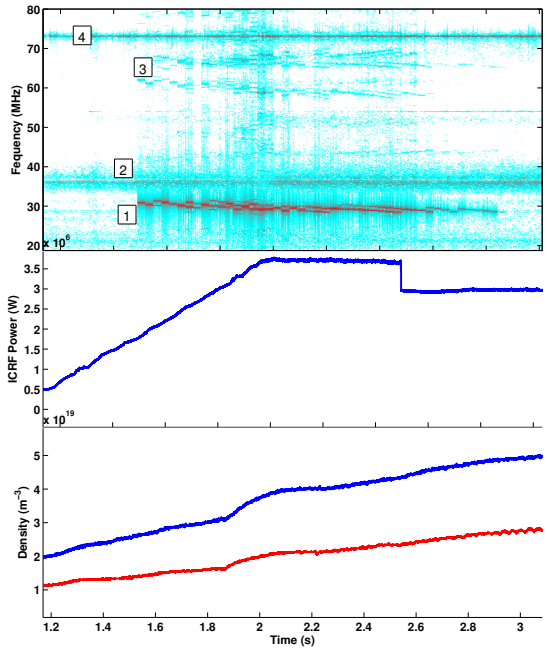

Figure 4.15: Spectrogram and main parameters during discharge 25549. 1 is the m-ICE at the first harmonic of hydrogen cyclotron frequency. 2 is the filtered ICRF frequency. 3 is the ICE at the 2nd harmonic and 4 is the non-filtered 2nd harmonic of the ICRF generator.

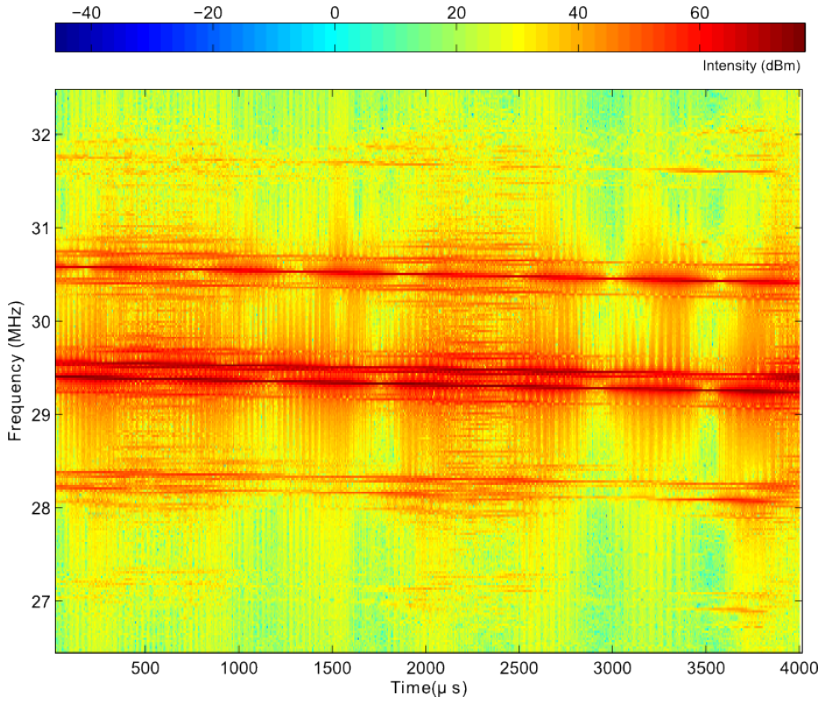

Figure 4.16: Spectrogram at high temporal resolution. Discharge 25549. The spectrum and its evolution can be measured with a good precision: substructures are present and their amplitude oscillates.

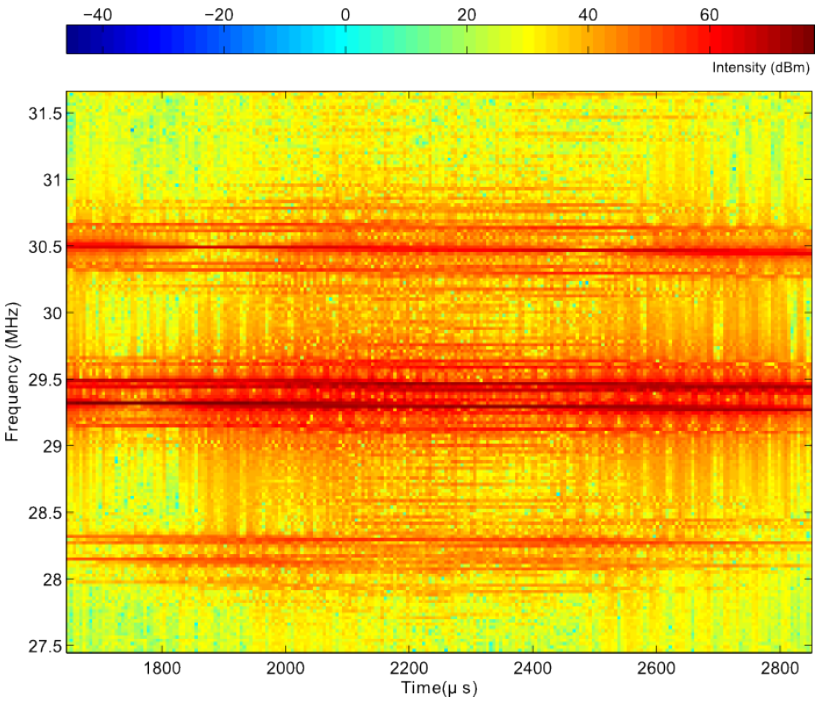

Figure 4.17: Zoom on Figure 4.16. We clearly see a structure of frequencies with three types of gaps: one large of 1 MHz, one large of 100 kHz and the smallest one of 50 khZ.

4.2.2 *Time evolution of m-ICE*

The frequencies can evolve in time: it is visible on large time scale or on short time scale. The boundaries of these frequencies evolve also in the same way. The signal is, in comparison with the FP-ICE, steady and can last for more than 1s. On short time scale, it evolves in bursts but with a longer duration than for FP-ICE: 5 ms instead of several microseconds.

4.2.3 *Condition of existence of m-ICE signal*

A precise criterion for the excitation m-ICE is given by the diagram ICRF power/density presented on Figure 4.19: It requires at least 3 MW of injected power for an edge density below $3.10^{19}\ m^{-3}$.

The intensity of the signal is also related to the injected power with a certain delay. This delay is also visible after the shutdown of the ICRF generators.

Another interesting feature appears on Figure 4.20 when the NBI heating is started once the m-ICE is already present: the emission extinguishes. It seems to be related to the decrease in Hydrogen as measured by the NPA at the edge.

In this case again, we were not able to see any fast ion losses with the FILD during the ICE signal.

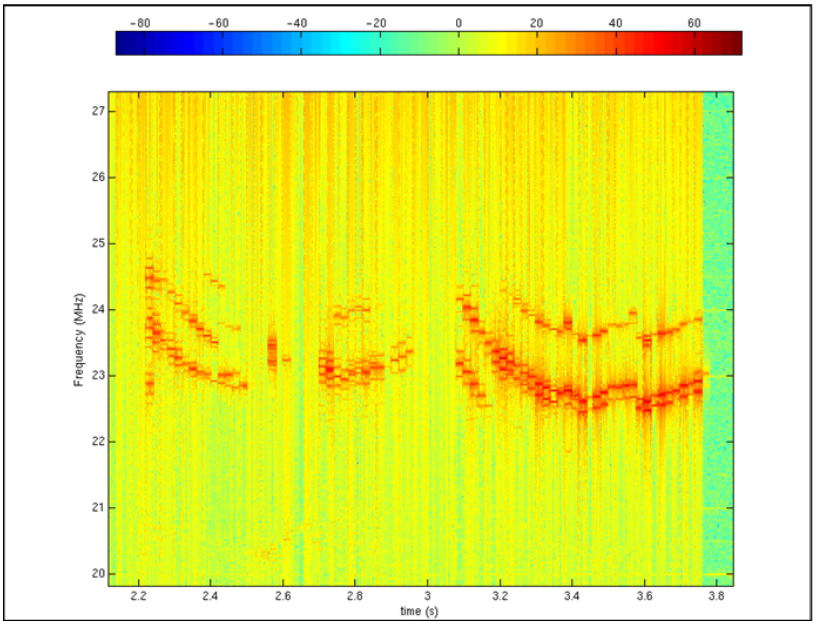

Figure 4.18: Splitting and evolution of frequencies. Discharge 23487.

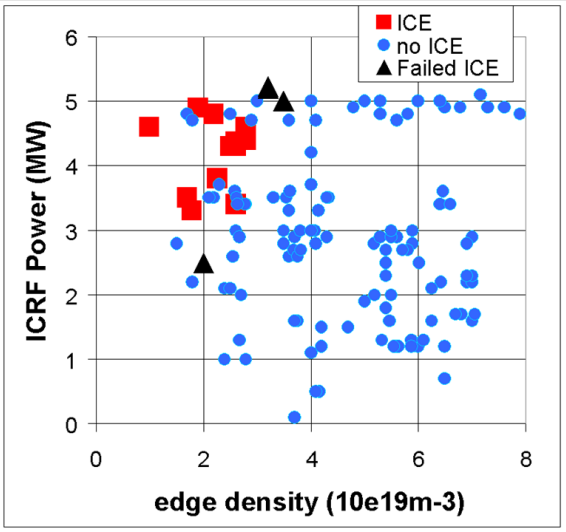

Figure 4.19: Domain of existence of mICE in function of density and injected power. The black triangles represented dedicated discharged destined to probe the limits of ICE excitation and that failed to trigger it.

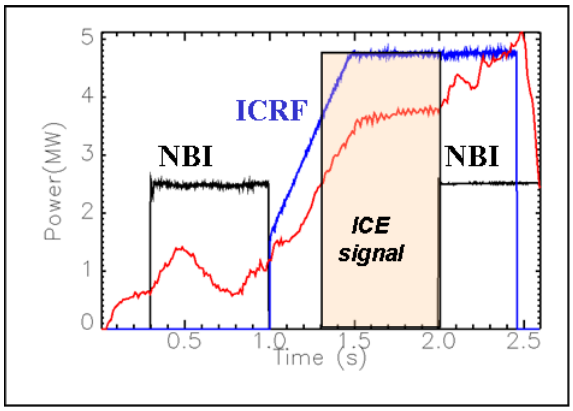

Figure 4.20: Extinction of the mICE signal when the NBI is started.

4.3 Central ICE

4.3.1 Frequency structure

The signal is in this case compared with the first harmonic of the cyclotron frequency measured on the magnetic axis. The matching is presented on Figure 4.21.

The reference cyclotron frequency evolves in time because the magnetic axis is moving and the magnetic field is in evolution. It is interesting to see that the measured signal perfectly follows this evolution: there is no Doppler shift in the usual case.

In some cases, "satellite" frequencies are visible and they evolve by diverging from the central frequency. The frequency is very narrow (below 50kHz) except in the reversed field case. The signal is sometimes synchronous with the Helium-3 edge ICE.

When the NBI beam is changed from 2 to 3, we can observe a jump from the 1st harmonic to the 2nd harmonic.

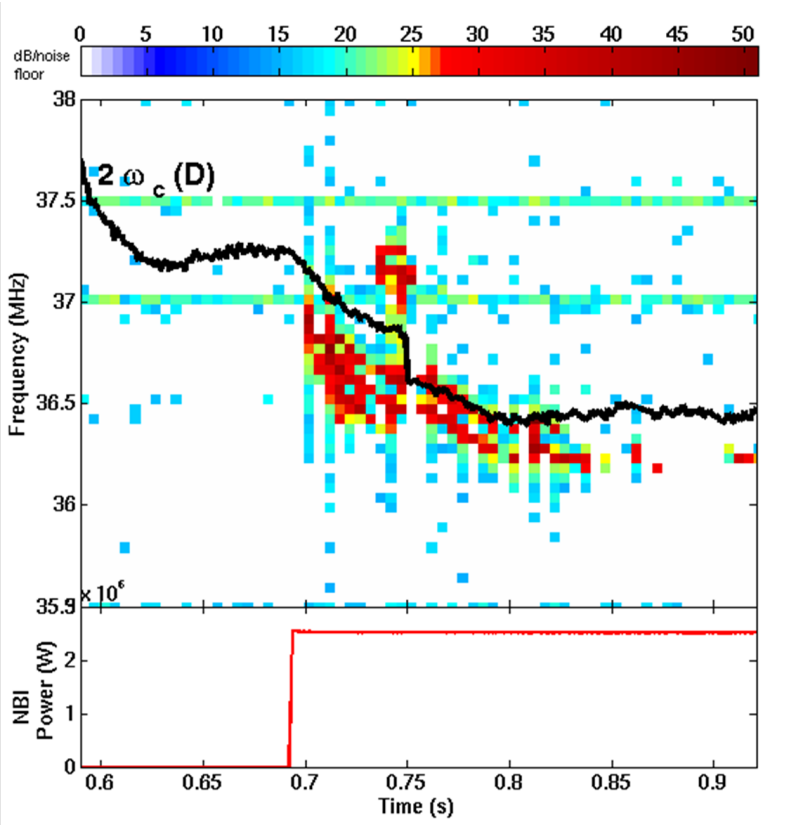

Figure 4.21: Evolution of central ICE

4.3.2 Time evolution

When no instability is present in the plasma core, the signal is transient and appears only at the beginning of NBI pulses. It lasts for around 100 ms. For several beam blips like on Figure 4.22, the ICE is present at each blip.

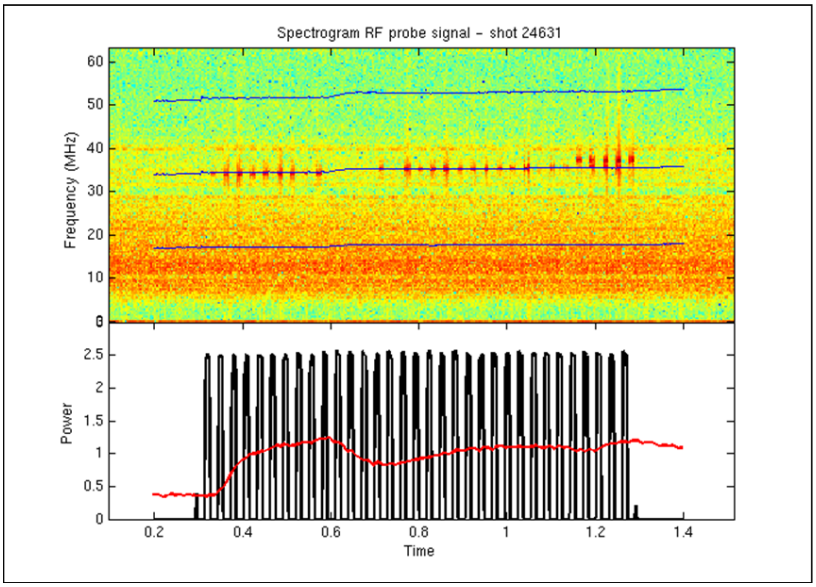

Figure 4.22: The central ICE is repeated for each burst if NBI

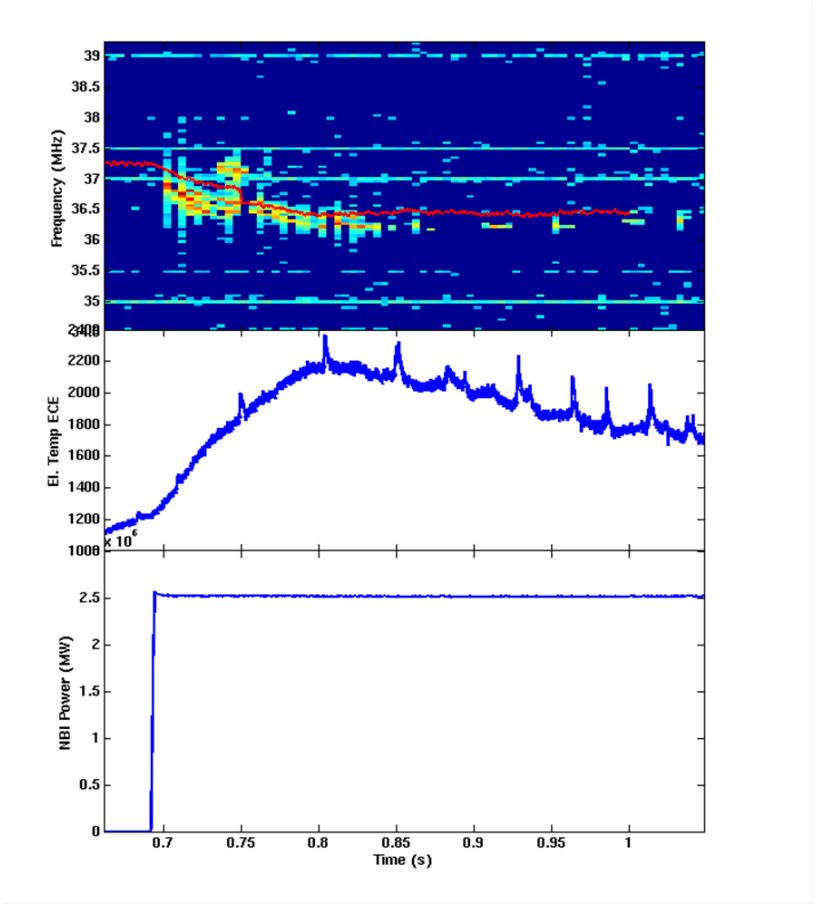

Figure 4.23: Correlation between central ICE ans sawteeth: bursts of ICE are synchronous with the sawteeth peaks.

When central instabilities like sawteeth are present, the signal is emitted in bursts correlated with them and can last in this way for about 1s (cf. Figure 4.23).

4.3.3 *Condition of existence*

No major plasma parameter has been identified as a driver for the excitation of this instability. But its is required to have a neutral beam with a direction of injection parallel to the plasma. With perpendicular injection, no signal has been observed. When the heating switches from one beam (usually beam 3 of box 1) to another (beam 8 of box 2), the third deuterium harmonic replaces the second harmonic (cf. Figure 4.24).

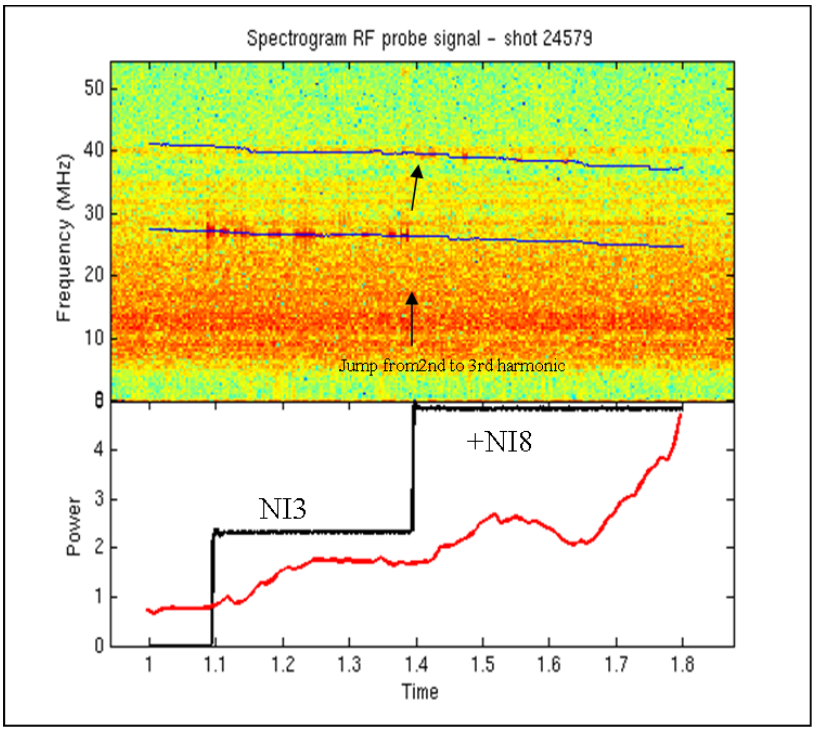

Figure 4.24: Shot 24579. The ICE jumps from the 2nd deuterium harmonic to the the third when the beam is switched.

4.4 *Conclusion*

The observations of ICE on ASDEX Upgrade have brought two principal novelties in comparison with the previous measurements on other machines: the discovery of a rich mode structure for the minority species driven ICE during ICRF heating and the characterization of a short central ICE instability during NBI heating with a mode structure as well and almost no Doppler shift. We will now turn on to the interpretation of these data with respect to the theory developed in the Section 2.2 to validate the models and to do a first attempt at the reconstruction of the distribution function of the fast ions. To facilitate this task, we summarize in the Table 4.1 the main results from this chapter.

Table 4.1: Summary of ICE observation on ASDEX Upgrade.

FP-ICE	
Mode structure	Peaks of width $\Delta f < 100\ kHz$ corresponding to 2nd and 6th harmonics of $\omega_{ci}(p)$ with a shift $\approx 1\ MHz$. A doublet with $\Delta f \approx 1\ MHz$ is sometimes visible. First and third harmonics are more rarely excited but the third one can be the most intense. Peaks corresponding to $2\omega_{ci}(He^3)$ with sometimes doublet. No continuum is observed above 100 Mhz. The emission is trongly enhanced during counter-current injection. **A surprising frequency can be observed in these conditions near** $4\omega_{ci}(D)$.
Time Evolution	The signal is bursty with a duration of $approx 10\ ms$. The signal of He-3 is observed only at the beginning of NBI heating or after almost disruptive instabilities. At small time scales, the signal show oscillations of $\approx 50\ \mu s$ duration.
Condition of existence	neutron rate above $10^{14}\ s^{-1}$. The signal correlates with ELMs and sawteeth.
beam-driven ICE	
Mode structure	Large bandwidth Δf up to 2 MHz. Low intensity and noisy. All harmonics of Deuterium cyclotron frequency excited except the 4th one.
Time evolution	steady state, continuous
Condition of existence	neutron rate above $10^{14}\ s^{-1}$.
mICE	
Mode structure	Peak at $\omega_{ci}(H)$. The second harmonic is far less intense. A fine structure can be observed with the following spacings: $\Delta f_1 \approx 1\ MHz$, $\Delta f_2 \approx 200\ kHz$ and $\Delta f_3 \approx 50\ kHz$.
Time evolution	steady state with duration up to 1 s possible. At small time scales, bursts of 5 ms are observed.
Condition of existence	Heating power above 3 MW and edge density $n < 3.10^{19}\ m^{-3}$.
Central ICE	
Mode structure	Peak at $2\omega_{ci}(D)$ width $\Delta f < 50\ kHz$. No Doppler shift observed. Structure sometimes observed with 2 or 3 frequencies spaced by $\Delta f \approx 150\ kHz$. In counter-current injection, the bandwidth is larger (up to 500 kHz). Jump to third harmonics of Deuterium when the source of NBI is changed.
Time evolution	Duration of about 100ms at the beginning of NBI pulses.
Condition of existence	Parallel NBI injection required.

5 Discussion

The objectives of this section are multiple for the edge-ICE, either due to fusion products or to ICRF.

- to check that the data measured correspond to ICE,
- to compare these results on ASDEX Upgrade with the results on other machines,
- to explain the peculiarities of ICE on ASDEX Upgrade,
- to use the data to reconstruct the distribution function of the fast ions and demonstrate that the ICE can be a viable diagnostic.

For the beam-driven ICE, we will compare the results with the theory of Dendy presented in the section 2.2.3. We will complete it with the results specific to AUG. And finally, for the central ICE, we will try to establish, thanks to the data gathered in the previous section, the basis of a theory to explain this emission.

5.1 FP and m-ICE at the edge

We have distinguished in section 2.2 four ingredients for the ICE process to take place: background plasma modes which constitute the emission (the CAEs), a tail in energy of fast ions with an anisotropic distribution function, the ion cyclotron resonance and a long term evolution modeled by the coupled equations describing the quasi-linear evolution of the distribution function and the balance of the wave energy. We will see how the data fit into this scheme.

5.1.1 Existence of Compressional Alfvén Eigenmodes

The spectrum of the m-ICE presents a clear structure (cf. Figure 4.16) with the evidence of at least two types of modes, one with a large gap (above 1 MHz) and one with a narrower gap (around 200 kHz) between the frequencies. A comparison between the CAE model and the data is presented on Figure 5.1. In spite of the sensitivity of the CAE model mentioned in section, we find a good correlation of the spacing and of the structure of the modes with the experimental data. We recognize the large gaps due to modes with different poloidal wave numbers and the smaller gaps for modes with different toroidal wave numbers.

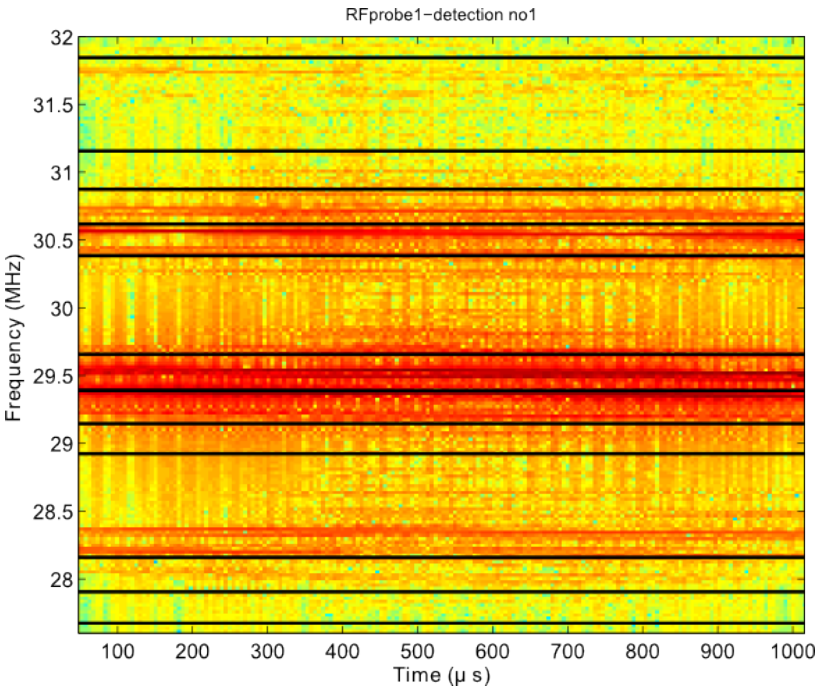

Figure 5.1: Comparison between the spectrogram of shot 25549 and the analytical model of CAE calibrated with the 2D code. We have calculated modes with poloidal mode numbers m between 17 and 22 and toroidal mode numbers n between 7 and 10 which can be superimposed on the experimental data. The CAE model predicts only the frequencies of the possible modes but do not explain why only these modes are excited. This will be done with the analysis of the excitation in the section 2.1.3.

The very fine structure of Figure 4.17 can be explained by an overlapping of modes with different m. We can thus observe a spacing below 50 kHz. The CAE structure is more difficult to evaluate in the case of FP-ICE due to the low time resolution of the spectrograms. In the cases that we have presented, we obtain a spacing between two frequencies of about 200 kHz, which corresponds to the distance between two frequencies with the same m and successive n numbers.

The frequencies of the CAEs are mainly driven by the Alfvén velocity. This is confirmed in a case with a large variation of the frequencies, as shown on Figure 5.2, with the evolution of the density.

We can thus confirm that the CAEs are indeed the modes which are visible on the measurements.

5.1.2 *Existence of a tail of fast ions*

We have to distinguish here the case of the FP-ICE and of the m-ICE.

Fusion Products

Three facts indicate that the fusion products are the source of free energy for this type of emission:

- The signal is present only for a neutron rate above $1.10^{14}\ s^{-1}$, which could indicate that a given concentration of fusion products is necessary to excite the emission
- the frequency signature of Helium-3 is present, which clearly indicates the role of this product in the signal. In addition the frequencies corresponding to the harmonics of the proton (the even harmonics of Deuterium) are most of the time the most intense, which is explained by the higher birth energy of this species.

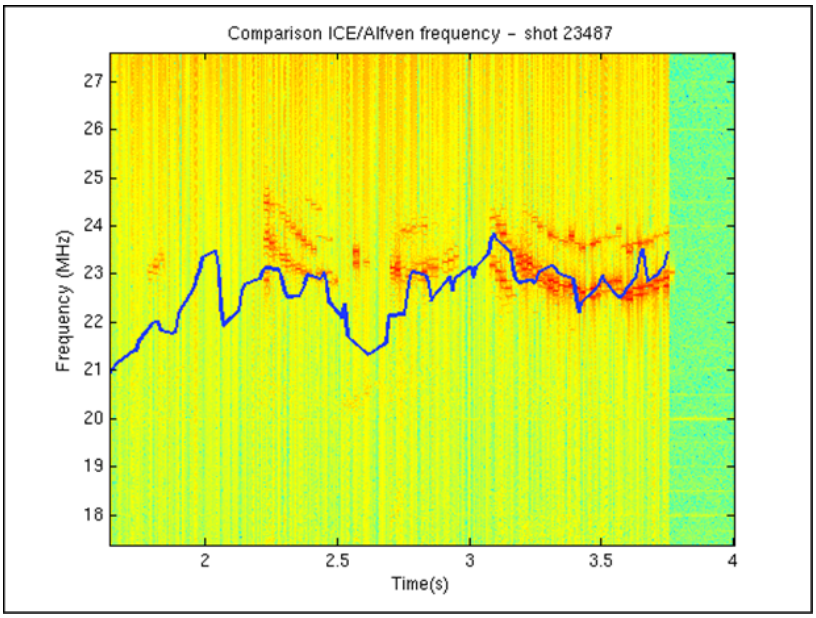

Figure 5.2: Comparison between the measured spectrogram and the evolution of the Alfvén velocity evaluated at the edge (blue line) for discharge 23487. This velocity changes because of the variation of the edge density ($v_A \propto 1/\sqrt{n_i}$).

- The signal presents peaks in relation with instabilities that wipe out the fast ions either in the center (sawteeth) or at the edge (ELMs). The exact synchronization is not known due to the lack of accuracy of our measurement system, but a very probable mechanism is that, during these instabilities, the fast ion distribution becomes narrow in energy and strongly anisotropic at the edge, which, as seen in section 2.1.4, increases the intensity of the signal.

Minority species with ICRF

We have three elements that confirm the existence of a tail of fast ions generated by minority ICRF heating.

The first one is the domain of existence of ICE determined by a heating power above 3 MW and a density below $4.5 \cdot 10^{19}\ m^{-3}$ in the center. A rough calculation shows that it corresponds to the condition for the formation a tail of hydrogen particles at about 1 MeV (which has already been observed on AUG with the FILD, cf. [46]): to get this population, the time necessary to increase the energy of a population of hydrogen ions from 0 to 1 Mev must be shorter than the corresponding slowing down time. This latter is calculated in a simplified case with Equation 2.80 and the heating time is obtained via the expression of the deposited power: $P = (n_{Hres} E_c)/t_h$ where n_{Hres} is the number of hydrogen ions in the resonant layer; $E_c = 1\ MeV$, P is the injected ICRF power and t_h is the heating time.

Secondly, the emission persists for several tens of milliseconds after the generator shutdown, which corresponds to the thermalization of the fast ions and the extinction of the tail.

And finally, when NBI is injected, we see that the flux of hydrogen, as measured by the NPA, decreases. The NBI disturbs in some way the population of fast hydrogen ions. The exact mechanism is not

clear: a part of the ICRF power can be lost in the acceleration of the fast beam ions through 2nd harmonic heating (cf. the simulations for ASDEX Upgrade carried out by Bilato [4]).

5.1.3 *Ion cyclotron interaction*

With the confirmation of the existence of the CAEs and of a tail of fast ions, we can turn on to the calculation of the growth rate spectrum, following the method from section 2.2.3, and to its comparison with the measured spectrum for a case with FP-ICE (corresponding to the discharge 27093) and a case with mICE (corresponding to the discharge 25549). In addition, we want to reconstruct the characteristics of the distribution function at the source of this emission. The mode structure is calculated using the characteristics of the background plasma and is injected in the prediction code for growth rates, together with an initial estimate of the parameters of the distribution function.

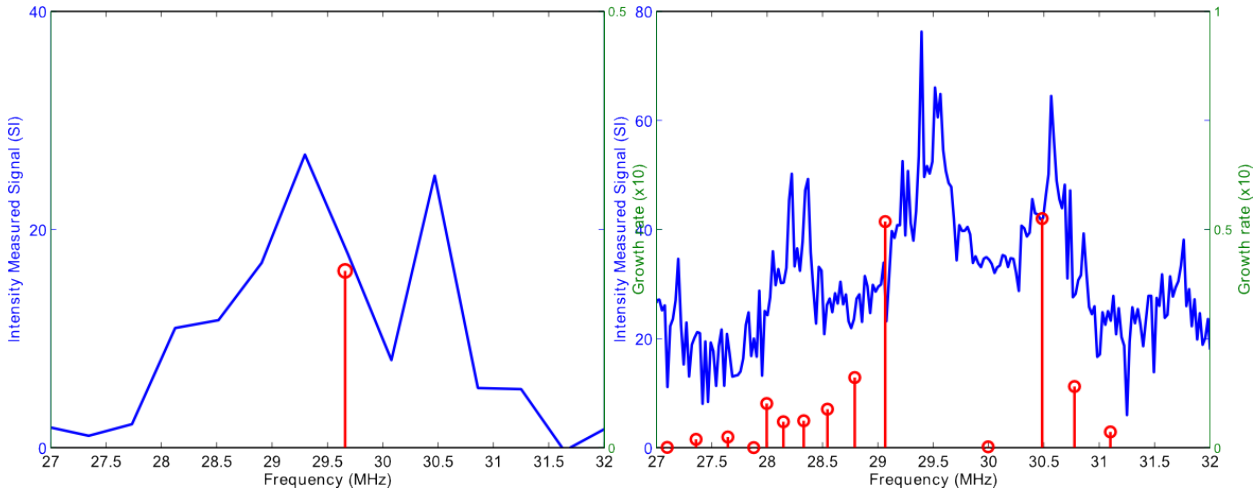

Figure 5.3: Comparison of measured spectrum and growth rate spectrum. Left: FP-ICE due to proton for the discharge 27093. Right: m-ICE for the discharge 25549.

Afterwards, the parameters are varied until we find the best match between the measured spectrum and the growth rate spectrum. The best fit for each case is presented on Figure 5.3. The parameters of the distribution function F which give these results are: for the proton population, $\Delta E = 2.10^5\ eV$, $\Delta P_\phi = 0.2$; for the hydrogen population, $E_0 = 1\ MeV$, $\Delta E = 200\ keV$ and $\Delta\Lambda = 0.01$. These results deserve several comments. First, we find that the theoretical eigenmodes architecture observed in the section 2.1.3 is validated by the experience: only few frequencies are excited in a narrow range around the cyclotron frequency of proton or hydrogen. As said previously, this is not due to damping effects (which are not taken into account for the determination of the growth rate) but to the "extension" in configuration space of the distribution function that allows the respect of the resonant conditions only for a limited number of CAE modes near the cyclotron frequency. Second, the difference between the spectra of FP-ICE and mICE is confirmed: the latter has more features then the former where only one peak is present. It is actu-

ally almost impossible to reconstruct precisely the distribution in this case because this peak can be produced by a wide range of variation of the parameters of the distribution function. The reconstruction is easier since we can support our matching on several frequencies. Yet, the matching is not perfect, far from it: the main issue is to find the mode structure corresponding to the measurements; any slight shift in the mode number and the spectrum can radically change. A consequence of that is that we do not manage to completely reproduce the rather clean frequency structure of the emission as seen on the spectrogram of the Figure 4.17 where we have regular bands of frequencies and sub-frequencies. A solution could be, in the future, to use a 2D MHD code to get a better modeling of the eigenmodes. But this sensitivity to the mode structure may be a numerical problem but also a physical reality: the main driver of the CAE modes structure is the density profile at the edge which can change from machine to machine and, for a given machine, from discharge to discharge. If the spectrum is really sensitive to this profile, it would explain why different hypotheses are required to explain results from different tokamaks (cf. [34] for an overview of the hypotheses on $k_{\|}$ and $k_{\perp}$). On ASDEX Upgrade, we observe this sensitivity as well and this is our final comment on this part: we saw in the previous chapter that the 2nd and 6th harmonics were the most excited for FP-ICE. But for some cases, the 3rd one could become the most intense (cf. Figure 4.4) and even present a triplet of peaks (cf. Figure 4.6). This is an experimental confirmation of what we got with our model on Figure 2.37 b) where a triplet has the highest amplitude near the third harmonic. This shows that the Doppler shift combined with a proper model of the distribution function can explain why odd harmonics of deuterium are excited by protons.

5.1.4 Long term evolution

Two experimental results are useful to validate the model of quasi-linear evolution developed in the Section 2.2.3: first, the acquisition on a short time scale of the mICE presented on Figure 4.16 and, second, the duration time of the mICE (up to 1 s) and FP-ICE (below 10 ms). In order to compare with the spectrogram of mICE, we solved the "predator-prey" simplification 2.92 of the quasi-linear evolution. The result is given on the Figure 5.4. We obtain a surprisingly good agreement in spite of the simplified model. The parameters are the same than those used in the section 2.2.3 except for a bigger damping rate ($\gamma_d/\omega = 5^{-5}$). We obtain a period of about 1.5 ms and a rather stable emission. The distribution is, on average, steady.

We have only one experimental case to benchmark the model, which is not sufficient to validate it. But if it turns out to be sufficiently representative, it would explain the long lifetime of the mICE emission (up to 1 s) and the transient signal of FP-ICE (below 10 ms). In the first case, the ICRF diffusion limits the losses of exciting ions due to ICE interactions; if the power is high enough, the exciting

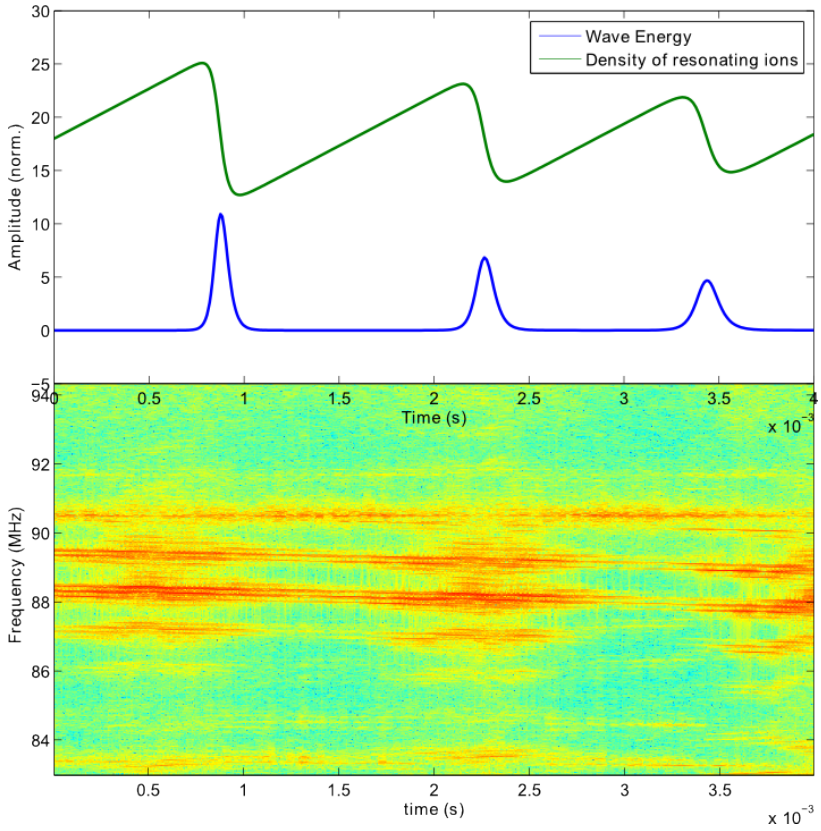

Figure 5.4: Comparison between the quasi-linear "predator-prey" model described by the equations 2.92 and the spectrogram from the discharge 25549 presented on the Figure 4.16. We observe a good agreement between the periods of the experimental and numerical results

population is never depleted. For FP-ICE, the fast ions production rate is rather low in comparison with the ICE diffusion rate and as soon as the instability is excited, the population of exciting ions is quickly depleted, which we can observe on Figure 2.36 b). The numerical time scale for the exponential decrease corresponds to the order of magnitude of the duration of the signal observed.

The important sensitivity of the system to its parameters, as indicated in Section 2.2.3, can lead to various behaviors in function of the machine. ASDEX Upgrade seems to present a rather stable emission of mICE and an instable FP-ICE; in any case, the linear approximation is always valid. JET, which had a high rate of fusion reactions, could have reached other modes of emission: either saturation after an exponential growth of the emission (this is the hypothesis supported by Kolesnichenko [44]) or a very fast oscillation of the ICE signal and of the fast ion population (as supported by Dendy and Cook [12]).

We do not have tackled the topic of the non-linear coupling and other saturation effect. Yet, one of our measurements on AUG can give some preliminary insights on what happens when a CAE mode saturates. We have injected 1.5 MW of ICRF power on the low field side edge of the plasma at a location where CAEs are present. The discharge was not long because the matching of the generator is difficult to insure with a bad coupling at the edge (the wave is almost not absorbed). We observe a frequency at half the ICRF frequency,

i.e. at the cyclotron frequency of deuterium. There are two ways to excite modes with such a frequency: with particles with a large Doppler shift or through non-linear coupling. The first case is not very probable because we have almost no coupling and no acceleration of particles; it seems difficult to create a tail of fast ions in these conditions. Consequently, the non-linear coupling seems the most probable. The nature of the wave is difficult to guess without the measurement of the wave vector but we can note two features: first, it seems to have an internal structures with modes at the limit of frequency accuracy of the digitizer. Second, it has a rather large bandwidth. We have to be cautious but this may support the idea that these modes are CAEs. This would mean that we could excite them with ICRF through non-linear coupling, which supposes in turn that the ICRF wave directly excites the CAEs at the second deuterium harmonic. We do not know the poloidal wave number of the ICRF wave; consequently, it is difficult to make further hypotheses but this measurement, if confirmed, could pave the way for further studies on a non-linear theory of CAEs.

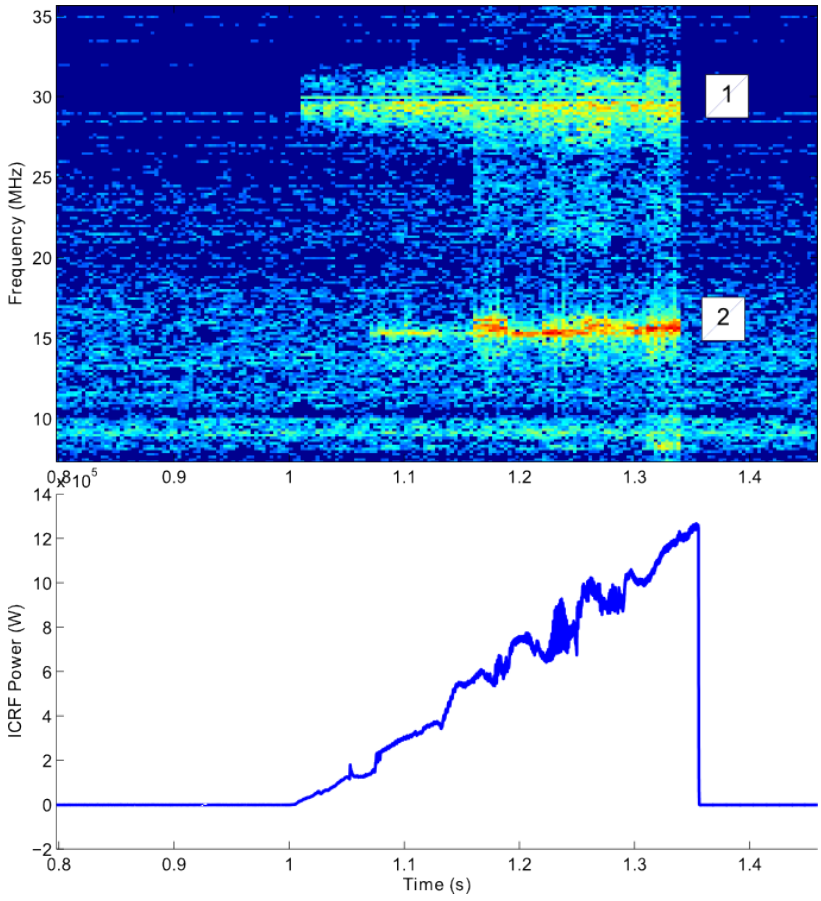

Figure 5.5: Spectrogram of Discharge 26549. The feature 1 is the ICRF frequency attenuated by a notch filter. The feature 2 is a band located at the deuterium cyclotron frequency.

5.2 *Beam-driven ICE*

We turn now on the analysis of the "beam-driven" ICE. The major difference with TFTR, which served as reference for Dendy to develop his theory, is that we have a strong correlation between the beam-driven ICE signal and the neutron rate. This would imply that the fusion products participate to the excitation of this instability. It makes sense since the fusion products have far more free energy than the beam ions. The scenario would also be the following: the beam ions created at the edge of the plasma can sustain the electrostatic modes of propagation described by the dispersion Equation 2.94. If their density is high enough and if their distribution function is anisotropic enough, they can even destabilize their own modes that propagate nearly perpendicularly to the magnetic field. But, it is more probable that they are destabilized by the fusion products, and more precisely by the protons, created in the center and grazing the edge (the same as for the FP-ICE hence the strong correlation between the two emissions). The emission is steadier than for FP-ICE because the electrostatic waves require less energy to be excited; so, it can persist even with a more relaxed population of fusion products. In comparison with what Dendy suggested, it is, in this case, possible to relax the condition on the perpendicularity of propagation of the wave and to admit waves that propagate in a more parallel direction with respect to the magnetic lines. The correlation between the density and the frequency shift presented on the Figure 4.3 can qualitatively be explained by the competing effect between the ionization rate of the neutral beam and its slowing down to create an anisotropic distribution of fast ions. These two effects are related to the density: the higher the density, the higher the ionization rate and the more outwards it occurs, i.e. for lower magnetic fields and lower cyclotron frequencies. Thus, with higher densities, the population of fast beam ions will cover a larger area towards the outside: the bandwidth of the emission will consequently be larger, which is what we have on Figure 4.3.

To finish, a curiosity was noticed in the measurement at a frequency in the spectrum where beam-driven ICE was expected. The frequency signature presented on Figure 5.6 has a strange evolution: it could correspond to the movement of a trapped ion at the edge except that the period is too short for that. One possibility could be that we have the signature of an electrostatic wave supported by the beam ions propagating along the magnetic field. Such electrostatic waves correspond to the oscillations of the beam ions density. The fusion products can resonate with this wave packet with an excess of beam ions and trigger on its location the beam-driven ICE with a frequency corresponding to the position of the interaction. Since the wave packet moves along the magnetic line, so moves the frequency. But this remains for the moment a speculation, as long as we do not have further measurements.

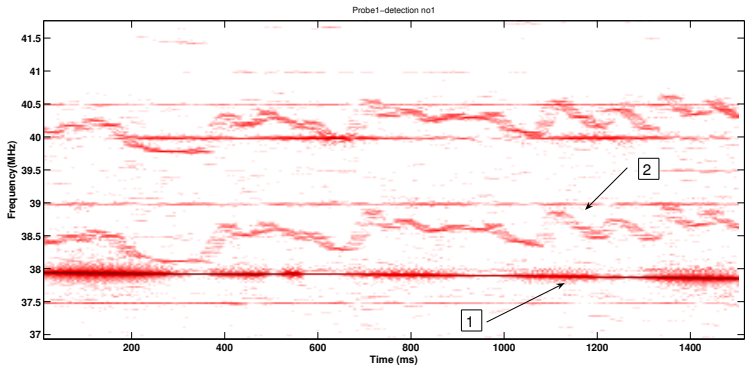

Figure 5.6: Measurement of a single frequency which would correspond to the beam-driven ICE

5.3 *Central ICE*

The development of a theory of central ICE requires the support of the following experimental features:

- there is no Doppler shift of the ion cyclotron frequency observed in the center,
- the wave is able to overcome all dampings and to reach the edge,
- the duration of the emission is longer than the slowing down time of the beam ions in the center,
- the emission occurs only for parallel injection of the beam

From these features, we can eliminate the scenario where electrostatic waves are excited by the beam ions. Otherwise we would have a shorter duration time and we could have beam-driven ICE at the edge at the same time (the conditions are more relaxed for this latter instability). They could be electrostatic waves excited by the fusion products but they are generally strongly damped in the plasma core where we have high densities and temperatures.

We propose therefore the following idea based on the interaction between fusion products and the fast wave in the center. The dielectric tensor that governs the ICE interaction is given by the Equation 2.85:

$$\epsilon^{\alpha} = -\frac{\omega_{p\alpha}^2}{\omega^2} \sum_N \int \frac{\mathbf{V_N^* V_N}}{N\omega_c + \mathbf{k}\cdot\mathbf{v_g} - (\omega + j\eta)} \frac{\Pi}{\tau_b} L_N \cdot F \; dE \; d\Lambda \; dP_\phi$$

Two terms have an impact on the growth rate: the diffusion operator L_N but also the fraction Π/τ_b of the trajectory duration when ICE interaction occurs. We have "neglected" it until now to simplify our calculations but it can be decisive in the case of the central ICE. Indeed, to have an instability with a high growth rate, we need two factors:

- a long interaction time,
- a strong inversion of population in energy.

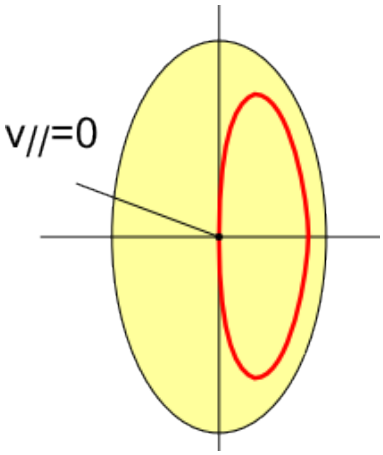

Figure 5.7: Representation of the "potato" trajectory characterized by a parallel velocity null at the center.

These requirements are fulfilled by a part of the fusion product population with $(\Lambda = 1, P_\phi = 0)$ which have potato orbits. As for the first requirement, these ions have $v_\parallel = 0$ in the center and, as displayed on Figure 5.7, their orbit is tangent to the point. The second requirement is more subtle to meet: before slowing down, the fusion products are supposed to be peaked near their birth energy. This simple approximation explains why we have an instability, but it does not explain why we do not have it with the perpendicular injection of neutrals. To understand the difference implied by the angles of injection, we have to remember that the main fusion reactions on ASDEX Upgrade are due to beam/target reactions ([52]). Heidbrink has shown ([32]) that the energy distribution of the fusion products was dependent on the angle of injection. The principle is explained on Figure 5.8. With perpendicular injection, the energy of the beam is transfered into the gyromotion v_1 of the fast ions. Fusion products created in a direction perpendicular to the magnetic field will go either in the direction of the gyromotion of the initial fast ion or opposite to it. The result is a widening in energy of the distribution function for purely perpendicular velocity, i.e., for $v_\parallel = 0$ which is satisfied by the population with potato orbits. Since the distribution is wider, the gradient is smaller and the associated growth rate decreases. The parallel injection of neutrals leads only to a shift in energy of the global distribution function which remains narrow in phase space.

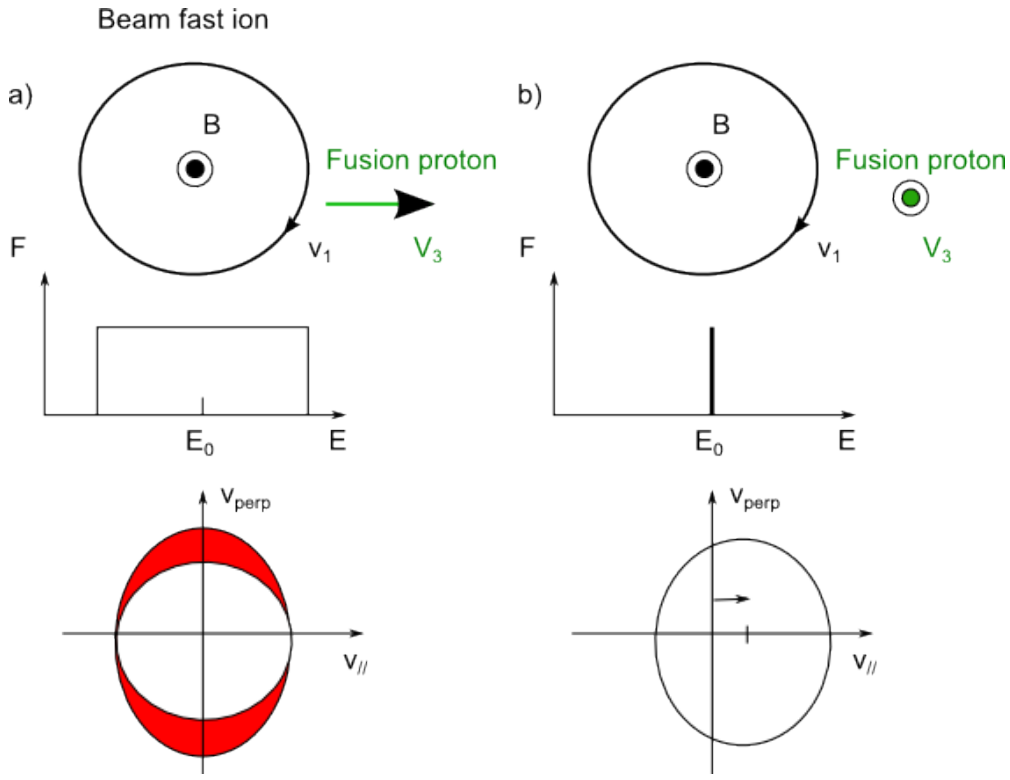

Figure 5.8: Widening of the energy distribution during perpendicular injection of neutrals on a). Simple shift of the distribution during parallel injection on b).

This explains why we have the emission only with parallel injection. In addition, orbits with $v_\parallel = 0$ at the center induce no Doppler

shift, whatever the mode. This is also compatible with the observed spectrum, where the excited frequency matches exactly the cyclotron frequency on the magnetic axis.

In some cases, we have adjacent frequencies which are drifting away from the central frequency with a frequency gap up to 160 kHz. This may be due to the rotation of the plasma. The increase of gap between the frequencies due to a Doppler shift from this rotation would be: $\Delta f = v_{rot}/R$. Measurements with the charge exchange diagnostic give a rotation of $50.10^3\ m.s^{-1}$ which is 2 orders of magnitude below the observed gap. Consequently, the structure observed is probably due to eigenmodes which are excited by ions with a small but non-null parallel velocity in the center.

A more difficult case to interpret is the transition from the 2nd to the 3rd harmonic when adding a second parallel beam. Normally protons should not excite the odd harmonics of the Deuterium cyclotron frequency. It is possible that the second beam, which has a different angle of injection widens the distribution function in the perpendicular direction as well: the second harmonic is suppressed. But in this case, more alpha particles (the secondary products of fusion in D-D plasmas) are produced and are able to excite the 3rd harmonic.

This is mainly a qualitative analysis of the central ICE emission but we have established the basis for a more detailed work using the toolbox from Chapter 2 with a focus on the population of ions with $(\Lambda = 1, P_\phi = 0)$.

6 Conclusion

In this last section, as a conclusion, we review the results that we have obtained in this study, both on the theoretical and experimental level. It is the occasion to recall the assumptions and the key points of the ICE theory developed in this report, its advantages, inconveniences and limitations with respect to the previous theories. It is also the opportunity to look at the future ways to investigate this area and to consider how a diagnostic could be built on this emission for the present tokamaks or for ITER. To finish and imagine the long term, we will sketch a scheme where the instability could be actively controlled to tailor the distribution function of the fast ions.

Our theoretical work was based on the Hamiltonian theory to establish two explicit relations between the parameters of the exciting distribution function of the fast ions in configuration space (E, Λ, P_ϕ) (where E is the energy, Λ the generalized pitch angle and P_ϕ the toroidal momentum) and the characteristics of the emission (growth rate, wave amplitude, mode structure in ω and $\mathbf{k}$). One relation is given on the short time scales (in comparison with the drift period of the ions) by the growth rate of the wave: it relates the constants of motion to the mode structure through the resonance relation $\omega = \omega_{ci} + \mathbf{k} \cdot \mathbf{v_g}$. Therefore, when we have a mode structure (generally established with a cold plasma approximation) and a model of distribution function (simplified in our studies by shifted Gaussian functions), we are able to predict which part of the fast ion population excite a given mode. The other relation establishes the "quasi-linear" long term (compared with the drift period but short compared with the slowing down time and MHD instabilities characteristic time) evolution of the coupled system made of the fast ions and of the excited wave. The relation distinguishes several modes of evolution depending on the intensity of the production of the tail of fast ions (fusion reaction rate or diffusion operator of ICRF heating), on the intensity of the ICE excitation (characterized by the growth rate and by the ICE diffusion operator which are related) and on the damping rates: the resulting emission can be stable, saturated because of an exponential growth, intermittent if the emission quickly depletes the population of fast ions, or damped if the source of fast ions is not strong enough to overcome the dampings, The theory from this report a general framework which can deal with different orbits, populations of ions and types of waves. It is limited by its linear character and by the gyro-center approximation. We have ap-

plied this theory to the four different types of known ICE: the ICE due to fusion products (FP-ICE), the ICE due to ICRF-accelerated ions (m-ICE), the beam-driven ICE and the central ICE. For the FP-ICE and m-ICE, we have elaborated a model of the Compressional Alfvén Eigenmodes which gives the spatial position and extension of the waves and a simple parametrization of the distribution function of the fast ions born in the center and reaching the edge. We are thus able to calculate the growth rate spectrum of the emission in function of the distribution function parameters. By matching this spectrum with the FFT of the measured signal, we can find the best choice of parameters and reconstruct the distribution function of the resonating population. We see that the method works but is very sensitive to the model of CAEs. A better one should be used in the future, taking into account the poloidal variation of the wavevector in a parallelized version of the code to limit the computational time. One possibility is to use the CASTOR-K which is available at the IPP. For the beam-driven ICE, we have just applied the model of waves supported by the ionized beam ions, given by Dendy. But we have found out that the instability is strongly enhanced on AUG by the fusion products reaching the edge. Finally, for the central ICE, we have a developed model where we show that the beam-target fusion reactions triggered by the parallel NBI creates an anisotropy in the distribution function of the products: the population of ions with a "potato" orbit, i.e., which is tangent to the center of the plasma, with a null parallel velocity at this point, constitutes a very narrow energetic tail. This property combined with the long interaction time in the center explains that it can excite the fast wave with no Doppler shift, which is in agreement with the measurements.

We have developed a dedicated diagnostic for ICE based on a fast acquisition system (up to 500 megasamples per second), RF cross antennas in the vessel and a set of low-voltage noise amplifiers and reject filters. We are thus able to acquire spectrograms (spectrum in function of time) with an improved time and frequency accuracy over the previous data on machines like JET and TFTR. Among the most noticeable measurements we have obtained, there are the rich spectrum of mICE where we can observe a complex mode structure that evolves in time at short ($\approx 100\mu s$) and long time scales ($\approx ms$), the central ICE emission with its modes splitting and correlation with MHD instabilities, and the confirmation of the FP-ICE and beam-driven ICE. There is also the presence of this strange structure at the 4th harmonic during counter beam injection. It may be related to beam-driven ICE but further investigations are required. There is still a lot of work to carry out and especially a better cross-checking with other fast ion diagnostics like the FIDA or the Collective Thomson Scattering. One major improvement which has to be brought to the diagnostic is to install a matrix of antennas to measure the poloidal and toroidal wave vectors, which simplifies the interpretation of the results. With better models and an improved diagnostic, we think

that it is possible to reconstruct the distribution function of the fast ions that can excite the ICE. On ITER, we will have in addition a population of alpha particles. There is a great chance that we observe a signal of ICE at the edge (but probably not in the center given the large minor radius of the plasma). The design of the machine is well advanced without possibility to add new dedicated antennas in the vacuum vessel. However, it should be possible to use the voltage probes mounted on the transmission lines of the ICRF system. We saw on AUG that it is possible to receive the ICE signal in this way. If we have the possibility to have these probes on the feeding line of each strap, it is even possible to resolve the wave structure in $\mathbf{k}$. To finish, we can imagine, in the long term, an active use of the ICE emission. We saw that it may be possible to excite the CAEs with the ICRF antenna. Yet, it is not designed for this purpose (the poloidal wave number is not controlled). With a dedicated system, we could excite more accurately these modes and enhance the ICE interaction for some selected modes. Since each mode is "connected" through the resonance condition to a part of the distribution function, we can make this part diffuse in phase space and change its profile. This can be useful when we have high energy ions that graze the edge and are about to be lost from the plasma. A wave generated from the outside could excite the CAE mode in resonance with this part of the population of fast ions and make it diffuse away from the limit of losses. The data from ICE reveal a rich structure and promise many possible applications. We hope that the research in this area will consequently increase and give to this instability the status that it deserves.

Appendix 1: CAE numerical model

We use throughout this section the Gaussian units which make it possible to get more tractable orders of magnitudes and accelerate the computations. The derivation of the CAE field equation comes from the work by Fulop et Kolesnichenko ([27]).

6.1 Equations of CAE in cylindrical coordinates

$$\boldsymbol{\nabla} \times \mathbf{E} = j\omega \mathbf{B} \tag{6.1}$$

$$\boldsymbol{\nabla} \times \mathbf{B} = -j\boldsymbol{\epsilon} \cdot \mathbf{E} \tag{6.2}$$

They are rewritten in cylindrical coordinates after having Fourier transformed the wave vector $\mathbf{k}$ along the z-axis :

$$(\boldsymbol{\nabla} \times \mathbf{E})_r = \frac{\partial E_z}{\partial \theta} - jk_z E_\theta = j\omega B_r \tag{6.3}$$

$$(\boldsymbol{\nabla} \times \mathbf{E})_\theta = jk_z E_r - \frac{dE_z}{dr} = j\omega B_\theta \tag{6.4}$$

$$(\boldsymbol{\nabla} \times \mathbf{E})_z = \frac{1}{r}\frac{d}{dr}(rE_\theta) - \frac{\partial E_r}{\partial \theta} = j\omega B_z \tag{6.5}$$

$$(\boldsymbol{\nabla} \times \mathbf{B})_r = \frac{\partial B_z}{\partial \theta} - jk_z B_\theta = -j(\epsilon_{11}E_r + \epsilon_{12}E_\theta) \tag{6.6}$$

$$(\boldsymbol{\nabla} \times \mathbf{B})_\theta = jk_z B_r - \frac{dB_z}{dr} = -j(\epsilon_{12}E_r + \epsilon_{22}E_\theta) \tag{6.7}$$

$$(\boldsymbol{\nabla} \times \mathbf{B})_z = \frac{1}{r}\frac{d}{dr}(rB_\theta) - \frac{\partial B_r}{\partial \theta} = 0 \tag{6.8}$$

We eliminate all variables except B_z to get a single equation for the parallel magnetic field that we decompose in the form $B_z(r,\theta) = \tilde{B}(r,\theta)e^{jm(\theta+\epsilon_0 sin\theta)}$ where $\epsilon_0 = a/(R_0+a)$ is the inverse aspect ratio. We use in addition the dielectric tensor of the magneto-acoustic wave given by:

$$\epsilon_{11} = \epsilon_{22} = -\frac{-\omega_{pi}^2}{\omega^2} \tag{6.9}$$

$$\epsilon_{12} = -\epsilon_{21} = -i\frac{\omega_{pi}^2}{\omega\omega_{ci}} \tag{6.10}$$

And we finally arrive after some lengthy calculations to the formula describing the parallel magnetic field that we can solve numerically:

$$[\frac{g^{11}}{rv_A^2}\frac{\partial}{\partial r}rv_A^2(1+K_n)\frac{\partial}{\partial r} + g^{22}(1+K_n)\frac{\partial^2}{\partial \theta^2}]\tilde{B} - V(r,\theta)\tilde{B} = 0 \tag{6.11}$$

where $K_n = (v_A n)^2/(\omega_{ci}R)^2$ and with the potential V defined by:

$$V(r,\theta) = (1+K_n)m^2(1+\epsilon_0 cos\theta)^2 g^{22} - \frac{\omega^2}{v_A^2} + \frac{m\omega n_i'}{rk\omega_{ci}n_i}(1+\epsilon_0 cose\theta) \tag{6.12}$$

where k is the ellipticity of the flux surface and where we have introduced the metric tensor to take elliptical section into account:

$$g^{11} = k^{-2}sin^{\theta} + cos^2\theta \tag{6.13}$$

$$g^{22} = (sin^2\theta + k^{-2}cos^2\theta)/r^2 \tag{6.14}$$

6.2 *Numerical Model*

The equation depends on r and θ. We make a discretization the variable θ in the poloidal direction with a finite difference scheme. The discretization is applied only on a half poloidal section, benefiting from the symmetry apart the midplane in the ideal model (without divertor). This half-plane is shared into k sections where k is an adjustable number.

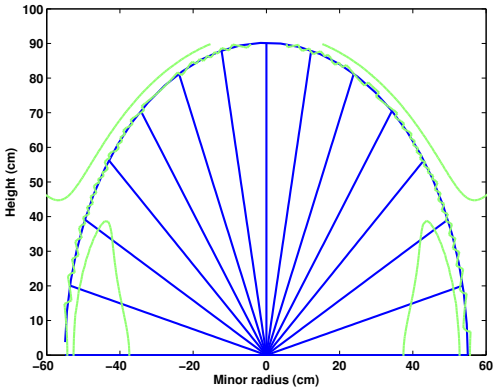

Figure 6.1: Discretization of the plasma section in the poloidal direction. Each line of discretization is solved with a shooting method.

The discretization shown on Figure 6.1 gives a system of k equations dependent on the variable r with boundary conditions at $r = 0$ and $r = 0$ for B_z and B_z'. This system of equations is solved with a shooting method. Given the null values of the boundary conditions, the initial point of the shooting method is taken somewhere in the mid-radius and we shoot in both directions, the coherence being insured by the continuity of B_z and B_z' at this initial point.

Appendix 2: Acronyms and abbreviations

AUG	ASDEX Upgrade
CAE	Compressional Alfven Eigenmodes
ECRH	Electron Cyclotron Resonance Heating
ELM	Edge Localized Modes
FFT	Fast Fourier Transform
FIDA	Fast Ions D-Alpha
FILD	Fast Ions Loss Detector
FP-ICE	Fusion Product Ion Cyclotron Emission
ICE	Ion Cyclotron Emission
ICRF	Ion Cyclotron Range of Frequency
ICRH	Ion Cyclotron Resonant Heating
IPP	Max Planck Institut fur Plasma Physik
ITER	International Tokamak Experiment Reactor
JET	Joint Experiment Torus
JT-60U	Japanese Torus 60 Upgrade
LH	Lower Hybrid
NBI	Neutral Beam Injection
mICE	minority Ion Cyclotrone Emission
MHD	Magneto-Hydro-Dynamics
NPA	Neutral Particle Analyzer
RF	Radio-Frequency
TFTR	Tokamak Fusion Test Reactor
TTL	Transistor-Transistor Logic
TTMP	Transit Time Magnetic Pumping

Bibliography

[1] A. Becoulet, D. J. Gambier, and A. Samain. Hamiltonian theory of the ion cyclotron minority heating dynamics in tokamak plasmas. *Physics of Fluids B: Plasma Physics*, 3(1):137–150, Jan. 1991.

[2] P. Bellan. *Fundamentals of Plasma Physics*. Cambridge University Press, 2008.

[3] P. M. Bellan. *Fundamentals Of Plasma Physics*. Cambridge University Press, 2006.

[4] R. Bilato, M. Brambilla, O. Maj, L. Horton, C. Maggi, and J. Stober. Simulations of combined neutral beam injection and ion cyclotron heating with the toric-ssfpql package. *Nuclear Fusion*, 51(10):103034, 2011.

[5] V. Bobkov, R. Bilato, F. Braun, R. Dux, J.-M. Noterdaeme, t. I. team, and t. A. U. team. ICRF antenna coupling dependence on edge plasma conditions in ASDEX upgrade. *Nuclear Fusion*, 46(7):S469–S475, 2006.

[6] M. Brambilla. *Kinetic theory of plasma waves: homogeneous plasmas*. Clarendon Press, 1998.

[7] S. Cauffman and R. Majeski. Ion cyclotron emission on the tokamak fusion test reactor. In *Proceedings of the tenth topical conference on high temperature plasma diagnostics*, volume 66, pages 817–819, Rochester, New York, Jan. 1995. AIP.

[8] S. R. Cauffman. *Ion cyclotron emission from fusion plasmas*. PhD thesis, Nov. 1997.

[9] F. F. Chen. *Introduction to plasma physics*. New York: Plenum Press, 1974.

[10] L. Colas, S. Heuraux, S. Bremond, and G. Bosia. RF current distribution and topology of RF sheath potentials in front of ICRF antennae. *Nuclear Fusion*, 45(8):767–782, 2005.

[11] P. L. Colestock. Radio-frequency coupling to plasmas. *Journal of Vacuum Science & Technology A: Vacuum, Surfaces, and Films*, 6(3):1975–1983, May 1988.

[12] J. W. S. Cook, R. O. Dendy, and S. C. Chapman. Particle-in-cell simulations of the magnetoacoustic cyclotron instability of fusion-born alpha-particles in tokamak plasmas. *Plasma Physics and Controlled Fusion*, 55(6):065003, 2013.

[13] B. Coppi. Origin of radiation emission induced by fusion reaction products. *Physics Letters A*, 172(6):439–442, Jan. 1993.

[14] B. Coppi, S. Cowley, R. Kulsrud, P. Detragiache, and F. Pegoraro. High-energy components and collective modes in thermonuclear plasmas. *Physics of Fluids*, 29(12):4060–4072, Dec. 1986.

[15] G. Cottrell, V. Bhatnagar, O. D. Costa, R. Dendy, J. Jacquinot, K. McClements, D. McCune, M. Nave, P. Smeulders, and D. Start. Ion cyclotron emission measurements during JET deuterium-tritium experiments. *Nuclear Fusion*, 33(9):1365–1387, 1993.

[16] G. A. Cottrell. Identification of minority ion-cyclotron emission during radio frequency heating in the JET tokamak. *Physical Review Letters*, 84(11):2397, Mar. 2000.

[17] R. O. Dendy, C. N. Lashmore-Davies, and K. F. Kam. A possible excitation mechanism for observed superthermal ion cyclotron emission from tokamak plasmas. *Physics of Fluids B: Plasma Physics*, 4(12):3996–4006, Dec. 1992.

[18] R. O. Dendy, K. G. McClements, C. N. Lashmore-Davies, R. Majeski, and S. Cauffman. A mechanism for beam-driven excitation of ion cyclotron harmonic waves in the tokamak fusion test reactor. *Physics of Plasmas*, 1(10):3407–3413, Oct. 1994.

[19] D. A. D'Ippolito, J. R. Myra, M. Bures, and J. Jacquinot. A model of sheath-driven impurity production by ICRF antennas. *Plasma Physics and Controlled Fusion*, 33(6):607–642, 1991.

[20] H. Duong, W. Heidbrink, E. Strait, T. Petrie, R. Lee, R. Moyer, and J. Watkins. Loss of energetic beam ions during TAE instabilities. *Nuclear Fusion*, 33(5):749–765, May 1993.

[21] D. V. Eester. Trajectory integral and hamiltonian descriptions of radio frequency heating in tokamaks. *Plasma Physics and Controlled Fusion*, 41(7):L23–L33, 1999.

[22] Equipe TFR. High-power neutral injection and ion power balance in TFR. *Nuclear Fusion*, 18(9):1271–1303, Sept. 1978.

[23] L.-G. Eriksson, M. J. Mantsinen, T. Hellsten, and J. Carlsson. On the orbit-averaged monte carlo operator describing ion cyclotron resonance frequency wave–particle interaction in a tokamak. *Physics of Plasmas*, 6(2):513–518, Feb. 1999.

[24] L.-G. Eriksson and F. Porcelli. Dynamics of energetic ion orbits in magnetically confined plasmas. *Plasma Physics and Controlled Fusion*, 43(4):R145–R182, 2001.

[25] T. Fulop, Y. Kolesnichenko, M. Lisak, and D. Anderson. Origin of superthermal ion cyclotron emission in tokamaks. *Nuclear Fusion*, 37(9):1281–1293, 1997.

[26] T. Fulop and M. Lisak. Ion cyclotron emission from fusion products and beam ions in the tokamak fusion test reactor. *Nuclear Fusion*, 38(5):761, May 1998.

[27] T. Fulop, M. Lisak, Y. I. Kolesnichenko, and D. Anderson. The radial and poloidal localization of fast magnetoacoustic eigenmodes in tokamaks. *Physics of Plasmas*, 7(5):1479–1486, May 2000.

[28] M. Garcia-Munoz. *Modelling of Fast Ion Losses in Tokamaks*. Diploma-thesis, LMU, May 2003.

[29] M. Garcia-Munoz. *Fast Response Scintillator based detector for MHD Induced Energetic Ion Losses In ASDEX Upgrade*. PhD thesis, LMU, June 2012.

[30] N. N. Gorelenkov and C. Z. Cheng. Excitation of alfven cyclotron instability by charged fusion products in tokamaks. *Physics of Plasmas*, 2(6):1961–1971, June 1995.

[31] E. G. Harris. Unstable plasma oscillations in a magnetic field. *Physical Review Letters*, 2(2):34, Jan. 1959.

[32] W. Heidbrink. Energy spectra from "beam-target" nuclear reactions in magnetic fusion devices. *Nuclear Instruments and Methods in Physics Research Section A: Accelerators, Spectrometers, Detectors and Associated Equipment*, 236(2):380–384, May 1985.

[33] W. Heidbrink and G. Sadler. The behaviour of fast ions in tokamak experiments. *Nuclear Fusion*, 34(4):535–615, 1994.

[34] T. Hellsten, K. Holmstrom, T. Johnson, T. Bergkvist, and M. Laxaback. On ion cyclotron emission in toroidal plasmas. *Nuclear Fusion*, 46(7):S442–S454, 2006.

[35] T. Hellsten, T. Johnson, J. Carlsson, L.-G. Eriksson, J. Hedin, M. Laxaback, and M. Mantsinen. Effects of finite drift orbit width and RF-induced spatial transport on plasma heated by ICRH. *Nuclear Fusion*, 44(8):892–908, 2004.

[36] T. Hellsten and M. Laxaback. Edge localized magnetosonic eigenmodes in the ion cyclotron frequency range. *Physics of Plasmas*, 10(11):4371–4377, Nov. 2003.

[37] K. Ikeda. ITER on the road to fusion energy. *Nuclear Fusion*, 50(1):014002, Jan. 2010.

[38] S. I. Itoh, A. Fukuyama, and K. Itoh. ICRF wave catalyst in beam-heated plasma. *Plasma Physics and Controlled Fusion*, 28(9B):1499–1510, Sept. 1986.

[39] S. I. Itoh, K. Itoh, and A. Fukuyama. Beam-driven ICRF instability and associated nonclassical transport in tokamak. *Plasma Physics and Controlled Fusion*, 26(11):1311–1324, 1984.

[40] T. Johnson, T. Hellsten, and L.-G. Eriksson. Analysis of a quasilinear model for ion cyclotron interactions in tokamaks. *Nuclear Fusion*, 46(7):S433–S441, 2006.

[41] A. N. Kaufman. Quasilinear diffusion of an axisymmetric toroidal plasma. *Physics of Fluids*, 15(6):1063–1069, June 1972.

[42] H. Kimura, Y. Kusama, M. Saigusa, G. Kramer, K. Tobita, M. Nemoto, T. Kondoh, T. Nishitani, O. D. Costa, T. Ozeki, T. Oikawa, S. Moriyama, A. Morioka, G. Fu, C. Cheng, and V. Afanas'ev. Alfvén eigenmode and energetic particle research in JT-60U. *Nuclear Fusion*, 38(9):1303–1314, Sept. 1998.

[43] Y. Kolesnichenko, T. Fulop, M. Lisak, and D. Anderson. Localized fast magnetoacoustic eigenmodes in tokamak plasmas. *Nuclear Fusion*, 38(12):1871–1879, 1998.

[44] Y. Kolesnichenko, M. Lisak, and D. Anderson. Superthermal radiation from tokamak plasmas caused by cyclotron magnetoacoustic instability. *Nuclear Fusion*, 40(7):1419–1427, 2000.

[45] X. S. Lee, J. R. Myra, and P. J. Catto. General frequency gyrokinetics. *Physics of Fluids*, 26(1):223–229, Jan. 1983.

[46] M. Mantsinen and L.-G. Eriksson. Analysis of ICRF-Accelerated ions in ASDEX upgrade.

[47] J. Myra, D. D'Ippolito, D. Russell, L. Berry, E. Jaeger, and M. Carter. Nonlinear ICRF-plasma interactions. *Nuclear Fusion*, 46(7):S455–S468, 2006.

[48] J.-M. Rax. *Physique des plasmas - Cours et applications: Cours et applications*. Dunod, Aug. 2005.

[49] J. A. Rome and Y.-K. M. Peng. The topology of tokamak orbits. *Nuclear Fusion*, 19(9):1293, Sept. 1979.

[50] Shoichi SATO, Makoto ICHIMURA, and Yuusuke YAMAGUCHI. Observation of ion cyclotron emission owing to DD fusion product h ions in JT-60U. *Plasma and Fusion Research*, Volume 5:S2067, 2010.

[51] T. H. Stix. Heating of toroidal plasmas by neutral injection. *Plasma Physics*, 14(4):367, Apr. 1972.

[52] G. Tardini, C. Hoehbauer, R. Fischer, R. Neu, and t. A. U. Team. Simulation of the neutron rate in ASDEX upgrade h-mode discharges. *Nuclear Fusion*, 53(6):063027, June 2013.